Towards lanthanide doped quantum dots: attachment and incorporation of trivalent lanthanide ions into InP and CdSe semiconductor nanocrystals

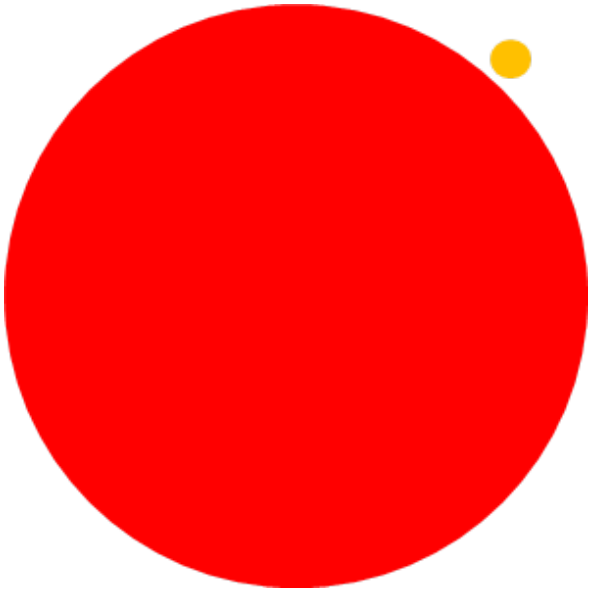

Adriaan Frencken

Supervised by:
Elleke van Harten, MSc
Joren Eilers, PhD
Robin Geitenbeek, MSc
Prof. dr. Andries Meijerink

Condensed Matter and Interfaces UTRECHT UNIVERSITY

Master Thesis

2014 - 2016

Contents

Chapter 1

Introduction

On the macroscopic scale, the physical and chemical properties of a material, such as its color and its melting point, are commonly known to be rigid and independent of the size of the object. Take for example my sweater. I own a red sweater, size XL. This sweater has been fabricated in the sizes M, L, XL and XXL. Each differently sized sweater is made of the same fabric and still has the same color. I could even cut up my sweater in smaller pieces and their color would not change, nor would their melting point. It should be noted that this last statement has not been verified experimentally, fortunately, as this is not a thesis about my sweater. This is a thesis about nanomaterials.

Nanomaterials are different. On the nanoscale, characteristics such as the melting point and the energy levels of a material may change with the size of the particle, while its chemical composition remains the same. These newfound properties and their dependence on the size and shape of the material have piqued the interest of researchers worldwide resulting in the exciting scientific field of nanotechnology. The last couple of decades have seen an exponential growth of activities in this field, driven by the promise of the numerous applications of nanomaterials. These applications range from catalysis to lighting to quantum computing. Furthermore, the field has attracted the attention of the general public, nanotechnology being widely perceived as one of the key technologies of the twenty-first century [1].

A nanomaterial is defined as matter with at least one of its spatial dimensions sized between 1 and 100 nanometers. This is a broad definition. The term nanomaterial therefore encompasses a large variety of particle types: two-dimensional materials (nanosheets [2, 3]), one-dimensional materials (nanorods, nanowires [4, 5]) and zero-dimensional materials (nanocrystals [6, 7]). This work is focused on a sub-class of the last type: the quantum dot.

Quantum dots are colloidal semiconductor nanocrystals. They are composed of a semiconductor crystal core that is surrounded by organic ligands to ensure dispersion in a liquid medium while maintaining colloidal stability of the particles. The small size of the quantum dots endows them with an interesting set of characteristics. One of these is the large surface to volume ratio. In a macroscopic material, the amount of surface atoms is relatively so small that their contribution to the system can be neglected. In a quantum dot of 1 nm, composed of ca. 30 atoms, almost every atom is a surface atom! This heavily affects the particle reactivity, as well as its crystalline stability [1, 6, 8, 9]. Another quantum dot characteristic that has received particular scientific attention is the dependence of the semiconductor bandgap on the particle size. The smaller the particle becomes, the larger its bandgap will be. This is explained by the quantum confinement effect. This effect occurs when the dimensions of the semiconductor particle approach the Bohr radius (a_0) of the exciton, thereby spatially confining the electron-hole pair and raising its energy. This increases the bandgap energy and gives rise to discrete energy levels near the bands. The effect has the result that the wavelengths of light absorbed and emitted by the particles can be tuned by their size [6–11].

Over the years, the combined work of a large number of research groups has provided us with a vast library of publications describing the synthesis of fluorescent quantum dots and their application in light emitting diodes (LEDs) [12–15], photovoltaic devices [16–20] and biological labelling[21–24]. For each of these applications, synthetic control over the optoelectronic properties of the material is of paramount importance as in a LED emission of specific colors is needed, for a photovoltaic device

light absorption over a broad spectrum is desired and for a biological label the light must be emitted over a longer timescale so it can be distinguished from the background radiation [25].

To cater to these needs, the optoelectronic properties of a quantum dot can be tailored even further by introducing optically active impurity atoms into the crystal lattice in a process known as doping. The incorporation of optically active dopants into semiconductor nanocrystals is an active area of research and the successful doping of quantum dots has been extensively reported, most notably with luminescent Mn [26–28] and Cu [29, 30] ions. Some reports are found where the dots have been successfully coupled to lanthanide ions [31–34], which is arguably even more interesting due to the wide range of electronic structures that the lanthanides display. Their intra 4f transitions result in a narrow line emission that is minimally influenced by the chemical environment of the lanthanide ion. The doping of quantum dots with Yb^{3+} seems especially promising both for fundamental research and for applications, because the Yb^{3+} emission is well separated from the emission of the quantum dot in the visible region.

A problem that needs to be overcome before quantum dots can be applied on an industrial scale is the intrinsic toxicity of the materials that the dots are composed of. The material that has been investigated most extensively for the use in dots is cadmium selenide (CdSe), which contains cadmium, a highly toxic metal. For the proposed applications the dots need to be free of toxic elements so a variety of non-toxic materials is being investigated. One of these materials is indium phosphide (InP). Quantum dots composed of InP are proposed to be a promising alternative to CdSe dots as their emission and absorption can be tuned over the visible and near-infrared range as well, while having a lower intrinsic toxicity due to the covalent nature of their crystal lattice [35, 36]. A disadvantage of InP is its low fluorescent quantum yield, measured to be as low as 1 % [35]. This low quantum yield has been attributed to the dangling bonds on the surface, facilitating non-radiative relaxation of the excited state. However, there have been several publications describing the growth of a semiconductor shell of a different material over InP quantum dots to passivate the dangling bonds on the surface and raise the quantum yield to values approaching those measured in CdSe nanocrystals [36–39].

The goal of the project

The primary aim of the project described in this report is to combine the narrow line emission of lanthanide ions with the broad absorption of non-toxic InP nanocrystals. This goal is pursued by developing a synthetic procedure to dope InP quantum dots with Yb^{3+} ions and investigating the energy transferred from dot to dopant. Several methods are employed to grow InP quantum dots, to attach Yb^{3+} ions to their surface and to overgrow the dots with a semiconductor shell. To elucidate their electronic structure, the resulting particles are subjected to a variety of analytical techniques, including absorption spectroscopy, emission spectroscopy and measuring the lifetime of the excited states.

As a secondary aim, this thesis strives to provide a better description of the internal and electronical structure of ytterbium doped CdSe quantum dots. To this end, CdSe quantum dots are synthesized, a previously described doping method is applied and the resulting particles are subjected to the same analytical techniques as the InP particles.

The thesis is comprised of the following sections: the introduction will be followed by a theory section, in which a more fundamental theoretical background will be provided to understand concepts that have already been briefly addressed in this introduction, such as quantum confinement, quantum dot synthesis, lanthanide electronic structure and energy transfer. Then two sections will follow, one detailing the experiments done with InP quantum dots and one those with CdSe quantum dots, including a description of the experimental methods used, the results that were obtained and a discussion of the obtained results. The thesis will then be concluded with a summary and an outlook towards future experiments.

Chapter 2

Theory

In this thesis, the synthesis and optical properties of doped semiconductor nanocrystals will be described. To properly discuss the experimental findings, a fundamental theoretical background is required. This chapter is dedicated to providing this background and will cover the following subjects: the electronic structure of a quantum dot and the origin of its size-dependent bandgap, the influence of shell-growth on the material properties, quantum dot synthesis techniques with focus on the hot injection method, synthetic strategies to dope nanocrystals, the electronic properties of lanthanide ions with focus on intra 4f transitions and finally the concept of energy transfer.

2.1 The electronic structure of a quantum dot

Quantum dots have been the subject of extensive research in large part due to the size dependence of their electronic properties: when the size of the nanocrystal decreases, the energy gap between the valance band and the conduction band of the semiconductor material increases and discrete energy levels close to the bands can be observed [1, 6–11]. This phenomenon is known as 'quantum confinement'. A demonstration of this effect is displayed in figure 2.1 where a series of differently sized CdSe crystals in dispersion are shown underneath schematic representations of their electronic structure. Quantum confinement can be understood by either describing the system as a very small semiconductor crystal in a 'top-down' approach or as a very large molecule in the more chemical 'bottom up' approach. Both explanations will be discussed in more detail in this section.

2.1.1 Top down approach

In the top down approach we approximate the quantum dot as a semiconductor nanocrystal that has become so small that its exciton wave-function becomes spatially confined. Increased spatial confinement of the exciton in increasingly smaller dots has the effect that the exciton energy increases and the material absorbs and emits light of higher energies.

When an electron in a semiconductor material is promoted to the conduction band by absorption of energy, it leaves behind a positively charged hole in the valence band. This positively charged hole and negatively charged electron are held together by attraction of a Coulomb force and this electron-hole pair can be described as a quasi-particle known as an exciton. The average distance between the electron and the hole is referred to as the exciton bohr radius (a_0) and its expression is given in equation 2.1 [41].

$$a_0 = \frac{\hbar^2 \epsilon}{e^2} \left(\frac{1}{m_e} + \frac{1}{m_h} \right) \tag{2.1}$$

Here, ϵ is the material dielectric constant, e is the charge of the electron and m_e and m_h are the effective masses of the electron and the hole, respectively. As can be seen, the exciton bohr radius is inversely dependent on the effective masses, which are themselves measures of the electron and hole mobility in the solid. In an insulator, electrons are not very mobile and a_0 is typically very small, whereas in semiconductors and metals, where electrons experience higher mobility, a_0 becomes larger.

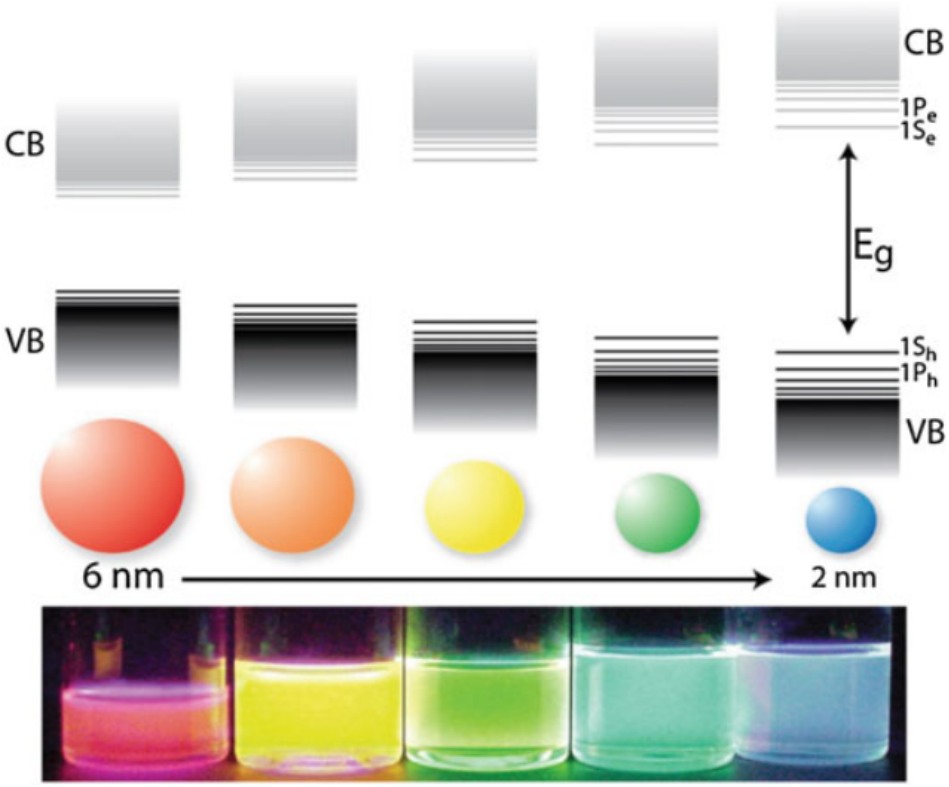

Figure 2.1: A schematic representation of the energetic band gap dependence on the CdSe crystal size. The electronic band structure of CdSe is displayed above a cartoon of differently sized crystals corresponding with a series of vials containing CdSe dispersions emitting light of different colors upon excitation with a UV-lamp. As the size of the crystals decreases from 6 nm to 2 nm the band gap increases and the emitted light shifts to higher wavelengths. Image reproduced from reference [40].

A correlation between energy bandgap and exciton bohr radius can be seen in materials: when the bandgap decreases, a_0 increases [1, 41].

The bohr radius gives a measure of the extension of an exciton in a material. When the size of the material approaches this length scale, confinement effects can be seen. As a general rule of thumb quantum confinement sets in when the size of a crystal is decreased below $4a_0$. The InP exciton bohr radius is 15 nm [42] and the CdSe exciton bohr radius is 5.6 nm [43], which means that InP displays quantum confinement over a larger range of particle sizes, implying that the emission and absorption of InP can be tuned over a broader spectrum [35].

Among the first to describe the spatial confinement of the exciton physically was the group of Brus. They synthesized and spectroscopically analyzed CdS and ZnS nanocrystals (in their work referred to as crystallites) and saw a shift to higher absorption energies with smaller crystals [10]. They explained this observation based on the confinement of the exciton wave function and adapted the wave function for a bulk material to one for a confined crystal in order to solve the Schrödinger equation for the lowest excited electronic state in a nanocrystal [11]. This expression is given in equation 2.2.

$$E = E_g + \frac{\hbar^2\pi^2}{2R^2}\left(\frac{1}{m_e} + \frac{1}{m_h}\right) - \frac{1.8e^2}{\epsilon_2 R} + \text{smaller terms} \tag{2.2}$$

This equation consists of three major terms. The first term, E_g, denotes the band gap energy of the bulk material at 0 K. The second term describes the spatial localization of the exciton, where R is the crystal radius. The third term is an expression for the size-dependent coulombic attraction. As can be seen, the positive term for the spatial localization energy is inversely dependent on the square of the particle radius and the negative term on just the particle radius, meaning that when R is sufficiently decreased, the term for the spatial localization will dominate and the band gap in the crystal will start to increase.

2.1.2 Bottom up approach

The quantum confinement effect can also be understood from the bottom up when we approach the quantum dot as a very large molecule or a cluster of atoms. The basis of this approximation is the quantum chemical method of linear combination of atomic orbitals (LCAO) where an overall wave function for a molecule is constructed from the individual atomic orbitals [40, 44, 45]. A simple example is the construction of bonding (σ) and anti-bonding (σ^*) orbitals in H_2 molecules. The electrons of two 1s atomic orbitals can lower their energy by occupying the bonding molecular orbital and leaving the anti-bonding molecular orbital unoccupied, as displayed in figure 2.2. The highest occupied molecular orbital is referred to as the HOMO and the lowest unoccupied molecular orbital is referred to as the LUMO.

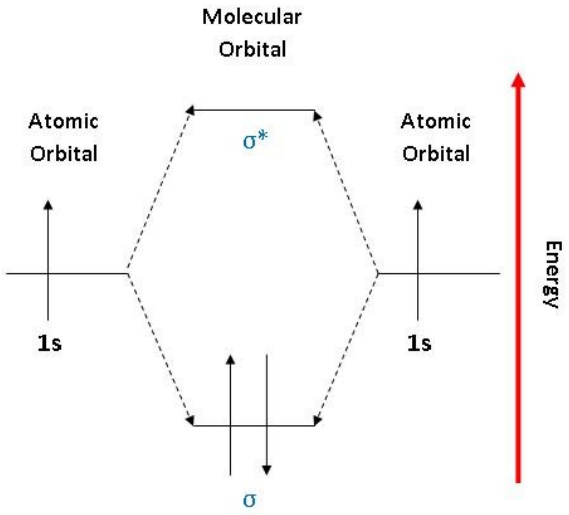

Figure 2.2: A representation of the electronic structure of H_2. The 1s atomic orbitals of two H atoms combine to form a bonding orbital (σ) and an antibonding orbital (σ^*). The electrons occupy the energetically lower σ orbital to form a molecular bond. Image reproduced from reference [45].

The principle can also be applied on larger systems, consisting of more than two atoms, where with the addition of each extra atom, a new bonding and anti-bonding orbital are formed [44]. As more atoms are added to the system and more molecular orbitals are formed, the energy gap between the HOMO and the LUMO starts to decrease and if a very large number of atoms is brought together in this manner, the density of states increases and the molecular orbitals begin to form quasi-continuous bands, separated by a band gap energy. This is demonstrated in figure 2.3, where we start out with a HOMO and LUMO energy level of a molecule and add atoms until a band structure is formed. On the intermediate between the molecule and bulk material we find the electronic structure of a quantum dot, with a filled conduction band and empty valance band and discrete energy levels at the band edges [1, 40, 44]. If more atoms are added to this dot, the band gap energy decreases further and the electronic structure becomes that of a bulk semiconductor material [1, 40, 44].

2.2 The electronic structure of core-shell systems

As demonstrated in the previous section the electronic structure of a quantum dot can be extensively controlled by varying the particle size. Another way to influence the electronic properties of a dot is by overgrowing it with a shell to form a core-shell system. In such a system, a semiconductor nanocrystal is the core on which another material, usually also a semiconductor, is epitaxally grown as a shell to form a heterojunction. Core-shell systems are generally classified as three different types based on their electronic structures: type-I, type-$I^{1/2}$ and type-II [1, 40, 47]. This section will describe these different types and their influence on the quantum dot properties. A schematic representation of the electronic structure of the different core-shell system types is displayed in figure 2.4.

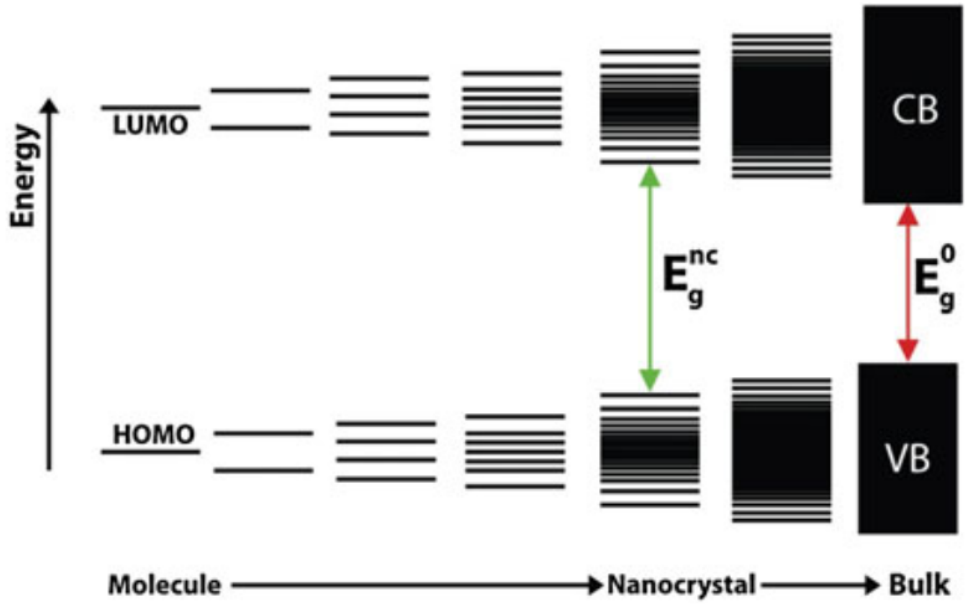

Figure 2.3: A demonstration of the bottom-up explanation of quantum confinement. At the left, the HOMO and the LUMO of a molecule are displayed as energy levels. When more atomic orbitals are added to the system, more molecular orbitals are formed. The HOMO-LUMO gap decreases and the density of states increases. Bands are formed and the electronic structure of a quantum dot is obtained. As the amount of atoms is further increased the energy band gap decreases further and the conduction band and valance band of a semiconductor are formed. Image reproduced from reference [46].

The type-I core-shell system is the most studied one and is comprised of a semiconductor core overgrown with a shell of a different semiconductor or insulator that has a higher conductive band edge and a lower valence band edge. This band alignment ensures that the exciton that is generated in the core remains confined there. The reason to grow a type-I shell is usually to shield the core material from oxidation or photodegradation, processes that are detrimental to the desired electronic properties. Another reason to use a type-I shell is to passivate dangling bonds on the quantum dot surface that may otherwise act as trap states for charge carriers. The overgrowth of a type-I shell on a quantum dot is in many cases accompanied by a small red-shift in the excitonic peak in its absorption and emission spectra, attributed to the partial extension of the exciton wavefunction into the shell material [1, 40, 47].

In a type-$I^{1/2}$ core-shell system, a shell is grown that has either the conduction or the valence band edge energy similar to that of the core material, but the other band edge lower when it's a valence band or higher if it's a conduction band. This configuration has the effect that the one of the exciton charge carriers is free to move through both core and shell, while the other remains trapped in the core. The type-$I^{1/2}$ shell type has a similar shielding benefit for one of the charge carriers to that of a type-I shell, the main observed difference is the bigger red-shift of the excitonic peak in absorption and emission spectra. This shift is caused by the delocalization of the electron or hole [1, 40, 47].

Type-II core-shell systems are made by overgrowth of a shell material that has both a lower conduction band edge energy and a lower valence band edge or a higher conduction band edge energy and a higher valence band edge. This makes sure that after excitation, the one of the exciton charge carriers is confined to the shell material while the other is confined to the core. The effect of this staggered band gap alignment is that emission and absorption are red-shifted and due to the indirect nature of the electron-hole recombination, the lifetime of the excited state is increased. An interesting property of the type-II system is that the emission and absorption energy may be lower than either the core or the shell band gap, which means that the emission color can be tuned to wavelengths that were otherwise unattainable for certain materials [1, 40, 47].

In this thesis, several different semiconductor materials are used to form different types of core shell structures. The band gap energies of a selection of semiconductors is displayed in figure 2.5.

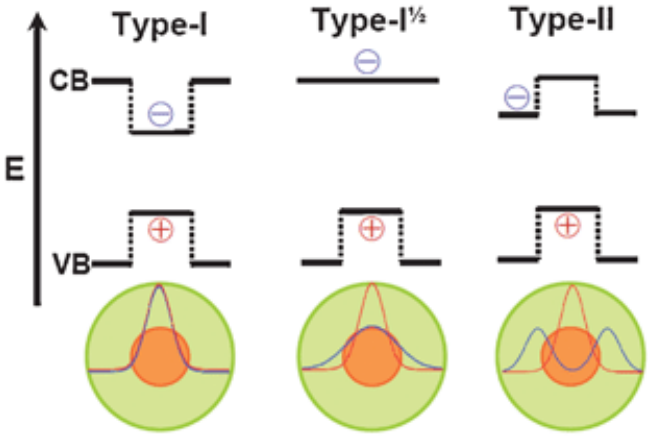

Figure 2.4: Schematic representation of the different shell types. Band structures of the different types are displayed above representations of the core-shell systems. The localization of the charge carriers is given by the gaussian functions. Type-I systems have the band gap of the core inside that of the shell material and both the electron and the hole localized in the core. Type-$I^{1/2}$ systems have the same conduction band edge for both materials with the valence band edge lower for the shell material, here the electron is delocalized over both core and shell. Type-II systems have a staggered band gap allignment. The electron is localized in the shell and the hole in the core. Reproduced from reference [40].

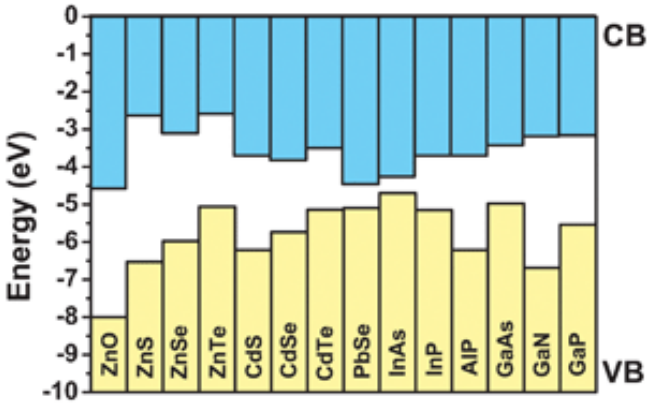

Figure 2.5: The relative band allignments of a selection of semiconductors. The energy of the states is given in eV with respect to vacuum, where E = 0 eV. Reproduced from reference [40].

2.3 Quantum dot synthesis

Ever since the discovery of quantum dots and up to this day, the synthesis of quantum dots is an active area of research. Several methods to synthesize the particles have been developed. The synthesis can be approached both from the top down and the bottom up. An example of a top down approach to nanocrystal fabrication is lithography. With this technique, an electron beam or a chemical is used to etch away bulk material and effectively cut it into smaller pieces [48]. An example of a bottom up approach to quantum dot synthesis is the colloidal synthesis. This chemically oriented method relies on the formation of colloidal semiconductor crystals in the liquid phase, by aggregation of monomers in solution. The majority of the protocols based on this method uses the 'hot-injection' technique, where a room temperature solution of one of the precursors is injected into a hot solution of the other precursors [1, 40, 49, 50].

2.3.1 Hot injection

One of the main advantages of the hot injection technique and one of the reasons it is so extensively employed, is that the colloidal nucleation event can be separated from the colloidal growth regime. This ensures that the particles are formed simultaneously during the injection step, and the size of the particles can be controlled by the length of the growth time, resulting in a solution of quantum dots

with a narrow size distribution. The separation of the different stages of the reaction mixture during different steps of the synthesis can be understood from the degree of supersaturation of the monomers in the solution, see figure 2.6.

The first stage is the induction period that starts during the injection step. Here, the molecular precursors react to form monomers. Monomers are the basic constituents of the nanocrystal, so for a CdSe crystal the monomer would be a single [CdSe] unit. After precursor injection into a hot reaction mixture, the formation of monomers causes the degree of supersaturation to rise until a point of critical supersaturation is reached. At this critical point, the supersaturation is sufficiently high to form colloidal nanocrystals in the solution, during the nucleation stage. Nucleation will cause the concentration of monomers to drop below the critical supersaturation, after which nucleation is terminated and the growth stage is started. During the growth stage monomers will attach to the nanocrystal surface until the supersaturation declines. It should be noted that at this point, undesired Ostwald ripening may set in that causes polydispersity of the crystals. To prevent this, the solution is usually cooled a certain time after injection [1, 40, 49, 50].

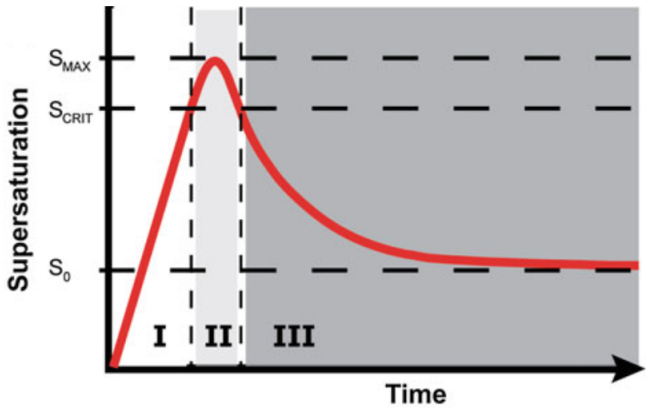

Figure 2.6: Graph showing the dependence of the different stages of colloidal nanocrystal synthesis on the degree of monomer supersaturation (S). S is plotted against the time. S_0 is the solubility limit of the solvents. Stage I is the induction period. When S reaches S_{CRIT} the nucleation will begin in stage II. Nucleation is terminated when supersaturation drops below S_{CRIT} upon which stage III, the growth stage, is started. This will continue until S_0 is reached. Graph reproduced from reference [51].

The driving force for the particle nucleation can be explained based on the change in total Gibbs free energy [49, 50]. An expression for ΔG_{TOT} is given in equation 2.3.

$$\Delta G_{TOT} = \Delta G_V + \Delta G_S \tag{2.3}$$

Here, we can see that the total change in Gibbs free energy is dependent on ΔG_V, the free energy of the volume of the particle, given in equation 2.4 and ΔG_S, the free energy of the surface of the particle, given in equation 2.5.

$$\Delta G_V = \frac{3}{4}\pi r^3 \rho \Delta\mu \tag{2.4}$$

The free energy for the volume (ΔG_V) is given by the product of the particle volume, where r is the radius, the density ρ and the change in chemical potential difference $\Delta\mu$. $\Delta\mu$ can be approximated with $-kT \ln S$, where S is the supersaturation. This makes the term for ΔG_V negative, which is correct since the systems energy is lowered by the formation of molecular bonds in the crystal. The surface free energy (ΔG_S) is equal to the product of the surface area, where r is the radius, and the interfacial tension γ. The formation of an interface between the crystal and the solution is not a spontaneous process, so ΔG_S is positive.

$$\Delta G_S = 4\pi r^2 \gamma \tag{2.5}$$

When the terms are put together, the expression for ΔG_{TOT} becomes equation 2.6.

$$\Delta G_{TOT} = -\frac{3}{4}\pi r^3 \rho k T \ln S + 4\pi r^2 \gamma \tag{2.6}$$

ΔG_V and ΔG_S are both dependent on r but have opposite signs. At a certain r, ΔG_{TOT} is maximized. This radius is referred to as the critical radius r_C and its expression is given in equation 2.7. When the size of the particle increases above r_C, growth of the crystal will be spontaneous. A graphical demonstration of the dependence of ΔG on the particle radius is displayed in figure 2.7.

$$r_C = -\frac{2\gamma}{\rho k T \ln S} \tag{2.7}$$

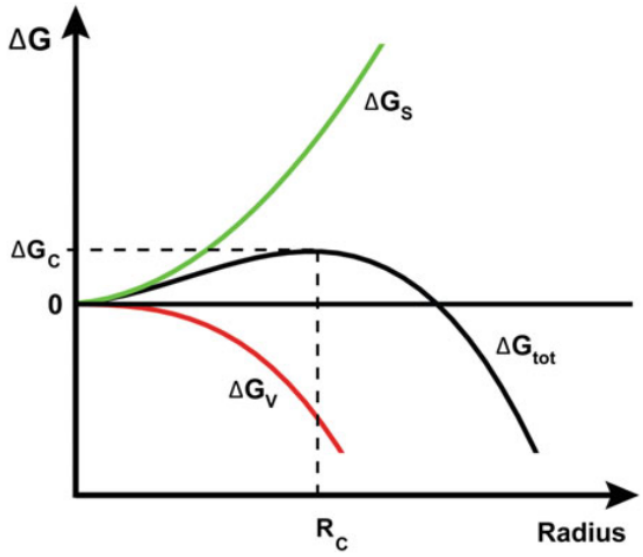

Figure 2.7: The dependence of the Gibbs free energy on the particle radius. ΔG_V and ΔG_S are the change in Gibbs free energy of the particle volume and surface, respectively. The sum of these energies is the total change in free energy ΔG_{TOT}. The maximum of ΔG_{TOT} corresponds with the critical radius R_C. G_C denotes the minimum energy required to reach R_C and subsequently the particle growth activation energy. Graph reproduced from reference [51].

2.4 Doping the quantum dots

The doping of a material is the intentional introduction of impurity atoms into its crystal lattice, thereby changing the material properties [25, 52, 53]. Doping can be used to further alter the electronic structure of a quantum dot. If a luminescent species is introduced, a quantum dot in its excited state can transfer its energy to the dopant and as a result, the dopant emission an be observed. Over the last decades several strategies to introduce impurity elements into colloidal quantum dots have been developed. This subsection will cover nucleation doping, growth doping and cation exchange, the most commonly used doping techniques.

The nucleation doping strategy relies on the introduction of the impurity atom in the form of a molecular precursor during the nucleation stage of the nanocrystals [25, 53]. A nucleus containing the dopant atom is synthesized. If incorporation of the dopant into the crystal lattice is favorable, the nucleus can be grown into a mature quantum dot by deposition of the semiconductor monomers. Nucleation doping leads to crystals that are either homogeneously doped or have their dopant exclusively localized in their center. This localization of the dopant ensures efficient energy transfer, resulting

in particles that show only emission of the luminescent dopant, and complete quenching of the band edge emission of the quantum dot [25, 53].

In growth doping, the impurity element is introduced after the formation of a quantum dot. The dopant is effectively attached to the nanocrystal surface. The nanocrystal is subsequently overgrown with a shell of the same or a different material, encapsulating the dopant [25, 53]. After growth doping, the dopants are usually localized at a fixed distance of the particle core. Energy transfer to the dopant will occur partially, so that quantum dot band edge emission is observed as well as the dopant emission [25, 53].

The cation exchange doping strategy relies on the exchange of cations in the crystal lattice of a quantum dot with different cations in the mixture. For the cation exchange to be succesful, both the outgoing and the entering species must have a high mobility in the crystal lattice, which means that they must be sufficiently small [54]. Furthermore, a driving force for the exchange must exist in the form of a lowered lattice energy after exchange or a higher solubility in the liquid medium for the leaving species [54]. When these conditions are satisfied, a dot can be homogeneously doped.

2.4.1 Self-purification

The nanoscale offers new solution doping strategies, but poses new challenges as well. One of the problems that is encountered during the synthesis of doped nanocrystals is the self-purification of the crystal lattice. To lower its lattice energy, a nanocrystal may eject an impurity atom [52]. For lattice ejection of the dopant species to be possible, the system must be in thermodynamic equilibrium with its environment. This means that at high temperatures the nanocrystal will form an energetically more favorable lattice and dopant ions are expelled.

2.5 Lanthanide ions

The lanthanides form a series of chemical elements where each succeeding lanthanide has an extra electron in its 4f shell. Together with the chemically similar elements scandium and yttrium, they are referred to as the rare earth elements [55].

Lanthanides are commonly found in the oxidation state +3 and Ln^{3+} (Ln being the informal chemical symbol to denote any of the lanthanide elements) has the general electron configuration of $[Xe]4f^n$. Here, the 4f orbitals are shielded by the further extending 5s and 5p orbitals. Since the 5s and 5p orbitals are the ones that interact with the environment and only the electronic structure of the 4f orbitals changes, the series of lanthanides is chemically very similar. The most noticeable chemical difference between the lanthanides is the decrease ionic radius over the series. This is known as the lanthanide contraction and is explained by the increase in nuclear charge. The 5s and 5p electrons are poorly shielded by the 4f electrons, so with increasing nuclear charge the extension 5s and 5p orbitals decreases [56].

While the lanthanide ions are chemically very similar, they are scientifically studied largely because of their spectroscopically unique intra 4f transitions. For a Ln^{3+} ion with configuration $[Xe]4f^n$, there are $\binom{14}{n}$ different electron distributions over the 4f shell. This gives rise to multiple energy levels within the shell, which are displayed in the diagram displayed in figure 2.8, created by the group of Dieke based on their spectroscopic and theoretical work [57].

The different energy levels in the Dieke diagram are denoted with term symbols that contain information on the quantum numbers of the configuration. The term symbols can be read as $^{2S+1}L_J$, where S is the total spin momentum quantum number ($\sum m_s$) and L is the total orbital momentum quantum number ($\sum m_l$). The expression for L is the letter S, P, D, F, ..., corresponding with $\sum m_l =$ 0, 1, 2, 3, ... In heavier atoms, the spin momentum quantum number and orbital momentum quantum number combine to form the total angular momentum quantum number J ($\sum (m_s + m_l)$). The ground state term symbol can be found by applying Hund's rules: S is maximized first, then L. The value for J in the ground state is L - S for $n < 7$ and L + S for $n \geq 7$.

As an example we take Yb^{3+}. The electronic configuration of Yb^{3+} is $[Xe]4f^{13}$. Distribution of these 13 electrons over the 7 4f sub-orbitals and applying Hund's rules yields the maximum S of 1/2 ($7 \times 1/2 + 6 \times -1/2$) and the maximum L of +3 ($2 \times 3 + 2 \times 2 + 2 \times 1 + 2 \times 0 - 2 \times 1 - 2 \times 2 - 3$),

corresponding with F. Since $13 > 7$, $J = L + S = 7/2$. The ground state term symbol then becomes $^2F_{7/2}$. The first excited state corresponds with a change in angular momentum and is $^2F_{5/2}$.

The shielding of the f orbitals has been well demonstrated in the optical spectra of the lanthanides. The f $\rightarrow$ f transitions yield fine line emission bands with a very small Stokes shift, because the f orbitals are shielded from their environment and do not partake in chemical bonds. This also has the effect that crystal field splitting (indicated in the Dieke diagram by the width of a state) is minimal.

The f $\rightarrow$ f transitions are parity forbidden. Due to the forbidden nature of the transitions their molar extinction coefficient is very low and they absorb light only weakly. As a result of being parity forbidden, f $\rightarrow$ f transitions usually have a very long excited state life-time, on the order of milliseconds.

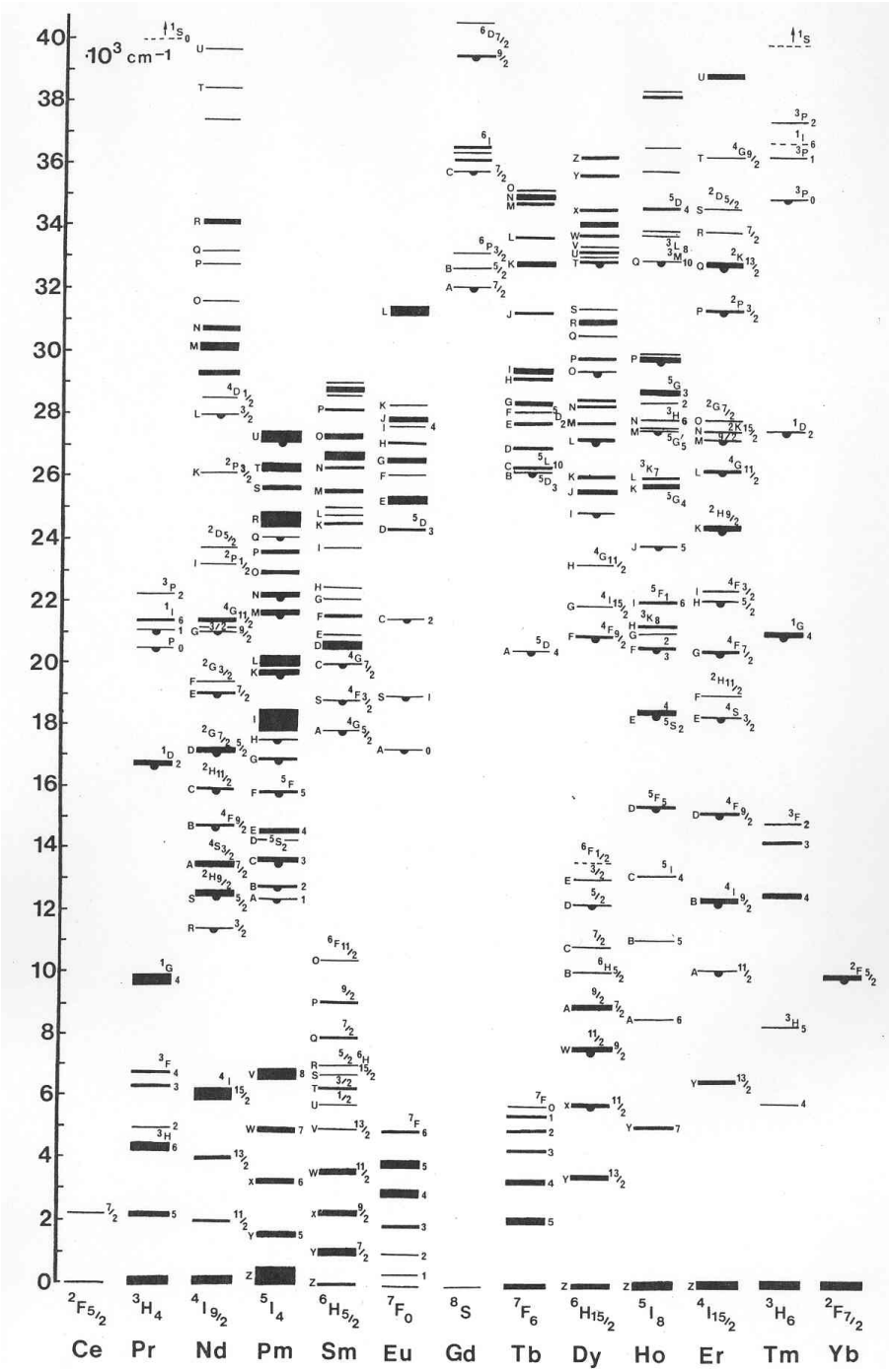

Figure 2.8: The 4f energy levels of the lanthanide series. The broadening of a level indicates its crystal field splitting. Reproduced from reference [57].

2.6 Energy transfer

Upon absorption of a photon, an electron is promoted to an energetically higher excited state. From this excited state, the electron can lose its energy either by emission of a photon, or by transferring its energy to another system. The focus of this thesis is on the energy transfer of the excited state of a quantum dot to its Yb^{3+} dopants. This section is dedicated to explaining the postulated mechanism for this energy transfer. Non-radiative energy transfer is discussed as well.

2.6.1 Ytterbium doped quantum dots

Energy transfer from the quantum dot in its excited state to the dopant needs to occur to observe Yb^{3+} dopant emission upon excitation of its quantum dot host. The energy difference between the quantum dot band gap and the energy difference between the $^2F_{5/2}$ excited state and the $^2F_{7/2}$ ground state of Yb3+ is relatively large (on the order of 7000 cm^{-1}). This energy difference is much higher than the lattice vibration energy of the quantum dot host material (ca. 200 cm^{-1} for CdSe [58] and ca. 300 cm^{-1} for InP [59]), so direct energy transfer assisted by phonons is unlikely. Therefore, to describe this process, a two step mechanism has been proposed: in the first step, the electron in the conduction band of the quantum dot reduces the Yb^{3+} ion, yielding Yb^{2+}. In the second step, the Yb^{2+} ion is oxidized by the hole in the valence band of the quantum dot, which results in a Yb^{3+} ion with an electron in its $^2F_{5/2}$ excited state. The energy transfer mechanism is depicted schematically in figure 2.9. After the energy transfer, emission upon relaxation to the $^2F_{7/2}$ ground state may be observed.

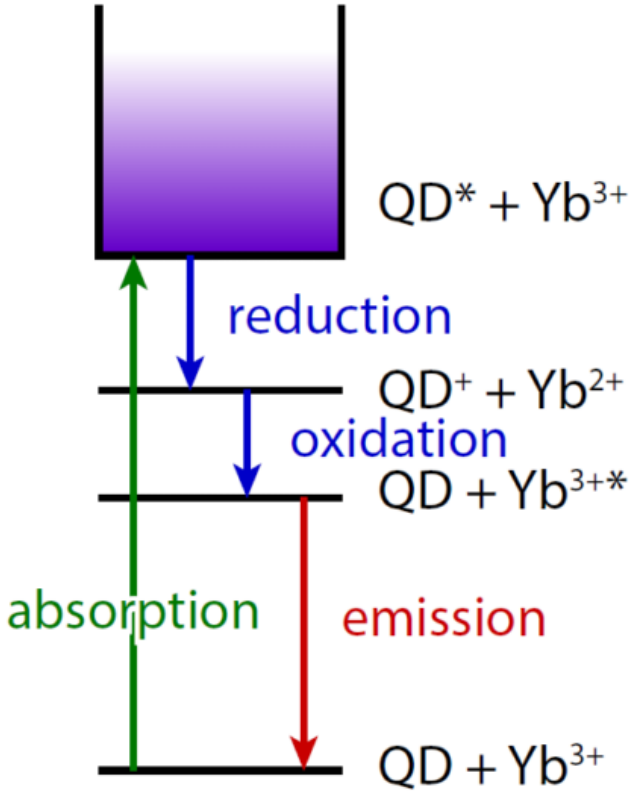

Figure 2.9: Schematic depiction of the quantum dot to Yb^{3+} energy transfer mechanism. A photon is absorbed, promoting an electron from the valence band to the conduction band, leaving behind a hole. The electron reduces the Yb^{3+} to form Yb^{2+}, which is then oxidized by the hole, yielding Yb^{3+} in its $^2F_{5/2}$ excited state. This excited state may then relax to the $^2F_{7/2}$ ground state by emission of a photon. Image reproduced from [60].

2.6.2 Multi-phonon relaxation

The energy of an excited state may also be relaxed by the release of phonons. Phonons are the vibrations of molecular bonds or lattices. As a general rule, an excited state will only decay via multi-phonon relaxation by coupling with five phonons or less. For ytterbium, the energy difference between its $^2F_{5/2}$ excited state and its $^2F_{7/2}$ ground state is about 10000 cm^{-1} (see figure 2.8). This means that, assuming the vibrational energy of a semiconductor to be around 250 cm^{-1}, in a semiconductor lattice, the excited state of Yb^{3+} will not decay non-radiatively. However, organic solutions and ligands can have vibrational energies around 3300 cm^{-1} for an O-H stretching vibration and around 3000 cm^{-1} for a C-H stretching vibration, so an Yb^{3+} ion in contact with a surface ligand or the quantum dot solute can have its excited state decay non-radiatively by coupling to molecular vibrations. This energy transfer will have a detrimental effect on the lanthanide luminescent quantum yield and the lifetime of its excited state.

2.6.3 Electron trapping

Although the number of phonons required to bridge the band gap of a quantum dot is too large to allow the excited state of a dot to decay via multi-phonon relaxation (more than 50 would be required for CdSe), non-radiative decay of a quantum dot is still possible via the capture of the excited electron by a trap state. Trap states are energetic states in between the semiconductor nanoxrystal band gap, formed by discontinuities in the nanocrystal lattice, such as lattice defects and surface states [1, 40]. After relaxation of a conduction band electron to a trap state, it can recombine with a valence band hole upon emission of an energetically lower photon, process 2 in figure 2.10. Alternatively, the energy can non-radiatively decay via multiple trap states until the quantum dot ground state is reached as displayed in process 3 in figure 2.10.

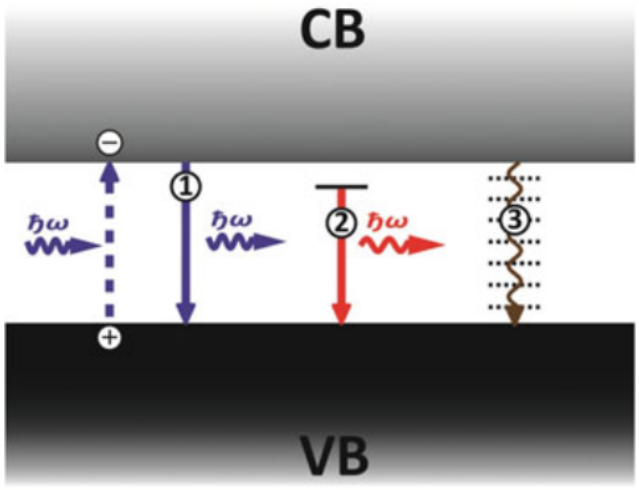

Figure 2.10: Schematic represantation of possible modes of quantum dot exciton decay. Decay process 1 is the relaxation of the exciton to the valence band upon emission of photon with energy equal to the band gap. Process 2 is the non-radiative decay to a trap state followed by radiative emission at a lower energy than the band gap. Process 3 is the non-radiative decay of a quantum dot exciton via multiple trap states. Image reproduced from reference [46].

Chapter 3

Incorporation of Yb^{3+} into InP quantum dots

Abstract

A growth doping strategy to attach Yb^{3+} ions to InP quantum dots is described. A hot-injection method is employed to synthesize InP and In(Zn)P colloidal semiconductor nanocrystals that absorb and emit light in the visible region. Yb^{3+} ions are coupled to the quantum dots in a doping step, after which Yb^{3+} emission at 975 nm corresponding with the $^2F_{5/2} \rightarrow {}^2F_{7/2}$ transition can be observed upon quantum dot excitation in the visible region, indicating the possibility of energy transfer from InP quantum dots to Yb^{3+} lanthanide ions. The optimal Yb:QD ratio in the synthesis is found to be 360:1. The short lifetime of the Yb^{3+} excited state is an indication that the dopant ions reside merely at the quantum dot surface, but washing the quantum dots multiple times does not decrease the Yb^{3+} emission, indicating that they are strongly bound to the nanocrystals. To incorporate the surface resident Yb^{3+} dopant ions, several different shell materials are applied to the doped quantum dots, each resulting in a decrease in Yb^{3+} emission, possibly as a result of nanocrystal self-purification. An increase of Yb^{3+} emission upon quantum dot excitation is observed when In(Zn)P quantum dots are used as cores instead of InP quantum dots, this increase is attributed to the passivation of trap states by Zn.

As an alternative doping method, a one pot synthesis route to dope In(Zn)P/ZnS quantum dots with Yb^{3+} is utilized based on an adaption of a previous publication describing the incorporation of Eu^{3+} into In(Zn)P/ZnS quantum dots, but this strategy yielded no Yb^{3+} emission upon quantum dot excitation.

3.1 Introduction

In this chapter, the development of a synthetic procedure to fabricate InP quantum dots doped with Yb^{3+} ions will be described. As a doping strategy, the growth doping method is chosen: first colloidal semiconductor nanocrystals will be synthesized, to the surface of these nanocrystals dopant ions will be attached, and finally the surface residant ions will be overgrown with a shell material.

As a colloidal semiconductor core material, indium phosphide (InP) is chosen. InP quantum dots have the benefit that, compared to for example cadmium selenide (CdSe) quantum dots, its intrinsic toxicity is reduced as a result of the covalent nature of its crystal lattice [35, 36]. Furthermore, the charge of the indium cations in the lattice is similar to that of trivalent lanthanide ions, which may facilitate exchange of the cations. Potential dissadvantages of InP as a host lattice may be the 4-fold coördination of cations in the zinc blende lattice and the smaller ionic radius of indium compared to ytterbium. InP and In(Zn)P quantum dot cores will be synthesized via a hot-injection technique derived from the work of Song *et al.* [36]. This synthesis method forgoes the use of the pyrophoric tris(trimethylsilyl)phosphine phosphor precursor in favor of the less reactive tris(dimethylamino)phosphine phosphor precursor.

As a trivalent lanthanide dopant ion, Yb^{3+} is chosen. The benefits of Yb^{3+} include the relatively simple electronic structure compared to different lanthanide ions and that its characteristic emission line corresponding with the $^2F_{5/2} \rightarrow {}^2F_{7/2}$ transition is well separated from the visible region where InP quantum dot band edge emission is expected, making for more facile interpretation of the emission spectra.

The final step in the growth doping procedure will be the overgrowth with a shell material. The effect of using several different encapsulating shell materials is investigated: sulfur, phosphor, zinc sulfide, zinc selenide and cadmium selenide.

A previous publication by the group of Reiss and coworkers described a one pot approach to the growth doping of In(Zn)P/ZnS with Eu^{3+} ions [34]. An adapted version of this synthesis is utilized to investigate incorporation of Yb^{3+} ions into In(Zn)P/ZnS colloidal semiconductor nanocrystals as well.

Emission of the ytterbium dopant ions upon quantum dot band edge excitation will be analyzed to describe the nature and location of the dopant ions.

3.2 Experimental methods

3.2.1 Chemicals

Selenium (Se, 99.999 %) was purchased from Alfa Aesar. Bis(trimethylsilyl)sulfide ($S(TMS)_2$, 98 %) and tris(trimethylsilyl)phosphine ($P(TMS)_3$, 98 %) were purchased from Fisher Scientific. 1-Butanol (Bu OH, 99.8 %), 1-dodecanethiol (DDT, 98+ %) indium acetate ($In(Ac)_3$, 99.99 %), methanol (MeOH, 99.9 %), myristic acid (MA, 99 %), 1-octadecene (ODE, 90 %), oleic acid (OA, 90 %), oleylamine (OLAM, 70 %), toluene (99.8 %), ytterbium acetate ($Yb(Ac)_2$, 99.9 %) and zinc chloride (98+ %) were purchased from Sigma-Aldrich. Reagents were used as received with the exception of ODE and OLAM, which were degassed under vacuum at 150 °C while stirring for 4 hours.

3.2.2 InP quantum dot synthesis

To synthesize InP core quantum dots, an adaptation of the hot injection approach described by Song et al. is employed [36]. The synthesis has been adapted to use different amounts of zinc precursor and was performed at different scales. The varied reaction parameters are described in appendix A.

In general, the synthesis was performed by introducing 0.199 g $InCl_3$ (0.9 mmol), 0.122 g $ZnCl_2$ (0.9 mmol) and 5 mL OLAM (15.2 mmol) into a 3-neck round-bottom flask fitted with a vigreux column under inert conditions in a glove-box. This mixture was then stirred and heated to 220 °C. Upon reaching this temperature, a mixture of 0.25 mL $P(DMA)_3$ (1.35 mmol) and 1 mL OLAM (3.04 mmol) was quickly injected into the flask. The temperature of the reaction mixture was kept at 190 °C after the injection for 5 minutes before cooling to room temperature. After cooling, the reaction mixture was washed by addition of 2 volume equivalents of MeOH and 2 volume equivalents of BuOH. The precipitate was separated from the liquid phase by centrifugation followed by decantation of the supernatant. The sediment was redispersed in 4 mL toluene.

3.2.3 Post-synthetic heating of InP cores

To investigate the effect of heating the InP cores after the synthesis, the dots were redispersed in ODE and heated to 240 °C while stirring for 1.5 hours. Upon cooling, the InP QDs were washed and redispersed in toluene before they were subjected to absorption and emission spectroscopy.

3.2.4 Yb^{3+} growth doping procedure

The growth doping procedure that was utilized to incorporate Yb^{3+} ions into InP quantum dots is based on a procedure described by Meijerink and coworkers to incorporate ytterbium into CdSe nanoparticles [33].

Yb precursor preperation

As an ytterbium precursor for the doping of InP with Yb^{3+} ions, ytterbium oleate is used. The preparation of $Yb(OA)_3$ proceeded as follows: in an Erlenmeyer flask, 0.42 g $Yb(Ac)_3{\cdot}(H_2O)_4$ (1.0 mmol) was weighted, 2 mL oleic acid and 8 mL ODE are were added. The mixture was brought under vacuum using a Schlenk-line and heated to 80 °C while stirring. After 30 minutes, the temperature was raised to 150 °C and reaction was allowed for 4 hours before cooling to room temperature. 10 mL ODE was added to decrease the viscosity yielding a 0.05 M $Yb(OA)_3$ solution.

Growth doping

The general approach for the growth doping of InP was as follows: under inert conditions in a glove-box, 3 mL OLAM and 9 mL ODE were added to a vial, together with a volume equivalent of 100 nmol InP quantum dots in toluene solution. The mixture was heated to 265 °C while stirring. The mixture was kept at this temperature for at least 30 minutes to allow the evaporation of toluene. After the toluene had evaporated, a volume of 0.05 M $Yb(OA)_3$ in ODE corresponding with a varying

Yb:QD ratio (see appendix B) was added in a slow drop-wise manner. The reaction was allowed for 30 minutes.

Encapsulation

After the Yb precursor reaction step, in several cases, encapsulation proceeded with either a S precursor or a P precursor. Using a S precursor, the mixture was cooled to 200 °C and a 340 μL volume of S precursor DDT (1.42 mmol) was slowly added in a drop-wise fashion. Reaction was then allowed for 2 hours before cooling to room temperature. Using a P precursor, the mixture was cooled to 190 °C and 150 μL of a 0.1 M solution of either $P(DMA)_3$ or $P(TMS)_3$ was added in a slow drop-wise manner. Reaction was allowed for 1 hour before cooling. In some experiments, the encapsulation step was forgone and the samples were cooled to room temperature 30 minutes after addition of the ytterbium precursor. After cooling, the particles were sedimented by addition of MeOH and BuOH, centrifuged, and redispersed in 4 mL toluene.

3.2.5 ZnS shell growth via Song method

After some doping syntheses, ZnS shells were grown over doped InP quantum dots, according to a procedure based on the protocol described by Song et al. [36]. The shell growth proceeded by introducing 2 mL InP:Yb^{3+} quantum dots in toluene (corresponding with 50 nmol of the quantum dots before doping) together with 3 mL OLAM and 9 mL ODE into a vial under inert conditions in a glove-box. The mixtures were heated to 205 °C while stirring and kept at this temperature for at least 30 minutes to allow the toluene to evaporate. 13.5 mg $ZnCl_2$ (0.1 mmol) and 165 μL DDT (6.9 mmol) were added in succession. Reaction of the shell precursors is allowed for 2 hours before cooling the mixture to room temperature. After cooling, the particles were sedimented by addition of MeOH and BuOH, centrifuged, and redispersed in toluene.

3.2.6 Rapid ZnS shell growth

As an alternative method to grow ZnS shells around doped InP quantum dots, a more reactive S precursor is used in combination with a shorter reaction time. In a glove-box, under inert conditions, 6.75 mL ODE, 2.25 mL OLAM and a volume of In(Zn)P:Yb^{3+} quantum dots in toluene corresponding with a pre-doping amount of 75 nmol quantum dots were added to a vial. Several reaction temperatures were tested, as displayed in appendix C. In a typical shelling procedure, the mixture was heated to 210 °C while stirring and kept at the elevated temperature for at least 30 minutes to allow the toluene to evaporate. After the toluene had evaporated, a 0.1 M $S(TMS)_2$ solution in ODE is added slowly and in a drop-wise manner in a volume corresponding with one, two, three or four mono-layers of ZnS per quantum dot, as calculated using the ZnS lattice parameters provided by Hotje et al. [61]. A few minutes after addition of the S precursor solution, a 0.1 M $Zn(OA)_2$ solution is added in the same volume in a slow drop-wise manner. Reaction is allowed for 20 minutes before cooling to room temperature and washing with MeOH and BuOH, centrifugation and redispersion in toluene.

3.2.7 Se based shells

In some cases, InP particles doped with Yb^{3+} ions were overgrown both with ZnSe and CdSe shells. ZnSe shell growth proceeded by adding 6.75 mL ODE, 2.25 mL OLAM and 0.75 mL InP:Yb^{3+} quantum dots in toluene to a vial under inert conditions in a glove-box (the amount of quantum dots corresponds with ca. 37.5 nmol quantum dots pre-doping). The mixture was heated to 240 °C while stirring and toluene was allowed to evaporate for at least 30 minutes. After toluene had evaporated, a 0.1 M Se dispersion in ODE is added slowly and drop-wise in a volume corresponding with either one or two mono-layers of ZnSe, as calculated using the ZnSe lattice parameters described by Hotje et al. [61]. A few minutes after addition of the Se precursor dispersion, an equal volume of $Zn(OA)_2$ was added in the same drop-wise manner. Reaction was allowed for 30 minutes before cooling to room temperature and washing by addition of MeOH and BuOH, centrifugation and redispersion in 3 mL toluene. Deposition of CdSe shells proceeded in exactly the same fashion, with the exception that

instead of a Zn precursor, $Cd(OA)_3$ is used and to calculate the volumes needed for one and two monolayers of CdSe, CdSe lattice parameters were used as described in the same publication by Hotje et al. [61].

3.2.8 Doping via Reiss method

A procedure to synthesize Eu^{3+} doped In(Zn)P/ZnS core/shell particles developed by Reiss et al. [34] is adapted to use a hot injection approach for the synthesis of the cores and an Yb-precursor for dopant incorporation.

As an In precursor for the In(Zn)P cores, $In(MA)_3$ was used. A 0.1 M $In(MA)_3$ precursor was prepared by weighting 584 mg $In(Ac)_3$ (2 mmol) and 1370 mg myristic acid (6 mmol) in an erlenmeyer flask. 20 mL ODE was added and the mixture was brought under vacuum using a Schlenk-line. The mixture was heated to 120 °C while stirring and kept at this temperature for 5 hours.

In(Zn)P core particles were synthesized using a hot injection method. Under inert conditions in a glove-box, to a 3-neck roundbottom flask fitted with a vigreux column 1 mL 0.1 M $In(MA)_3$ solution, 126 mg Zn stearate (0.2 mmol) and 7 mL ODE was added. The mixture was heated to 200 °C while stirring. After reaching 200 °C, a mixture of 1 mL ODE and 15 μL $P(TMS)_3$ was rapidly injected. After injection, the temperature of the mixture is kept at 190 °C for 10 minutes. The mixture was then cooled to 80 °C. Dopant introduction then proceeded by adding 0.6 mL 0.05 M $Yb(OA)_3$ in ODE (prepared in the same manner as described in section 3.2.4) in a slow drop-wise manner. The temperature was kept at 80 °C for 100 minutes before it was increased to 120 °C and kept there for 20 minutes. For the ZnS shell growth a mixture of Zn ans S precursors is prepared by adding 1 mL 0.1 M $Zn(OA)_3$ in ODE and 1 mL 0.1 M $S(TMS)_2$ in ODE to 2 mL ODE and stirring at 80 °C. This mixture was slowly added to the reaction mixture over 20 minutes after the doping step. The reaction mixture was then kept at 120 °C for 20 minutes and before being cooled to room temperature. The mixture was washed by addition of 20 mL acetone, centrifugation, and redispersion in 2 mL toluene.

3.2.9 Characterization

TEM was performed using a FEI Tecnai microscope operating at 120 kV. Absorption spectra were recorded with a Perkin Elmer Lambda 950 UV/VIS/NIR spectrophotometer. Emission and excitation spectra were recorded with an Edinburgh Instruments FLS 920 spectrofluorometer with a 450 W Xe lamp for excitation. Emission was detected using a Hamamatsu R928 photomultiplier tube for detection in the visible region and a nitrogen cooled R5509-72 photomultiplier tube for detection in the infrared region. Lifetimes were measured using the same detector as the emission after pulsed excitation using an Optical Parametric Oscilator (OPO) lasing system. Samples for spectroscopy were prepared by diluting a purified reaction mixture with toluene and were measured in quartz cuvettes.

3.3 Results and discussion

Yb^{3+} doped InP quantum dots were synthesized using a growth doping approach. The procedure to synthesize the particles is comprised of three steps: synthesis of an InP quantum dot core, attachment of the dopant ions to the quantum dot surface, and the overgrowth of a shell material over the dots to encapsulate the dopant ions. In this section the results of several different synthetic approaches to these steps are presented and discussed.

3.3.1 InP cores

As a first step to create InP:Yb^{3+} quantum dots, InP quantum dots were synthesized. The protocol chosen for the synthesis is an adaptation of the hot injection method described in the work of Song and co-workers [36] and a detailed description of the synthetic method is given in section 3.2.2. In the initial experiments, zinc has not been used as the existence of Zn^{2+} ions at the quantum dot surface was postulated to inhibit the adsorption of Yb^{3+} due to the repelling positive charges of both cations.

The obtained InP semiconductor nanocrystal dispersions were typically orange to red in color and did not emit light upon UV-lamp excitation, an early indication of the poor expected optical properties of bare InP QDs caused by non-radiative exciton recombination at surface states.

The dots were subjected to spectroscopic investigation. Of the quantum dot dispersion, both absorption of light over the visible range and emission upon QD core excitation were measured. Figure 3.1 shows a typical absorption spectrum of a dispersion of InP QDs in toluene. An increasing absorbance from 650 nm to 300 nm with a shoulder around 550 nm can be observed, corresponding with the observed orange to red color. In the quantum dot electronic structure, as explained in section 3.2.2, discrete energy levels are expected above and below the valance and conduction bands respectively. These discrete energy levels are expected to correspond with discrete absorption peaks in a monodisperse QD dispersion. The absence of discrete peaks in the InP QD absorption spectrum indicates a polydisperse sample with a broad QD size distribution. A possible explanation for this degree of polydispersity is the relatively low reactivity of the precursors used during the hot-injection. The low reactivity causes the nucleation event of the QD synthesis to take place over a longer time. During this time, deposition of monomers onto the nuclei will take place as well, which has the result that earlier formed nuclei grow into larger QDs and a larger size distribution in the QD sample is obtained [35, 36].

Although the size distribution in the spectrum in figure 3.1 is broad, the lowest energy absorption of the $S_h \rightarrow S_e$ transition can still be observed in the form of the shoulder at 550 nm. Using this absorption wave-length, the average size of the QDs and their concentration in the dispersion can be estimated using an empirically derived fitting function derived by the group of Xie [62]. Furthermore, an estimate of the QD concentration in the sample can be made using the absorbance at 344.4 nm and the optical properties of InP [63]. The InP quantum dot sizes and concentrations calculated in this manner were used to determine the right amounts of InP quantum dots during the doping experiments.

The bare InP QDs did not display light emission upon excitation at 400 nm. The lack of emission is most likely caused by trap states created by the dangling bonds of the unbound phosphor atoms at the QD surface. These surface traps capture the excited electron promoted by the absorbed light causing it to decay non-radiatively via multiple trap states in the manner explained in section 2.6.3 (process 3).

Another commonly used technique to analyse QDs is transmission electron microscopy (TEM). Figure 3.2 displays a typical TEM image of InP quantum dots. As can be seen, the contrast of the QDs with respect to the background is extremely low. The low contrast is due to high amount of electrons transmitted by the InP QDs. The quantum dots in the TEM images were deemed too poorly defined for a reliable size analysis.

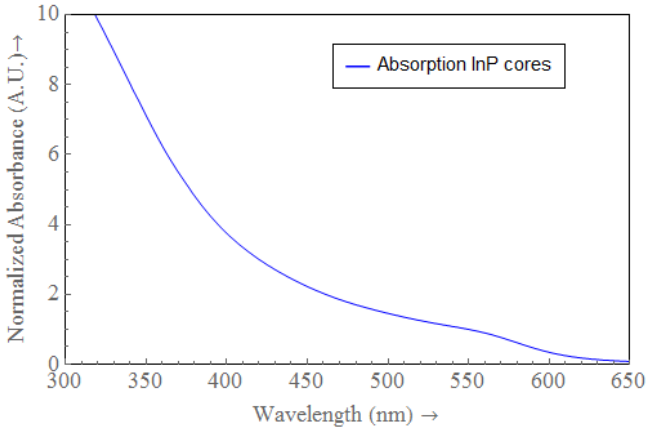

Figure 3.1: Typical absorption spectrum recorded from a dispersion of bare InP quantum dots in toluene. Absorbance increases towards the UV and a shoulder corresponding with the $S_h \rightarrow S_e$ transition is identified around 550 nm. The poorly defined absorption shoulder suggests a broad quantum dot size distribution.

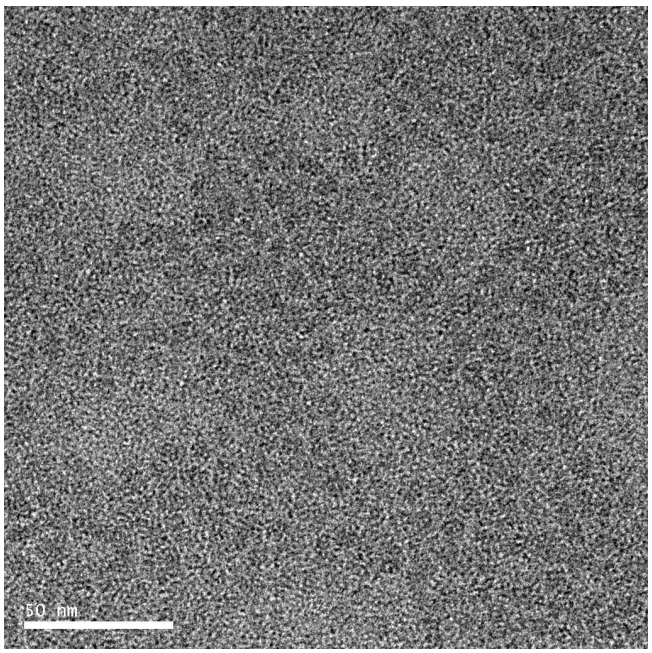

Figure 3.2: Typical TEM image of an InP QD sample. The contrast of the dots with respect to the background is very low.

3.3.2 Post-synthetic heating of InP cores

Figure 3.3 displays the absorption spectra of InP QDs before (blue) and after (red) being heated to . After the heating treatment, the absorption shoulder appears significantly more defined and shifted slightly to the red. A possible explanation for this observation is that after the hot-injection synthesis, the InP QDs have In and P material attached to their surface that is not completely incorporated into the crystal lattice. Heating these dots causes the surface to become more crystalline and as a result, their optical properties increase in a process known as surface reconstruction [40].

Figure 3.3 also shows an emission spectrum (green) obtained after excitation with a 400 nm light source. The spectrum displays two main features: a peak at 600 nm that overlaps with a broader band around 750 nm. The peak at 600 nm is assumed to be the band edge emission of the quantum dots that was not observed before the heating of the sample. The rise of this peak is also explained by the increased crystallinity of the QD surface. Incorporation of surface atoms into the InP crystal lattice decreases the number of dangling bonds and as a result, the number of surface traps is decreased as well. This has the effect that a decreased number of trap states exists inside the band gap, decreasing the rate of non-radiative decay. The broader band around 750 nm is likely the radiative decay of

electrons at trap states close to the QD valence bands [35].

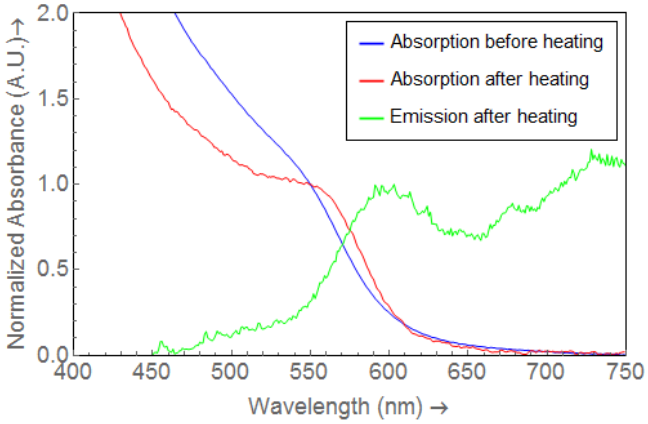

Figure 3.3: Displayed are the absorption spectrum of InP QDs before heating (blue) as well as the absorption (red) and emission (green) spectra of InP QDs after heating at 240 °C for 1.5 hours. After heating, the band edge absorption shoulder appears more well defined and shifted to the red. Excitation at 400 nm shows a band gap emission peak at 650 nm and trap state emission around 750 nm.

3.3.3 Growth doping InP quantum dots

The synthesized InP QDs were used as cores in growth doping experiments. The procedure to dope these cores was based on a protocol developed by Geitenbeek and Martín-Rodríguez [33]. As described in more detail in section 3.2.4, the cores were heated to 265 °C before a $Yb(OA)_3$ solution was added in a slow drop-wise manner. The incorporation of the dopant was allowed for 30 minutes before the reaction mixture was cooled to 200 °C, DDT was added to encapsulate the QDs with sulfur and its deposition was allowed for 2 hours before cooling and washing. On the resulting particles, absorption and emission spectroscopy were performed.

Representative absorption spectra obtained from both bare InP QDs (blue), undoped InP QDs encapsulated with DDT (red) and doped dots encapsulated with DDT (green) are compared in figure 3.4. Comparison of these spectra reveals a red-shift and better definition of the lowest energy absorption shoulder of InP QDs after reaction with DDT, an indication that S is successfully deposited onto the dots: the red-shift is caused by the leaking of the exciton wave-function into the S-shell material, decreasing its quantum confinement. The absorption shoulder of the sample of InP on which the doping procedure is applied displays an even further shift towards the red. This may be caused by a further increase in QD size by deposition of the dopant followed by S-shell overgrowth, decreasing the confinement of the exciton wave-function.

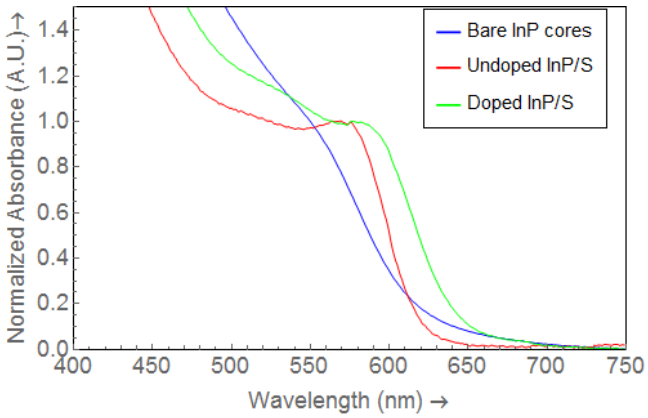

Figure 3.4: Comparative absorption spectra of bare InP QDs (blue), undoped InP QDs encapsulated with DDT (red) and doped dots encapsulated with DDT (green). A red-shift is observed after S-shell growth, possibly caused by leaking of the wave-function into the shell. The doped dots have their absorption shoulder shifted even further to the red, possibly due to the increase in QD size.

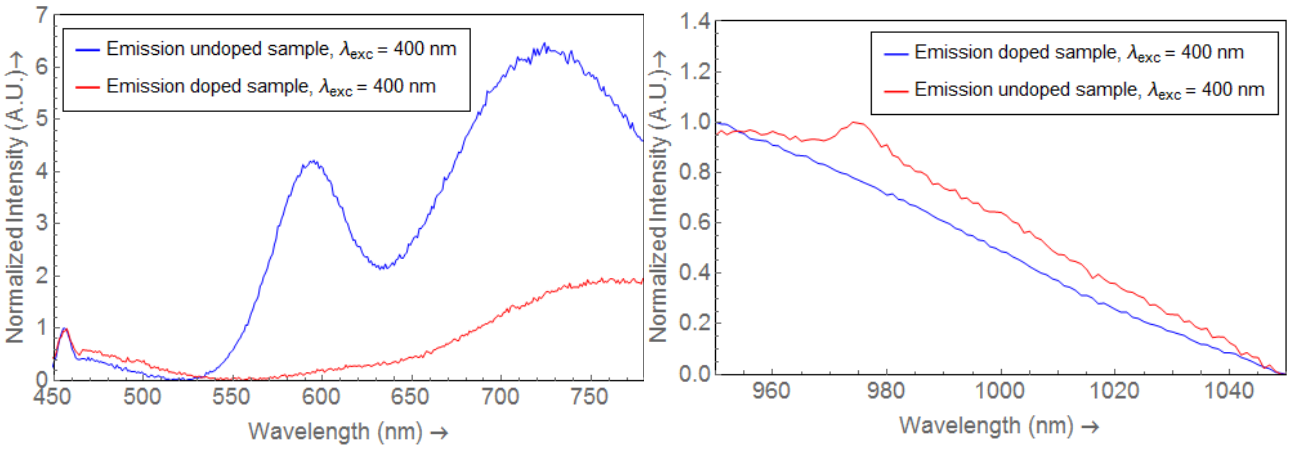

Figure 3.5: Spectra displaying emission of undoped (blue) and Yb^{3+} doped (red) InP/S QDs in the visible (left) and the IR (right) region. Spectra in the visible region display band-edge and trap state emission that is quenched and red-shifted upon application of the doping procedure. In the right spectra, a sloping baseline of trap emission is displayed and in the doped sample, Yb^{3+} emission can be seen at 975, corresponding with the $^2F_{5/2} \rightarrow {}^2F_{7/2}$ transition. All spectra were obtained after excitation at 400 nm.

Emission of the doped dots has been measured as well, both in the visible and the IR region. The visible emission of both undoped (blue) and doped (red) InP/S QDs upon excitation by a 400 nm light source is comparatively displayed in figure 3.5 (left). The spectra display a small peak at 460 nm, likely caused by Raman scattering of the toluene solvent (visible region emission spectra recorded on the same sample exciting at different wavelengths showed a corresponding shift in this peaks position). Upon growth of a S-shell around the InP dots, radiative decay after light absorption can be observed: the blue spectrum displays a peak at 590 nm, attributed to band-edge emission of the dots, and a broader peak around 720 nm, attributed to emission from trap states close to the QD conduction band. The rise of the visible band edge emission is an indication that the dangling bonds on the InP surface have at least been partially passivated by the S-shell grown with DDT. The red spectrum displaying the visible emission of the doped dots shows similar peaks to the undoped sample, except that the band edge emission peak is largely quenched. This may be an early indication of energy transfer to the ytterbium dopant. Another explanation for the decrease in emission is the possible formation of trap-states caused by crystal defects generated by the dopant ions. The spectrum of the doped sample has its excitonic emission peak shifted to the red, just like the band edge absorption, a further indication of larger QDs. The right spectrum in figure 3.5 displays emission in the near infra-red of both undoped and doped samples. The region of interest is between 950 and 1050 nm, since the Yb^{3+} $^2F_{5/2} \rightarrow {}^2F_{7/2}$ transition is expected to correspond with emission at 10^5 cm^{-1} or 1000 nm, as predicted by the Dieke diagram (figure 2.8). Comparing the spectra, a peak at 975 nm is identified in the doped sample. Although small, this peak may be attributed to the Yb^{3+} $F_{5/2} \rightarrow {}^2F_{7/2}$ transition upon excitation of the InP QD at 400 nm, providing a promising indication of successful coupling of the trivalent lanthanide ion to the InP core. Besides the Yb^{3+} emission, a sloping baseline of what is presumed to be trap emission is displayed in both spectra as well.)

3.3.4 Finding the optimal Yb^{3+} concentration

Experimenting with the growth doping procedure provided evidence of successful coupling of Yb^{3+} ions to InP cores by showing emission at 975 nm upon QD excitation at 400 nm. The intensity of this emission was still very low. To investigate whether the intensity of the Yb^{3+} emission could be improved, a series of experiments was performed to optimize the Yb^{3+} incorporation into the dots by varying the Yb^{3+} to QD ratio in the doping experiments over a wide range.

Of the resulting samples, the emission in the IR was measured upon excitation at 400 nm. These spectra are displayed in figure 3.6. The peak intensity at 975 nm is compared with respect to the trap emission of samples made with a 120:1 (blue), 240:1 (red), 360:1 (green), 480:1 (black), and

720:1 (pink) Yb:QD ratio. When the amount of Yb used is increased to 360 atoms per dot, the peak increases. Beyond the 360:1 ratio, the intensity appears to drop again, suggesting that 360:1 is the optimal Yb:QD ratio.

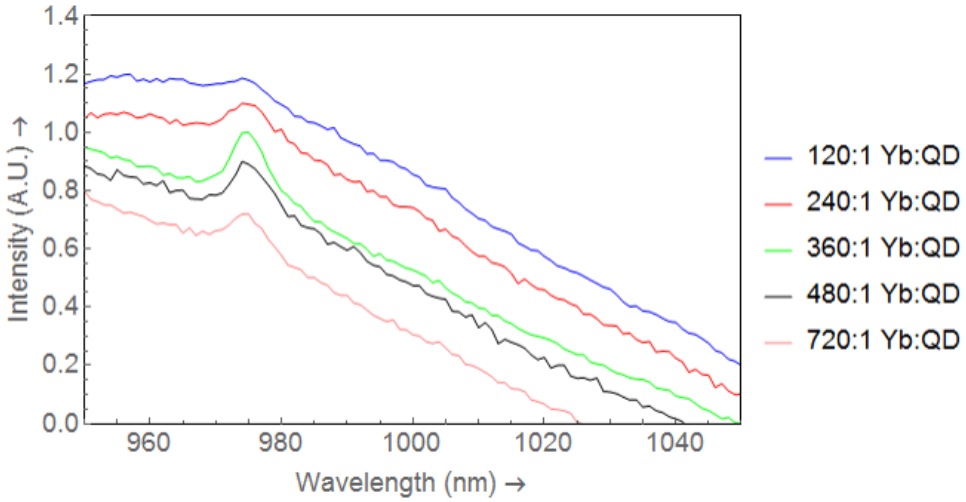

Figure 3.6: Comparative emission spectra of Yb^{3+} doped InP/S QDs prepared with a 120:1 (blue), 240:1 (red), 360:1 (green), 480:1 (black), and 720:1 (pink) Yb:QD ratio in the IR upon excitation at 400 nm. The spectra are vertically offset for clearer presentation. The emission peak at 975 nm appears highest with respect to the trap emission when the 360:1 ratio is used.

3.3.5 Further spectroscopy on InP:Yb^{3+}/S quantum dots

Emission at 975 nm upon excitation at 400 nm provided an early indication of energy transfer from InP QDs to Yb^{3+} ions. To further investigate the origin of the emission peak at 975 nm, an excitation spectrum is collected of a InP QD sample that has been doped with Yb^{3+}. Emission at 975 nm is measured over the excitation range from 400 to 750 nm. The excitation spectra are displayed in figure 3.7 (red). An absorption spectrum collected from this same sample is shown as well (blue) for comparison. The features of the excitation spectrum compare well with the electronic features of the InP quantum dot. A gradual increase of emission towards excitation in the UV is observed, as well as a shoulder at 560 nm similar to the one observed in the absorption spectrum. The similarity of the excitation spectrum to the absorption spectrum of the quantum dot suggests energy transfer of the InP QDs upon QD absorption to the Yb^{3+} dopant ions, followed by Yb^{3+} emission. A possible other origin of the QD excitonic features may be the trap state emission observed upon QD excitation (displayed in figure 3.5 (right)). The Yb^{3+} emission overlaps with the broad peak of trap state emission and the origin of the excitation spectrum can be either of the two.

To investigate the chemical environment of the Yb^{3+} dopant ions, fluorescence lifetime of the $^2F_{5/2}$ excited state is measured by excitation with a pulsed laser followed by time-resolved measurement of emission at 975 nm in a Yb^{3+} doped InP QD. The obtained decay curve is plotted and displayed in figure 3.8. The expected lifetime of the lanthanide excited state is expected to be on the order of milliseconds due to the f-f transitions being parity forbidden and its decay curve is expected to be mono-exponential. The obtained decay curve shows multi-exponential decay on a significantly shorter time-scale. The shortening of the lifetime can be explained by the coupling of the Yb^{3+} ions to vibrations of the ligands and molecules in the solution, resulting in multi-phonon relaxation as explained in section 2.6. This indicates that the Yb^{3+} ions reside merely at the InP quantum dot surface, instead of being incorporated into the crystal lattice.

3.3.6 ZnS shells grown via Song method

Spectroscopy performed on the Yb^{3+} doped InP QDs indicates successful coupling of the dopant ions to the InP cores and the possibility of energy transfer from dot to dopant, but Yb^{3+} emission upon

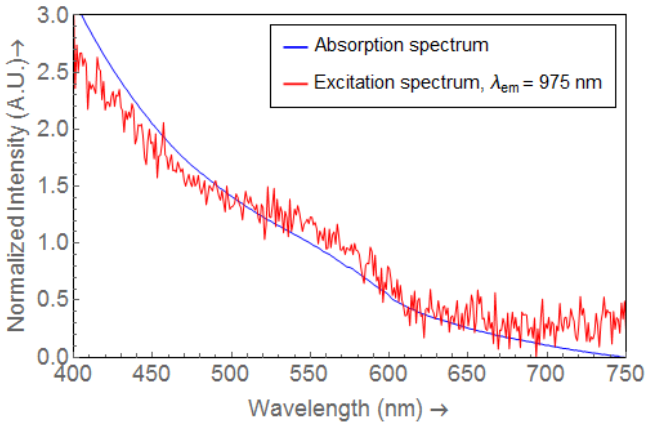

Figure 3.7: Displayed is the absorption spectrum obtained from an InP QD sample to which the Yb^{3+} doping procedure is applied followed by S overgrowth by reaction with DDT (blue), as well as the excitation spectrum obtained from the same sample by measuring emission at 975 nm while varying the excitation wavelength. Both spectra display the InP QD excitonic features, with the $S_h \rightarrow S_e$ transition shoulder identified at 560 nm. The overlapping spectra suggest the possibility of energy transfer to Yb^{3+} upon InP QD absorption, resulting in Yb^{3+} emission.

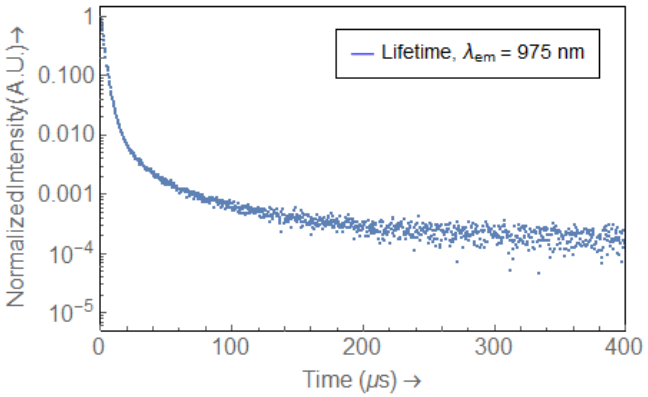

Figure 3.8: Decay curve obtained from an InP QD sample to which the Yb^{3+} doping procedure is applied followed by S overgrowth by reaction with DDT. Lifetime of the Yb^{3+} emission at 975 nm upon excitation with a pulsed laser at 560 nm is measured. The lifetime is on a very short timescale for a lanthanide f-f transition, possibly due to multi-phonon relaxation of the $^2F_{5/2}$ excited state. The multi-exponential nature of the decay curve can be explained by the overlap of the Yb^{3+} emission peak with the emission of InP QD trap states, which decay on different timescales.

QD excitation has a low intensity and QD trap state emission is observed as well. Furthermore, the measured lifetime of the Yb^{3+} excited state is on a very short timescale, indicating multi-phonon relaxation by coupling to ligand and solvent vibrations, suggesting that the dopant ions merely exist at the InP QD surface, without being incorporated into its crystal lattice.

These problems may be overcome by application of a ZnS type-I shell. The shell is deposited by reaction of $ZnCl_2$ with DDT at 200 °C for 4 hours in a procedure based on the method described by Song et al. [36].

The doped and shelled InP particles were analyzed with emission spectroscopy. In figure 3.9, typical visible (left) and IR (right) emission spectra obtained from the samples before (blue) and after (red) shell growth upon excitation at 400 nm are displayed. The main observation in the visible region is the rise of a broad band at 610 nm, likely caused by band edge emission of the quantum dots. The application of the type-I ZnS shell is assumed to passivate the dangling bonds on the QD surface, decreasing the number of trap states in the band gap and increasing the probability of radiative decay. Trap state emission is still observed in the form of a broad band from 700 nm and up, indicating that not all trap states have been passivated in the shell growth procedure. Comparing the IR emission spectra taken before and after shell growth reveals a quenching of the emission peak at 975 nm upon

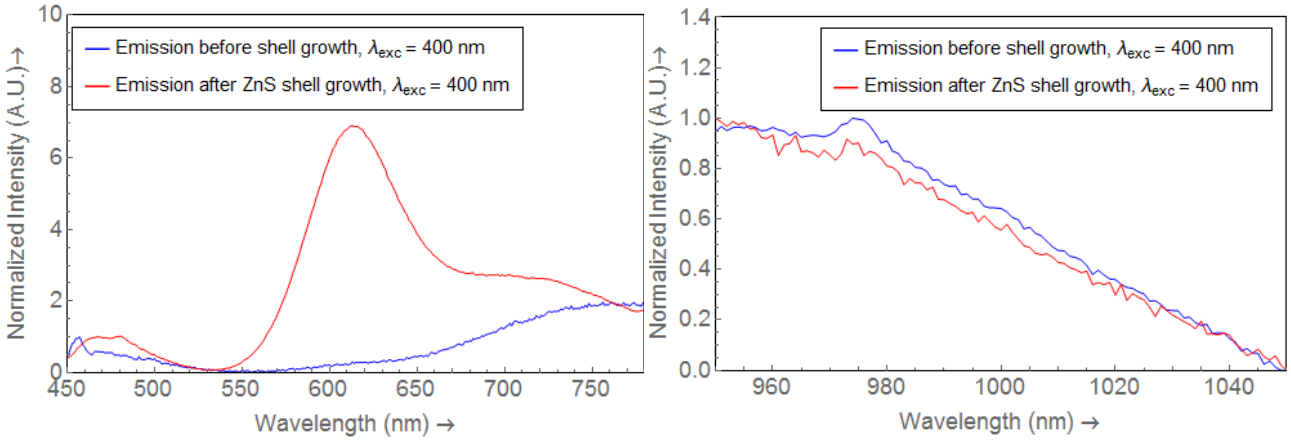

Figure 3.9: Emission spectra of InP:Yb^{3+}/S particles before (blue) and after (red) overgrowth with a ZnS via the Song method. Emission upon excitation at 400 nm is measured both in the visible (left) and the IR (right) region. Upon shell growth, the rise of peak at 610 is observed, presumably due to partial passivation of trap states at the InP QD surface resulting in a higher probability of band edge radiative decay. Both samples display trap state emission around 700 nm. Comparing the emission of the samples in the IR reveals the quenching of the Yb^{3+} emission peak at 975 nm.

application of a ZnS shell. Encapsulation of the surface-resident Yb^{3+} is expected to increase their emission intensity by shielding the ions from the vibrations of the organic molecules in the solution, thereby decreasing the probability of multi-phonon relaxation. The decrease in Yb^{3+} emission upon ZnS shell growth can be explained by the self-purification of the quantum dots: the doping procedure was performed at elevated temperatures for an extended time. These reaction conditions may have allowed the semiconductor crystal lattice to decrease its energy by ejecting the impurity ions. As a result, InP/ZnS QDs were formed and the Yb^{3+} ions were ejected to the ZnS shell surface or even into solution.

3.3.7 Doping InP without DDT encapsulation

Experimenting with the deposition of a ZnS shell onto the doped dots revealed the possibility of quantum dot self-purification, resulting in ejection of the Yb^{3+} ions, a process that may also be allowed during the deposition of S by reaction with DDT, the final step in the optimized doping procedure. To investigate whether the dopant emission may in fact be amplified by forgoing the reaction step where S is deposited, the previously optimized doping procedure is applied to a new batch of InP QD cores, both with and without the reaction step with DDT. On the resulting samples, emission spectroscopy is performed.

Figure 3.11 shows the emission in the visible region (left) upon excitation at 400 nm and in the IR (right) upon excitation at 355 nm of both Yb^{3+} doped InP encapsulated with DDT (blue) and without encapsulation (red). Emission of both samples in the visible region appears similar: both display a broad peak of trap emission and a lack of band edge emission. Comparing the emission in the IR shows that the peak at 975 nm in the samples that were encapsulated with DDT is diminished compared to the peak measured in the sample that was not encapsulated. These spectra suggest that treatment of the samples with DDT does not encapsulate the Yb^{3+} ions with a S shell. Instead, stronger Yb^{3+} emission is observed where no S layer is deposited after the doping step, suggesting that the DDT may be responsible for the decoupling of the dopant ions from the InP QD core surface.

3.3.8 The effect of washing doped dots

The low intensity of the measured Yb^{3+} emission peaks, in combination with their short excited state life times and the negative effect of shell-growth suggested that the dopant ions existed merely on the QD surface or even still in solution. To investigate whether the Yb^{3+} ions are weakly bound to the InP QD surface or dissolved in the toluene solvent of the sample, the doped dots were subjected to several

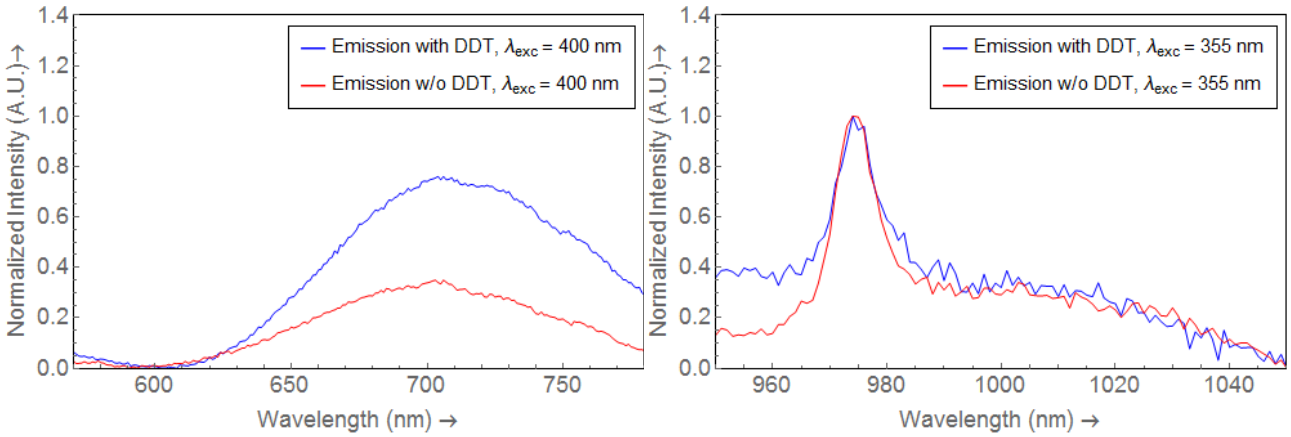

Figure 3.10: Emission spectra of InP:Yb^{3+} particles with (blue) and without (red) deposition of a S layer by DDT. Emission upon excitation at 400 nm is measured in the visible region (left) and at 355 nm in the IR region (right). The visible region displays a broad band of radiative decay from trap states in both samples. In the IR region, emission of the Yb^{3+} dopant is observed in both samples. This emission appears amplified with respect to trap state emission in the sample without DDT encapsulation.

additional washing steps and their optical properties were measured after each step. The washing proceeded by sedimentation of the QDs by MeOH antisolvent addition followed by centrifugation, and redispersion of the sediment in toluene. The washing step was repeated one, two, and three times. Of the washed samples, emission spectra in both the visible and IR region were measured upon quantum dot excitation.

The obtained spectra are displayed in figure 3.11. Emission is measured in the visible region (left) and the IR region (right) upon excitation at 355 nm of samples washed two (blue), three (red) and four (green) times. The small peaks displayed in the visible region are likely the result of scattering effects in the toluene solution. The broad peaks at 400 and 450 most clearly displayed in the sample that has been washed two times are assumed to be the result of emission of OLAM upon excitation at 355 nm (see appendix). These peaks are diminished when the sample is washed, suggesting the removal of OLAM ligands during the washing steps.

The IR region shows no distinct difference between the Yb^{3+} emission peaks at 975 nm. The similar emission peaks after several washing steps give an indication that the dopant ions are strongly bound to the InP QD surface instead of dissolved in the toluene solvent.

3.3.9 Encapsulation with a phosphor shell

Encapsulation of the Yb^{3+} atoms at the quantum dot surface with a S shell by reaction with DDT proved to be unsuccessful. The effect of the deposition of a phosphor shell onto doped dots is investigated to see if the trivalent P atoms can successfully overcoat the dopant ions. Two different P precursors are studied: the highly reactive $P(TMS)_3$ and the less reactive $P(DMA)_3$. The particles investigated were prepared via the previously optimized doping procedure, followed by reaction with one of the P precursor at 200 °C. The resulting particles were subjected to optical spectroscopy.

Figure 3.12 displays typical emission spectra in the visible region upon excitation at 400 nm (left) and in the IR region upon excitation at 355 nm, obtained from Yb^{3+} doped InP QDs overcoated with a layer of P by reaction with $P(TMS)_3$ (blue) and $P(DMA)_3$ (red).

Band edge emission and trap state emission are observed in both spectra in the visible region. The spectrum obtained from the sample where $P(TMS)_3$ is used has its visible emission peaks shifted slightly to the red, possibly the result of a larger QD due to the higher reactivity of the used P precursor, depositing more P onto the QD surface.

The emission spectra obtained in the infrared indicate that application of a P shell does not result in a notable increase in Yb^{3+} emission upon QD excitation. Trap state emission in the IR region appears higher in the sample where $P(TMS)_3$, possibly also due to the red-shift of the trap state

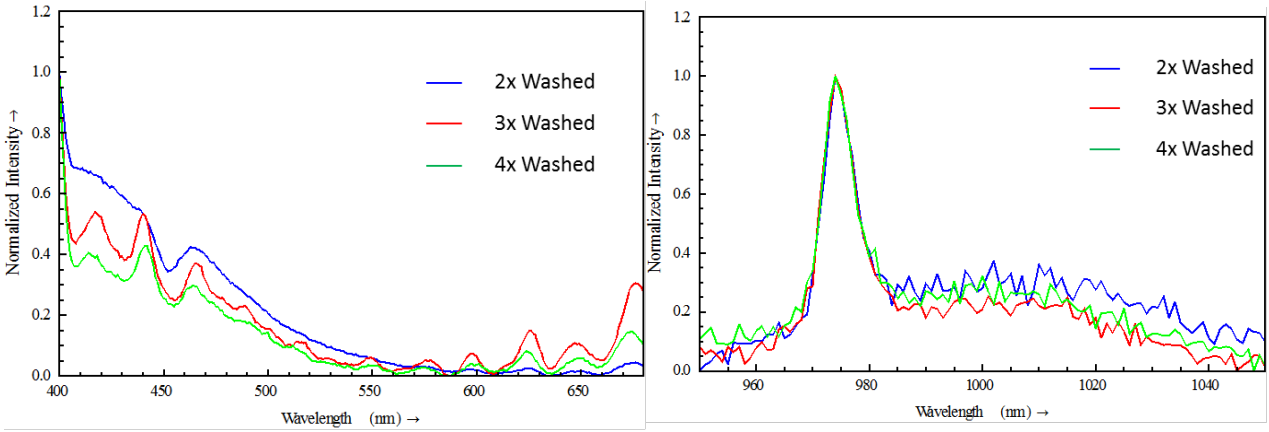

Figure 3.11: Emission spectra in the visible (left) and IR (right) region obtained upon excitation at 355 nm of InP:Yb^{3+} particles washed two (blue) three (red) and four (green) times. The spectra in the visible region display a multitude of small peaks associated with scattering effects in the toluene solvent. The broader peaks at 400 and 450 nm associated with OLAM emission reduce in intensity with each extra washing step, suggesting the stripping of OLAM ligands. Spectra in the IR region are very similar, indicating that the washing steps do not effect the Yb^{3+} ions because they are strongly bound to the InP QD surface.

emission due to increased QD size. Experiments with a P encapsulant do not provide convincing evidence of Yb^{3+} encapsulation.

3.3.10 Encapsulation with Se based shells

The work of Geitenbeek and Martín-Rodríguez [33] demonstrated the encapsulation of Yb^{3+} dopant ions on a CdSe QD core surface by overgrowth of selenium, so as an alternative to sulfur and phosphor based shells, the effect of shell growth over InP:Yb^{3+} QDs using selenium based materials is investigated as well. Yb^{3+} doped InP QDs were overgrown with ZnSe and CdSe shells via the SILAR method, depositing up to two mono-layers of the shell material onto the dots. The resulting particles were analyzed using absorption and emission spectroscopy.

Figure 3.13 (left) displays the absorption spectra of InP:Yb^{3+} particles without shell (blue) and overcoated with one mono-layer (red) and two mono-layers (green) of a ZnSe shell. Upon shell-growth, a small blue-shift in the first absorption shoulder is observed. A possible explanation for this shift towards higher energies is the effective decrease in InP core size by either etching by the shell precursors or alloying with the shell material. The absorption shoulder becomes less well defined when more mono-layers of ZnSe are deposited, which may be the result of inhomogeneous shell deposition, resulting in particles with varying shell-thicknesses that confine the excitons to varying degrees.

In figure 3.14 the emission spectra collected from InP:Yb^{3+} samples without shell growth (blue) and deposited with one mono-layer ZnSe (red) and with two mono-layers (green). Emission spectra were obtained in both the visible region (left) and the IR region (right) upon excitation at 355 nm. The emission spectra in the visible region display an increase in band edge emission as well as trap state emission when a mono-layer of ZnSe is deposited and a further increase when the second mono-layer is grown. This may indicate the passivation of trap states at the QD surface by the type-I shell material. The passivation results in a decrease in the probability of non-radiative decay and an increase in QD emission. Trap state emission is still observed, indicating the existence of either surface traps that were not passivated or trap states related to crystal defects, originating from the dopants or the lattice mismatch between InP and ZnSe. The band edge emission of the QDs in the samples shift towards higher energies when more ZnSe is deposited. This can, in the same manner as the blue-shift in the first absorption shoulder, be explained by the effective decrease in InP core radius, either by etching or alloying. The IR region displays the Yb^{3+} emission at 975 nm upon QD excitation in every sample, as well as a broad band of trap state emission. When the ZnSe shell is grown, the intensity of the trap state emission increases with each additional layer, in the same way

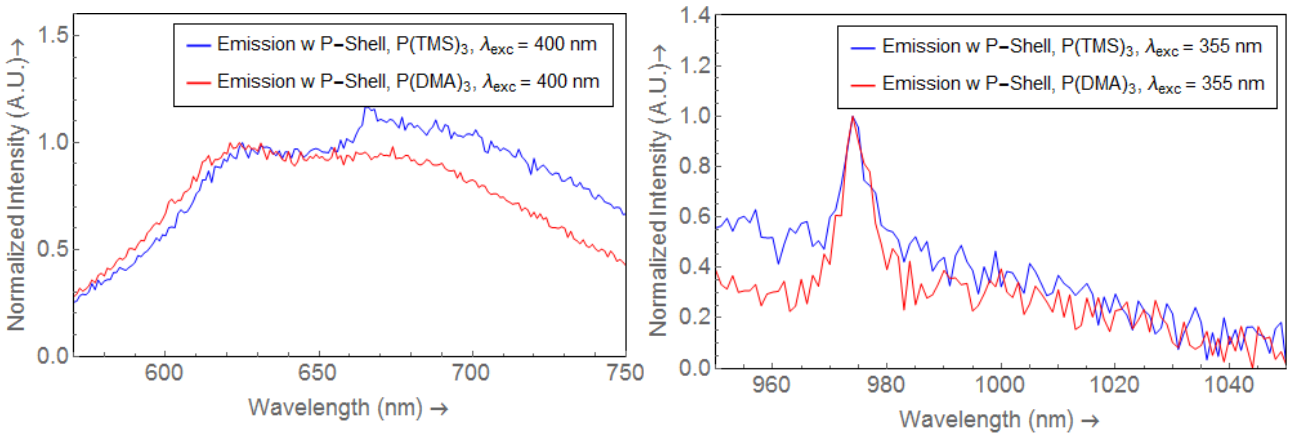

Figure 3.12: Emission spectra obtained from Yb^{3+} doped InP QDs encapsulated with P by reaction with $P(TMS)_3$ (blue) and $P(DMA)_3$ (red). Spectra in the visible region (left) obtained after excitation at 400 nm and in the IR (right) by excitation at 355 nm. Both spectra in the visible region display band edge emission as well as trap state emission. The visible emission of the blue spectrum is shifted slightly to the right as a result of the increased QD size due to the higher reactivity of $P(TMS)_3$. The IR region does not reveal a significantly increased Yb^{3+} emission peak upon P shell deposition. The spectrum obtained from the sample made with $P(TMS)_3$ displays a lower Yb^{3+} emission peak with respect to the trap state emission due to the red-shift of the trap state emission compared to the sample made with $P(DMA)_3$.

that was observed in the visible region. The dopant emission intensity appears to decrease, especially after the deposition of two mono-layers of shell material. This may be the result of the removal of the Yb^{3+} ions from the InP surface by the ZnSe shell material. The spectra do not provide evidence of the successful encapsulation of the dopant ions by ZnSe overgrowth as the Yb^{3+} peak stays at the same position.

The absorption spectra of the InP:Yb^{3+} samples that were coated with a CdSe shell are displayed in figure 3.13 (right). Shown are the absorption of InP:Yb^{3+} QDs with no shell grown (blue), with one mono-layer of CdSe grown (red) and with two mono-layers of CdSe grown (green). Comparing the spectra, a shift in the first absorption shoulder of the quantum dots towards lower energies can be seen upon deposition of a mono-layer of CdSe and a further shift upon the deposition of the second mono-layer. The shift is explained by the CdSe being a type $I^{1/2}$ shell, confining the hole generated by electron excitation, but not the electron. Adding additional layers of CdSe shell material to the dots then leads to a decrease in quantum confinement and a red-shift in the first absorption shoulder.

The spectra in figure 3.15 display the emission of InP:Yb^{3+} (blue) and of these dots overgrown with one mono-layer CdSe (red) and two mono-layers CdSe (green) upon excitation at 355 nm. Emission spectra are obtained in the visible region (left) and the IR (right). In the visible region, upon the deposition of each extra mono-layer of CdSe, band edge emission intensity appears to decrease. The same trend is observed the infrared spectrum for the Yb^{3+} emission. An explanation for this loss of optical properties may be the lattice mismatch between the InP and the CdSe shell material, creating trap states at the interface. Growing CdSe shells on doped InP quantum dots proves to be detrimental for the Yb^{3+} dopant emission.

3.3.11 In(Zn)P cores

The introduction of zinc during the hot injection synthesis of InP quantum dots has been reported to increase the optical properties of the resulting particles compared to InP QDs synthesized without zinc. The Yb^{3+} doping procedure that has been investigated thus far displayed broad bands of trap state emission, attributed to the radiative recombination of generated excitons at surface states created by dangling bonds. The existence of these trap states is assumed to have a quenching effect on both the quantum dot band edge emission as well as the Yb^{3+} dopant emission since they create competitive relaxation pathways. To see if the optical properties of the doped dots can be increased by passivating the trap states by the addition of zinc in the QD core synthesis, the previously optimized doping

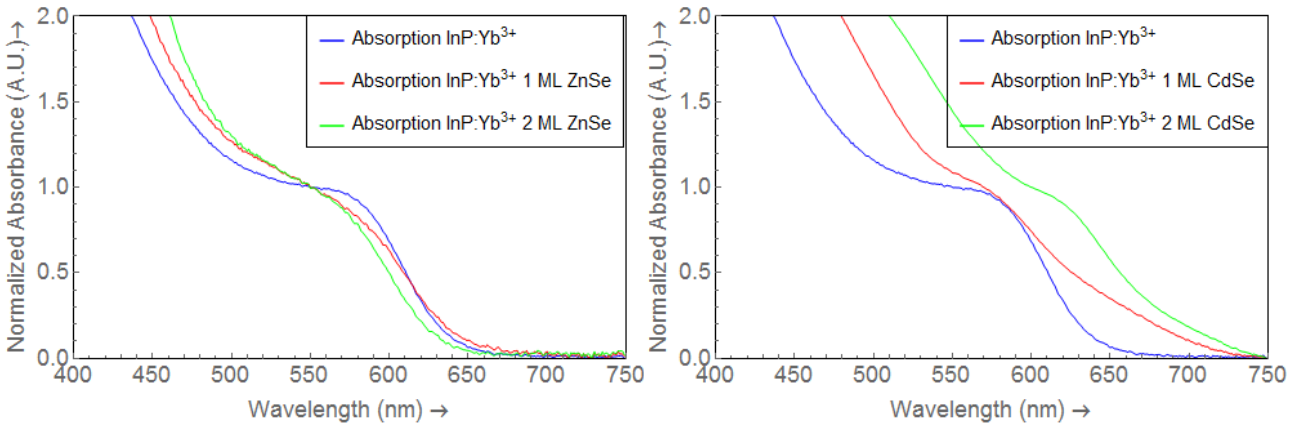

Figure 3.13: (Left) Absorption spectra obtained from InP:Yb^{3+} quantum dots (blue) overgrown with one monolayer ZnSe (red) and with two monolayers ZnSe (green). Upon overgrowth with ZnSe, a blue-shift in the absorption shoulder is observed. This is possibly due to etching of the QD by the Se. (Right) Absorption spectra obtained from InP:Yb^{3+} quantum dots (blue) overgrown with one monolayer CdSe (red) and with two monolayers CdSe (green). When CdSe is overgrown, a red-shift is observed in the QD absorption shoulder. This can be explained by the decreased confinement of the exciton due to the type $I^{1/2}$ character of the CdSe shell material.

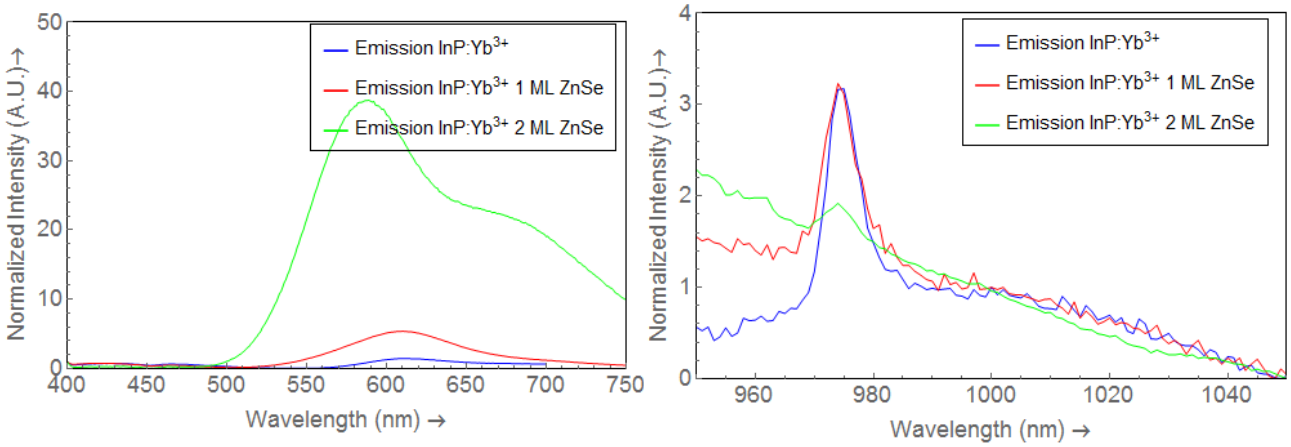

Figure 3.14: Emission spectra in the visible (left) and IR (right) region obtained upon excitation at 355 nm of InP:Yb^{3+} particles (blue) overgrown with one monolayer ZnSe (red) and with two monolayers ZnSe (green). The spectra in the visible region display an increase in band edge emission intensity with each applied monolayer of shell material, indication of the passivation of QD surface traps. The IR region displays a decrease in Yb^{3+} emission with each applied monolayer, indicating that the dopants are decoupled from the InP QD surface during the shell growth procedure.

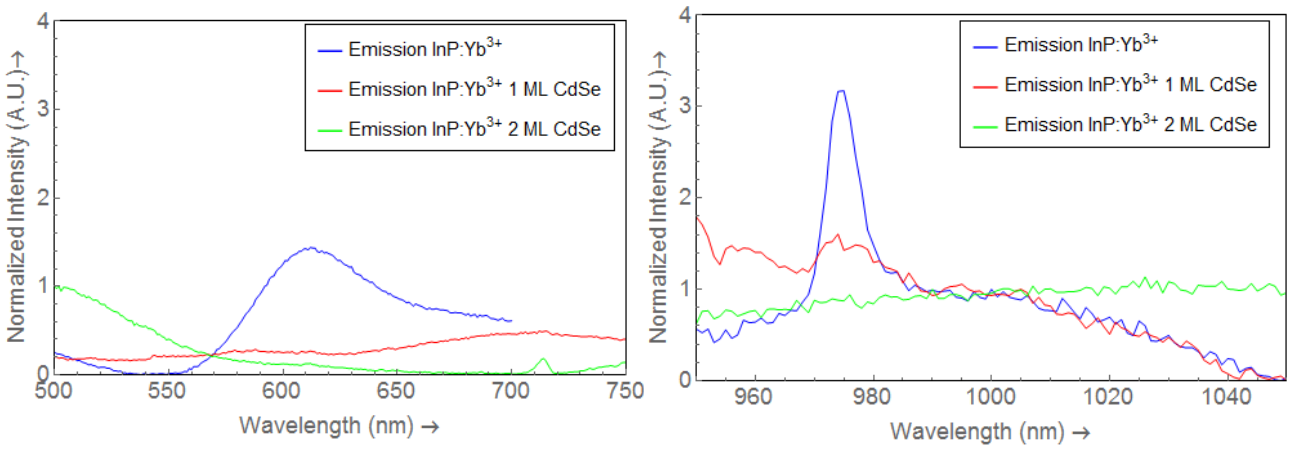

Figure 3.15: Emission spectra in the visible (left) and IR (right) region obtained upon excitation at 355 nm of InP:Yb^{3+} particles (blue) overgrown with one monolayer CdSe (red) and with two monolayers CdSe (green). The spectra in the visible region display a decrease in band edge emission intensity with each applied monolayer of shell material and the IR region displays a decrease in Yb^{3+} emission with each applied monolayer as well, suggesting that the deposition of CdSe onto the doped dots creates trap states that result in non-radiative emission after quantum dot excitation.

procedure is applied to In(Zn)P QD cores.

In(Zn)P QD cores are synthesized in the same manner as the InP QDs, the only change in the procedure is the presence of a 1:1 or 2:1 $ZnCl_2$:$InCl_3$ ratio in the mixture before the injection of the P precursor. The resulting particles were analyzed using absorption spectroscopy.

Figure 3.16 displays the absorption spectra of particles created with Zn:In ratios 0:1 (blue), 1:1 (red) and 2:1 (green). The addition of zinc in the QD core synthesis is demonstrated by the first absorption peak associated with the $S_h \rightarrow S_e$ transition being significantly more well-defined in the In(Zn)P absorption spectra, indicating a narrowing of the QD size distribution. Furthermore, a blue-shift in the absorption shoulder is observed when Zn is used, which may indicate smaller QD sizes. The blue-shift increases when more Zn is used in the synthesis. The observed effects can be explained by the presence of zinc at the InP QD surface during the synthesis, stabilizing the surface and reducing the size of the critical nuclei [36].

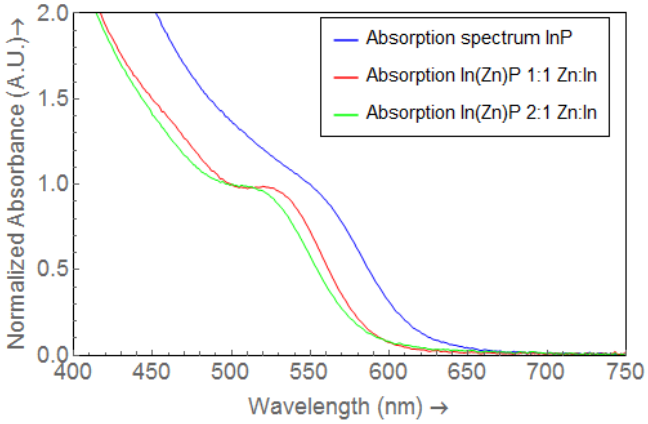

Figure 3.16: Absorption spectra obtained from In(Zn)P quantum dots synthesized with a 0:1 (blue), 1:1 (red) and 2:1 (green) Zn:In ratio. Presence of zinc during the QD synthesis results in a blue-shift and better definition of the $S_h \rightarrow S_e$ absorption shoulder. The blue-shift increases when more zinc is used. The effects are explained by the decrease of the quantum dot critical radius by stabilization of zinc at the surface during the synthesis.

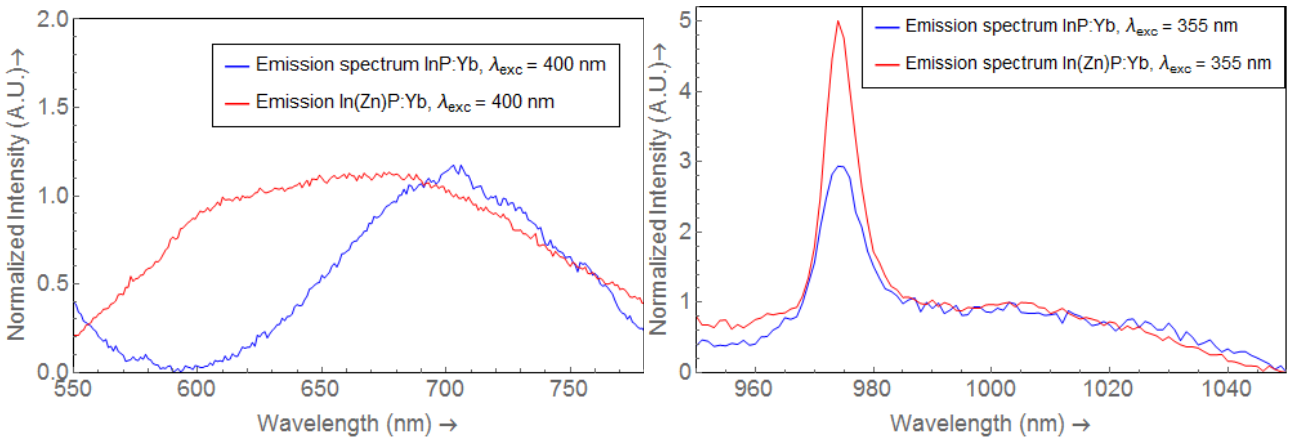

Figure 3.17: Emission spectra obtained from samples where the optimized doping procedure is applied to InP cores (blue) and In(Zn)P cores (red). Emission spectra were collected in the visible region (left) upon excitation at 400 nm and in the IR region (right) upon excitation at 355 nm. Both visible emission spectra display broad trap state emission peaks. The spectra obtained in the IR display Yb^{3+} emission upon QD excitation. In the In(Zn)P particles, the emission becomes more pronounced, a possible result of the passivation of trap states by Zn.

3.3.12 Growth doping In(Zn)P

The effect of using In(Zn)P QDs as cores for the doping experiments is investigated by applying the previously optimized growth doping procedure to In(Zn)P cores synthesized with a 1:1 Zn:In ratio. The resulting particles were not encapsulated with a shell. On the obtained samples, emission, absorption, and excitation spectroscopy is performed.

Figure 3.17 comparatively displays emission spectra obtained from samples where the optimized doping procedure is applied to InP cores (blue) and In(Zn)P cores (red). Emission spectra were collected in the visible region (left) upon excitation at 400 nm and in the IR region (right) upon excitation at 355 nm.

The visible region displays a very broad emission band in the doped In(Zn)P sample. This band is likely formed by the overlapping peaks of band edge emission at 600 nm and trap state emission around 670 nm. The rise of radiative band edge decay in the In(Zn)P QD sample compared to the InP sample may be an indication of the passivation of trap states by Zn residing at the InP surface.

Comparison of the IR emission reveals a strong amplification of the Yb^{3+} emission at 975 nm. This increase in intensity can also be attributed to the passivation of trap states by Zn: a decrease in relaxation pathways via trap states results in a higher probability of energy transfer to the dopant ions, leading to higher dopant emission intensity.

The origin of the large peak at 975 nm is further investigated using excitation spectroscopy. Figure 3.18 displays the excitation spectrum taken at 975 nm (red). The excitation spectrum is compared to the absorption of the same sample in same range (blue). Both spectra display the same absorption shoulder at 540 nm, suggesting that energy transfer after absorption of the QD dot is responsible for the Yb^{3+} emission. A difference that is observed in the spectra is the much lower intensity in the range 300 to 400 in the excitation spectrum compared to the absorption spectrum. This difference is explained by the absorption of QD ligands and other organic molecules. These absorb light in the near UV but do not transfer the energy to the lanthanide dopants, resulting in a discrepancy between the sample absorption spectrum and the Yb^{3+} excitation spectrum.

3.3.13 Rapid overgrowth of a ZnS-shell

To investigate whether the optical properties of the Yb^{3+} doped In(Zn)P quantum dots could be further improved by application of a type-I shell, experiments were conducted overgrowing In(Zn)P:Yb^{3+} particles with ZnS shells. Reaction conditions are chosen to minimize the previously observed effect of dopant lattice ejection by utilizing highly reactive Zn and S precursors in combination with the rela-

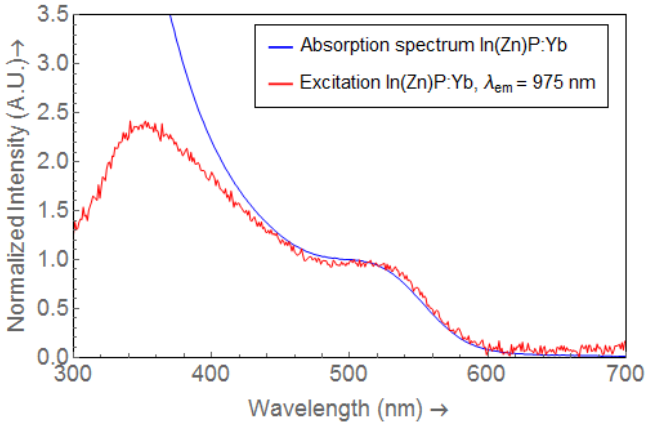

Figure 3.18: Absorption (blue) and excitation (red) spectra obtained from a In(Zn)P QDs (1:1 Zn:In ratio) doped with the optimized Yb^{3+} growth doping method. The excitation spectrum is recorded by measuring the emission intensity at 975 nm upon excitation over the 300 to 750 nm range. The overlapping spectra suggest energy transfer from the In(Zn)P QDs to the Yb^{3+} dopant ions upon QD absorption, resulting in dopant emission.

tively low reaction time of 20 minutes per shell. ZnS shells were grown via the SILAR method reacting $Zn(OA)_2$ with $S(TMS)_2$ at 210 °C. The resulting particles were studied with emission spectroscopy.

Figure 3.19 displays the emission spectra in the visible region (left) and the IR (right) of In(Zn)P:Yb^{3+} without a ZnS shell (blue), and overcoated with 1 ML ZnS (red), 2 ML ZnS (green), and 3 ML ZnS (black). All spectra where obtained by measuring emission after excitation at 355 nm.

Comparing the emission spectra in the visible region, an increase in the quantum dot band edge emission is observed in the samples where a monolayer of ZnS is grown. This increase in intensity is attributed to the passivation of InP surface trap states. When the second monolayer is deposited, a further increase in intensity is observed, indication further completion of the ZnS shell. Upon deposition of the third monolayer, the band edge emission drops in intensity, which may indicate that using this shell growth method, the precursor equivalent of two monolayers is optimal. All the spectra obtained in the visible region from the particles upon which shells were grown display a single emission peak, as opposed to the previously discussed visible emission spectra that displayed both a band edge emission peak as well as a trap state emission peak. This is further evidence of successful ZnS shell deposition.

In the IR region, the characteristic Yb^{3+} emission peak is observed at 975 nm. When the monolayers of ZnS shell material are deposited, the Yb^{3+} emission decreases in intensity with each successive monolayer. The explanation for this decrease in intensity is possibly the effect of lattice ejection, removing the dopant atoms from the quantum dot surface. This means that the shorter reaction time used in combination with a more highly reactive S precursor proved to be ineffective to successfully encapsulate the Yb^{3+} ions.

Conclusions

Several different shelling methods have been investigated in this research project to encapsulate Yb^{3+} ions resident on InP and In(Zn)P quantum dots, utilizing dierent materials and varying reaction conditions. The convincing evidence of encapsulation remains absent in the (time-resolved) emission spectra, as Yb^{3+} emission does not increase in intensity or shift towards a lower energy as previously reported [33]. An explanation for the unsuccessful overgrowth over the dopant ions in InP is the covalent nature of its crystal lattice that combined with the four-fold coördination of the cations does not allow for favorable incorporation of trivalent lanthanide ions that prefer a six-fold coördination.

3.3.14 Doping via Reiss method

Reiss and coworkers have reported the successful incorporation of Eu^{3+} ions into In(Zn)P/ZnS quantum dots [34]. The synthesis described in their publication involves a three-step, one-pot doping-

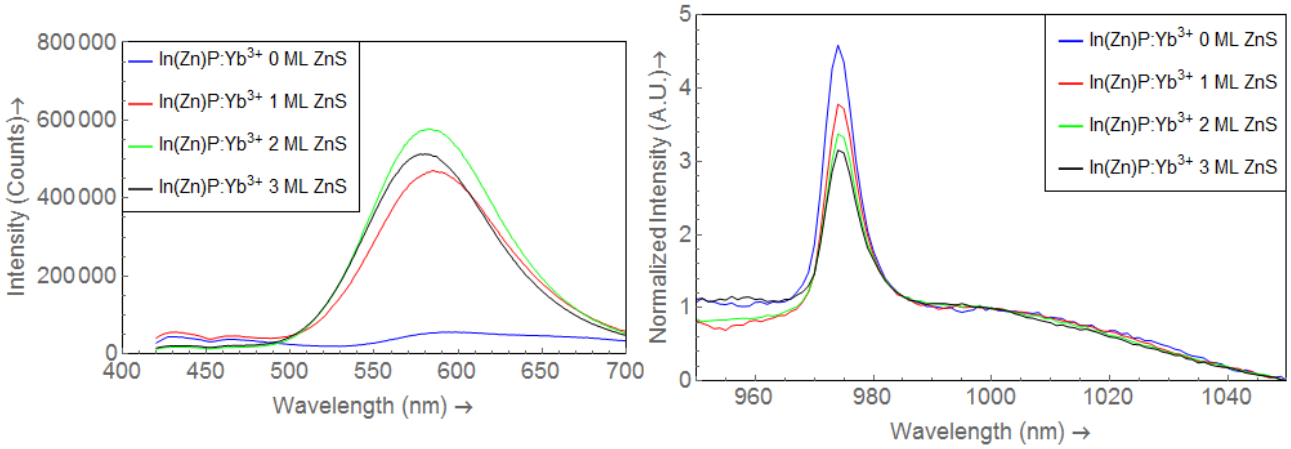

Figure 3.19: Obtained emission spectra in the visible region (left) and the IR (right) of In(Zn)P:Yb^{3+} without a ZnS shell (blue), and overcoated with 1 ML ZnS (red), 2 ML ZnS (green), and 3 ML ZnS (black) using a highly reactive S precursor at short reaction times. All spectra where obtained by measuring emission after excitation at 355 nm. Upon deposition of a ZnS-shell, the band edge emission of the quantum dots increases. The infrared region displays the Yb^{3+} emission peak at 975 nm, which decreases in intensity with each ZnS monolayer deposited.

strategy: As a first step, In(Zn)P are grown by heating up a solution of In, Zn, and P precursors with a In:Zn:P ratio of 1:2:0.5. Secondly a Eu-oleate precursor solution is added (in a 1:0.3 In:Eu ratio) in a slow dropwise manner. The third and final step is the overgrowth of a ZnS shell by slow addition of a mixture of $Zn(OA)_2$ and $S(TMS)_2$.

As an alternative to the growth doping strategy previously discussed in this section, the doping strategy described by the group of Reiss is adapted to utilize an Yb precursor instead of a Eu precursor in order to incorporate Yb^{3+} ions into In(Zn)P/ZnS quantum dots. Another change to the original synthesis is the use of a hot-injection approach to synthesize In(Zn)P QD cores, instead of the original method of heating up a mixture of precursors. The hot-injection method is chosen since it was deemed more feasible with the available lab-equipment. The three-step one-pot approach that was eventually used is described in section. The resulting particles were analyzed using absorption and emission spectroscopy.

The obtained absorption spectrum (blue) and emission spectra (red) in the visible region (left) and the IR region (right) are displayed in figure 3.20. Emission spectra were obtained after excitation at 355 nm.

The QD absorption shoulder is well defined and the band edge emission peak at 540 nm is relatively symmetrical, indications of high quality In(Zn)P/ZnS quantum dots with well passivated surface trap states due to successful ZnS shell growth. Upon QD excitation at 355 nm, emission in the IR region was measured, since Yb^{3+} emission of the $F_{5/2} \rightarrow {}^2F_{7/2}$ transition is expected around 1000 nm. The spectrum displays only noise, suggesting that no energy transfer from dot to dopant occurs and that no Yb^{3+} ions adhere to the In(Zn)P surface.

It is concluded that the doping method derived from the work of Reiss et al. proved unsuccessful to incorporate Yb^{3+} ions into In(Zn)P/ZnS quantum dots. Although Yb is expected to be chemically very similar to Eu, the reaction steps that led to Eu^{3+} emission upon QD excitation in the work of Reiss and coworkers did not lead to Yb^{3+} emission upon QD excitation when the synthesis was adapted to use Yb-oleate. A possible explanation for these different results is that the relatively low reaction temperatures used in the doping step (100 minutes at 80 °C and 20 minutes at 120 °C) where not high enough to couple Yb^{3+} to the quantum dot surface. Another explanation could be that using either Yb or Eu precursors, only a small portion is coupled to the QD surface. If the surface resident dopant ions are not successfully covered by the ZnS shell material, multi-phonon relaxation may take place in the excited Yb^{3+} ions by coupling to 3-4 solvent or ligand vibrations, leading to non-radiative decay. For excited Eu^{3+} ions, the energy difference is much higher, so their excited state will not be relaxed by coupling to multiple phonons, resulting in radiative decay.

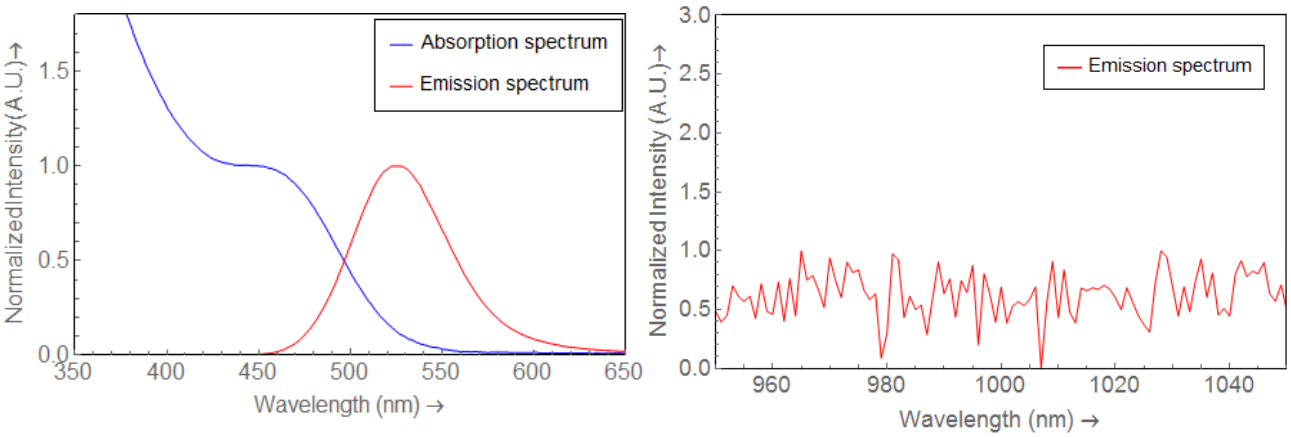

Figure 3.20: Absorption (blue) and emission (red) spectra obtained from In(Zn)P/ZnS particles made with an Yb^{3+} doping step based on a method described by Reiss et al. [34] to dope In(Zn)P/ZnS particles with Eu^{3+}. Emission is measured both in the visible region (left) and the IR region (right) upon excitation at 355 nm. The absorption spectrum displays a well defined QD absorption shoulder and the visible emission spectrum displays a symmetric band edge emission peak, indicating high quality In(Zn)P/ZnS QDs. No Yb^{3+} emission is observed in the IR region upon QD excitation, suggesting that the dopants are not successfully coupled to the dots.

3.4 Conclusion

In this chapter, the development of a growth doping strategy to synthesize InP quantum dots attached to Yb^{3+} ions was described. InP and In(Zn)P colloidal semiconductor nanocrystals were synthesized via a hot-injection method as cores to which the doping procedure would be applied. When no zinc was used in the quantum dot synthesis, the observed absorption shoulder was poorly defined, indicating a broad size distribution of the nanocrystals as a result of the low reactivity of the InP precursors. The presence of zinc stabilized the formed quantum dots, resulting in smaller nanocrystals with a more narrow size distribution. Visible of emission of the band edge transition was barely observed in the InP quantum dots, most likely due to the non-radiative decay via trap states.

The quantum dots were coupled to Yb^{3+} ions in a doping step, after which Yb^{3+} emission at 975 nm corresponding with the $^2F_{5/2} \rightarrow {}^2F_{7/2}$ transition could be observed upon quantum dot excitation in the visible region, indicating the possibility of energy transfer from InP quantum dots to Yb^{3+} lanthanide ions. The Yb^{3+} emission overlapped with a broad band of trap state emission. The highest Yb^{3+} emission was found when a Yb:QD ratio of 360:1 is used during the doping synthesis step.

The lifetime of the Yb^{3+} emission peak at 975 nm was measured to be very short. The short lifetime of the Yb^{3+} excited state is an indication that the dopant ions reside merely at the quantum dot surface, but washing the quantum dots multiple times did not decrease the Yb^{3+} emission, indicating that they are strongly bound to the nanocrystals.

To incorporate the dopant ions, several different shell materials were applied to the doped quantum dots: S shells, P shells, ZnSe shells, and CdSe shells were grown and ZnS shells were grown both via a slow and a fast synthesis route. While shell deposition upon the quantum dots was demonstrated to be successful based on the changes in the absorption and emission spectra in the visible region, the highest Yb^{3+} emission is measured in InP:Yb^{3+} quantum dots where no shell had been grown. An explanation for this trend may be the crystal self purification of the doped nanocrystals as a result of the high temperature reaction conditions.

An increase of Yb^{3+} emission upon quantum dot excitation was observed when In(Zn)P core particles were used, this increase is attributed to the passivation of trap states by zinc, leading to more efficient energy transfer to the Yb^{3+} dopant ions after quantum dot excitation.

As an alternative doping method, a one pot synthesis route to dope In(Zn)P/ZnS quantum dots with Yb^{3+} was utilized based on an adaption of a previous publication describing the incorporation of

Eu^{3+} into In(Zn)P/ZnS quantum dots, but this strategy yielded no Yb^{3+} emission upon quantum dot excitation. The discrepency in the results may be explained by the low reaction temperature used in this synthesis approach. Another explanation might be that in the publication, Eu^{3+} ions reside at the quantum dot surface as well, but their emission is not, unlike in Yb^{3+} ions, quenched by multi-phonon relaxation.

Chapter 4

Incorporation of Yb^{3+} into CdSe quantum dots

Abstract

A growth doping strategy is used to couple Yb^{3+} ions to CdSe quantum dots. CdSe quantum dot cores of various sizes are synthesized via a hot-injection method and used as cores in a Yb^{3+} doping procedure. Coupling to Yb^{3+} ions results in emission at 975 nm corresponding with the Yb^{3+} $^2F_{5/2}$ $\rightarrow$ $^2F_{7/2}$ transition upon quantum dot excitation. Overgrowth with Se resulted in the rise of a second peak at 985 nm. Both peaks could be traced back to quantum dot excitation. The peak at 975 nm has a very short lifetime and is attributed to Yb^{3+} ions at the quantum dot surface, the peak at 985 nm has a significantly higher lifetime and is attributed to Yb^{3+} ions incorporated in the CdSe crystal lattice. The coupling of Yb^{3+} to differently sized quantum dots shows the characteristic Yb^{3+} emission at the same wavelengths while the band edge absorption is varied.

4.1 Introduction

The work of Meijerink *et al.* on the incorporation of Yb^{3+} ions into CdSe quantum dots provided convincing evidence of the successful coupling of the lanthanide ions to the nanocrystal and subsequent overgrowth of a CdSe shell [33]. Spectroscopic data show the emission of the Yb^{3+} dopant after excitation of the CdSe host particle. The Yb^{3+} emission line becomes sharper and shifts to the red when a Se shell is grown and a longer lifetime is observed. Band edge emission of the CdSe nanocrystals is still observed, however, indicating that the particles are not homogeneously doped.

The reported observations led to the proposition of the model depicted in figure 4.1. The Gaussian indicates the probability of finding an exciton in the quantum dot as a function of the distance to its center. The area underneath the black part of the curve is the probability of the exciton interacting with a dopant ion, leading to Yb^{3+} emission. The area beneath the grey part of the curve represents the chance that the exciton collapses without finding a dopant ion. The model implies that when the dopant is localized closer to the center of the host particle, energy transfer of the dot to the ion is more likely to occur resulting in more efficient Yb^{3+} emission upon quantum dot excitation.

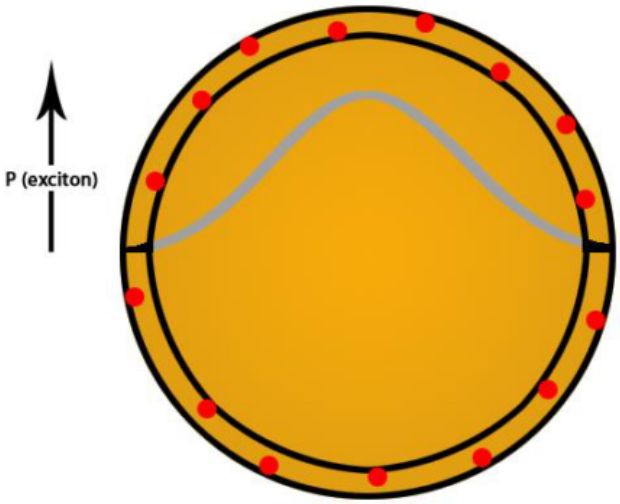

Figure 4.1: Visual representation of the proposed model. A quantum dot is depicted with dopant ions residing in an outer shell. The Gaussian indicates the probability of finding the exciton as a function of its location. Reproduced from the master thesis of Robin Geitenbeek.

In this chapter, the growth doping procedure described by Meijerink [33] will be applied to a series of differently sized CdSe quantum dots synthesized via a hot-injection procedure described by Peng et al. [64]. Doped particles will be overgrown with CdSe to create differently sized particles. Their optical properties will be analyzed using absorption, emission and time-resolved emission spectroscopy.

4.2 Experimental methods

4.2.1 Chemicals

Selenium (Se, 99.999 %) was purchased from Alfa Aesar. 1-Butanol (Bu OH, 99.8 %), cadmium acetate ($Cd(Ac)_2$, 99.99 %) methanol (MeOH, 99.9 %),1-octadecene (ODE, 90 %), oleic acid (OA, 90 %), oleylamine (OLAM, 70 %), toluene (99.8 %), tri-octylphosphine (TOP, 90 %), octadecylamine (ODA, 90 %) and ytterbium acetate ($Yb(Ac)_2$, 99.9 %) were purchased from Sigma-Aldrich. Reagents were used as received with the exception of ODA, ODE and OLAM, which were degassed under vacuum at 150 °C while stirring for 4 hours before use.

4.2.2 CdSe quantum dot synthesis

CdSe quantum dots were synthesized according to a hot injection protocol reported by Peng and coworkers [64]. Before the quantum dot synthesis, Cd and Se precursors were prepared. A 0.1 M $Cd(OA_2$ precursor solution was prepared by weighting 506 mg $Cd(Ac)_2$ in an Erlenmeyer flask, 21.9 mL ODE and 2.75 mL OA were added. The flask was put under vacuum using a Schlenk line and heated to 120 °C while stirring. After 2.5 hours, the mixture was cooled to room temperature. A 0.75 M TOP-Se precursor was prepared by weighting 1.42 g Se under inert conditions in a glove-box, adding 9.025 mL TOP and heating to 90 °C while stirring. After 15 minutes, the mixture was clear and colorless and 15.08 mL ODE was added. The hot injection CdSe quantum dot synthesis proceeded by introducing into a 3-neck round bottom flask 4.15 mL TOPO, 12 mL ODA and 18.75 mL of the TOP-Se precursor solution. The mixture was heated to 280 °C. Upon reaching this temperature, 18.75 mL of the $Cd(OA)_2$ solution is injected rapidly and the heating mantle is removed. Immediately after the injection step a 2 mL sample is extracted. After each subsequent time-interval of ca. 30 seconds, another sample is extracted. In total, 12 samples were extracted. The remaining reaction mixture cooled to room temperature, this is the 13^{th} sample. Each sample was washed by addition of a sample volume equivalent of toluene and two sample volume equivalents of both MeOH and BuOH. The samples were centrifuged and after decantation of the supernatant, they were redispersed in a 2 mL volume of toluene for the extracted samples and 40 mL of toluene for the final reaction mixture.

4.2.3 Yb^{3+} growth doping procedure

The CdSe quantum dot cores were doped via the growth doping procedure described by Meijerink *et al.* to incorporate ytterbium into CdSe nanoparticles [33].

Before the doping of the particles, an Yb precursor is synthesized and an Se precursor in either dispersion or solution is prepared. As an Yb precursor, Yb oleate is chosen and was prepared by weighting 0.42 g $Yb(Ac)_3{\cdot}(H_2O)_4$ (1.0 mmol) in an Erlenmeyer flask and adding 2 mL oleic acid and 8 mL ODE. The mixture was brought under vacuum using a Schlenk-line and heated to 80 °C while stirring. After 30 minutes, the temperature was raised to 150 °C and reaction was allowed for 4 hours before cooling. The result is a homogeneous viscous faintly yellow solution. 10 mL ODE was added to decrease the viscosity yielding a 0.05 M $Yb(OA)_3$ solution. The Se precursor was prepared by either adding 0.158 g of Se (2 mmol) to 20 mL ODE, resulting in a turbid black dispersion, or by dissolving the Se in ODE as described by Bullen et al [65], adding 0.158 g of Se (2 mmol) to 20 mL ODE and heating at 180 °C while stirring under vacuum using a Schlenk-line resulting in a clear faintly yellow solution of 0.1 M Se in ODE.

Reactional parameters in the doping procedure were varied as displayed in appendix D. In a typical synthesis, the growth doping of CdSe quantum dots proceeded by introducing into a vial, under inert conditions in a glove-box, 9 mL ODE, 3 mL OLAM and 140 nmol quantum dots in toluene. The mixture was then heated to 270 °C and kept at this temperature for at least 30 minutes to allow toluene to evaporate. The Yb precursor was then introduced by slow drop-wise addition of a mixture of 0.042 mL 0.05 M $Yb(OA)_3$ in ODE and 0.958 mL ODE (resulting in a 30:1 Yb:QD ratio). Reaction was then allowed for 30 minutes before addition of the Se precursor. A volume corresponding with a varied 1:1 to 1:30 ratio of Yb:Se of either 0.1 M Se in dispersion or 0.1 M Se in solution was added to a volume of ODE to create a 1 mL mixture of Se and ODE, and this mixture was injected in a

slow-drop-wise manner to the reaction mixture. Reaction with the Se as allowed for 30 minutes before cooling to room temperature. The resulting particles were then washed three times by addition of MeOH and BuOH, centrifugation and redispersion of the sedimentation in toluene.

4.2.4 CdSe deposition via SILAR

Doped CdSe quantum dots were grown to larger sizes by deposition of mono-layers of CdSe via the successive ionic layer adsorption and reaction (SILAR) method. The overgrowth of CdSe via SILAR proceeded as follows: under inert conditions in a glove-box, to a vial was added 1.8 mL ODE, 0.6 mL OLAM and a volume of Yb^{3+} doped CdSe quantum dots in toluene corresponding with 30 nmol quantum dots. The mixture was heated to 240 °C and toluene is allowed to evaporate for one hour. After evaporation of the toluene, a volume corresponding with the chemical amount needed to form a single mono-layer of CdSe, as calculated using the CdSe lattice parameters [61], of 0.1 M Se in ODE solution was added in a slow drop-wise manner. A few minutes after, the same volume of 0.1 M $Cd(OA)_3$ in solution is added in the same manner. Reaction was allowed for 30 minutes before a sample of 0.5 mL was extracted. This step is then repeated to form a second mono-layer: a volume corresponding with the chemical amount needed to form a the second mono-layer of CdSe, as calculated using the CdSe lattice parameters [61], of 0.1 M Se in ODE solution was added in a slow drop-wise manner. A few minutes after, the same volume of 0.1 M $Cd(OA)_3$ in solution is added in the same manner. Reaction was then again allowed for 30 minutes before a sample of 0.5 mL was taken. In total, this step is repeated four times, yielding a total of five samples where CdSe is deposited in one, two, three, four and five mono-layers.

4.2.5 Characterization

Absorption spectra were recorded with a Perkin Elmer Lambda 950 UV/VIS/NIR spectrophotometer. TEM was performed using a FEI Tecnai microscope operating at 120 kV. Emission and excitation spectra were recorded with an Edinburgh Instruments FLS 920 spectrofluorometer with a 450 W Xe lamp for excitation. Emission was detected using a Hamamatsu R928 photomultiplier tube for detection in the visible region and a nitrogen cooled R5509-72 photomultiplier tube for detection in the infrared region. Lifetimes were measured using the same detector as the emission after pulsed excitation using an Optical Parametric Oscillator (OPO) lasing system. Samples for spectroscopy were prepared by diluting a purified reaction mixture with toluene and were measured in quartz cuvettes.

4.3 Results and discussion

4.3.1 CdSe QD cores

CdSe quantum dots were synthesized according to a hot-injection protocol developed by the group of Peng [64], as described in section 4.2.4. Briefly, the synthesis was performed by heating up a mixture of TOPO, ODA and TOP-Se followed by quick injection of a $Cd(OA)_2$ solution. After injection, samples were extracted from the reaction mixture after intervals of circa 30 seconds. In total, 12 samples samples were extracted, the 13^{th} sample is the remaining reaction mixture.

Absorption spectra are obtained of the 13 collected samples, these are displayed in figure 4.2. Each sample that was extracted at a later time has its lowest energy absorption peak shifted further to the right. In every absorption spectrum, the expected characteristics of CdSe quantum dots are observed: an absorption peak at the lowest energy corresponding with the transition between the discrete S_h and S_e energy levels and depending on the sample, up to three more distinct exciton transitions can be observed. The small width of the absorption peaks indicates successful synthesis of relatively monodisperse CdSe QD samples. The shift towards lower energies in the lowest energy absorption peak of the samples is an indication that larger quantum dots are obtained due to a longer reaction time before sample extraction.

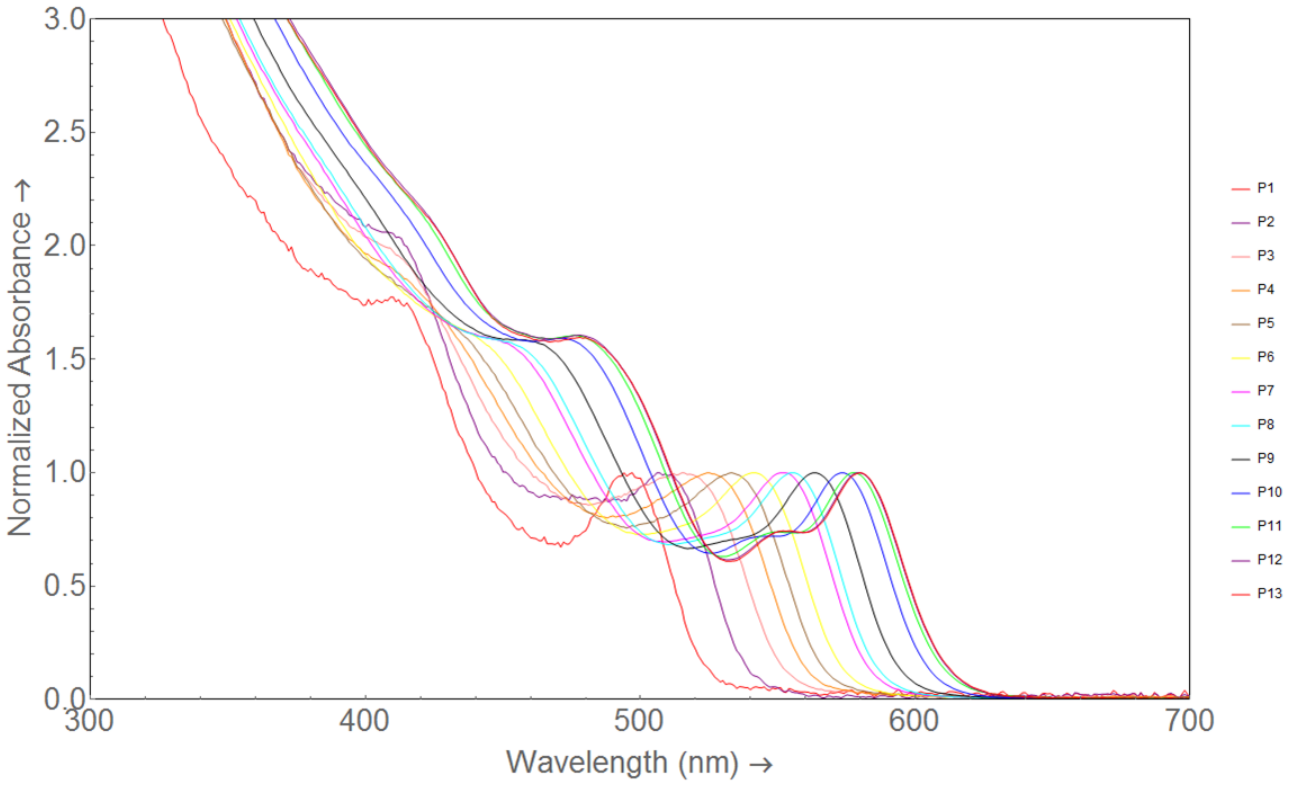

Figure 4.2: Absorption spectra of samples P1 to P13. Spectra are normalized to their first absorption peak. Samples extracted at a later time during the synthesis have their first absorption peak shifted further to the red, indicating larger particle sizes as a result of a longer reaction time.

From the height and position of the first absorption peak in the spectra, corresponding particle diameters and concentrations were calculated using an empirically derived fitting function [66]. Table 4.1 displays the QD diameter for each sample, as well as the sample volume, its concentration and the total amount of dots the reaction yielded.

On the sample with highest calculated particle diameter (P13), TEM images were taken as well. A representative TEM image is displayed in figure 4.3. The CdSe nanocrystals can easily be distinguished from the background, appearing as monodisperse near-spherical particles with similar diameters. Analyzing the TEM data, an average CdSe quantum dot diameter of 3.98 nm is found with a standard deviation of 0.5 nm. This larger size compared to the one calculated using the empirical fitting method (3.85 nm) may be explained by a bias in the manual measurement of the particles in TEM images. The

Table 4.1: Table dislaying the calculated particle sizes, volumes, and concentrations of the samples extracted at different times during the CdSe quantum dot hot injection synthesis.

Sample	Particle size (diameter, nm)	Volume (mL)	Concentration (mol/L)
P1	2.31	1.9	1.39343E-05
P2	2.43	1.9	1.47887E-05
P3	2.55	1.9	2.48964E-05
P4	2.64	1.9	3.00272E-05
P5	2.76	1.9	2.73293E-05
P6	2.89	1.9	4.5948E-05
P7	3.07	1.9	4.40181E-05
P8	3.14	1.9	5.45907E-05
P9	3.36	1.9	5.07194E-05
P10	3.65	1.9	4.40248E-05
P11	3.77	1.9	4.33372E-05
P12	3.83	1.9	4.26795E-05
P13	3.85	39.95	4.56625E-05

relatively low standard deviation in the particle diameters is further evidence of a low polydispersity in the QD sample, agreeing well with the observation of discrete peaks in the absorption spectrum.

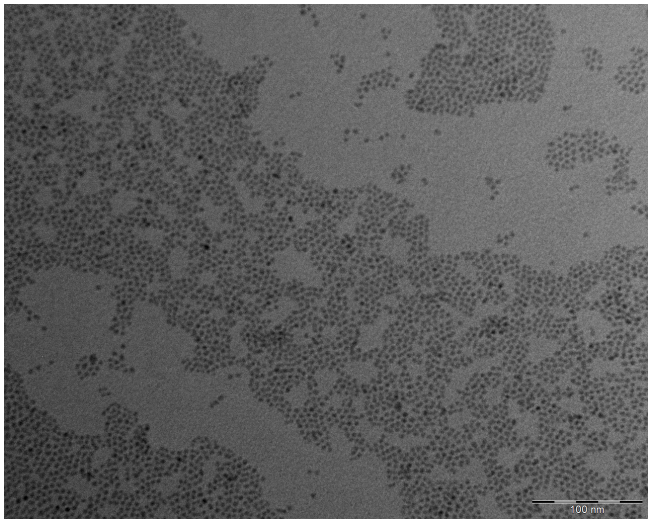

Figure 4.3: Representative TEM image of the P13 CdSe quantum dots. The quantum dots were measured to have an avarage diameter of 3.98 ± 0.5 nm.

4.3.2 Growth doping CdSe

To the largest batch of previously synthesized CdSe quantum dots, sample P13, the Yb^{3+} growth doping procedure optimized by Robin Geitenbeek and Rosa Martín-Rodríguez is applied. The synthesis is described in detail in section 4.2.3. The particles were doped with an amount of Yb in a 30:1 Yb:QD ratio. After the doping step, Se is deposited by addition of a dispersion of Se in ODE where the amount of Se is the same as the amount of Yb used.

The resulting particles were analyzed using emission spectroscopy, measuring emission in the 950 to 1050 nm IR region upon excitation of the the quantum dots at 585 nm. The emission spectrum in the IR is displayed in figure 4.4. The emission spectrum displays a small peak at 975 nm attributed to the emission of Yb^{3+} ions upon energy transfer from the quantum dots. A sloping line of what is probably trap state emission is observed as well. Comparing this spectrum to the results obtained in previous work, a high similarity to the IR emission of unshelled CdSe:Yb^{3+} QDs is observed [33], suggesting that the Yb^{3+} ions are not incorporated into the QDs, but merely reside at the QD surface.

This may also explain the low intensity of the emission peak, as the emission of surface resident Yb^{3+} ions may be quenched by non-radiative decay via multi-phonon relaxation.

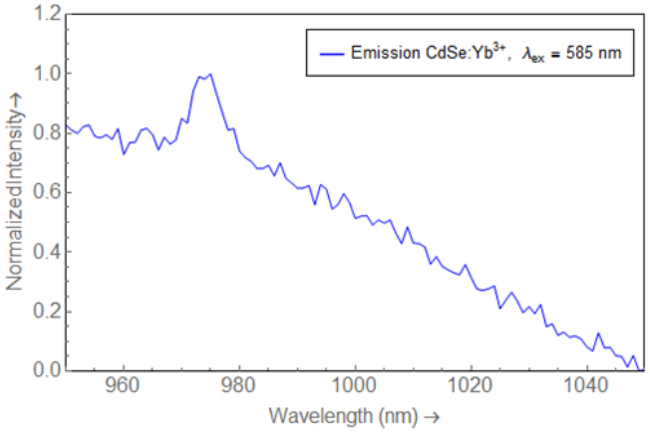

Figure 4.4: IR emission spectrum of 3.85 nm sized QDs doped with a 30:1 Yb:QD ratio and a 1:1 Yb:Se ratio. The spectrum is obtained after QD excitation at 585 nm. The peak observed at 975 nm is attributed to emission of surface-resident Yb^{3+} ions upon QD excitation. Spectra are vertically offset for clarity.

4.3.3 Optimizing the amount of Se used during encapsulation

Initial doping experiments with CdSe yielded evidence that the Se overgrowth step was not sufficient to incorporate the Yb^{3+} ions into the nanocrystal lattice, therefore a series of experiments using varying amounts and different types of Se-precursors is conducted to find the right experimental parameters for dopant incorporation.

The growth doping procedure is performed upon the 3.85 nm sized CdSe QDs in the same manner as discussed in the previous section, with the exception that the amount of Se used in the encapsulation step is varied. The effect of using Yb:Se ratios of 1:5, 1:10 and 1:20 is investigated. After the doping procedure, emission spectroscopy is performed.

Figure 4.5 displays emission spectra collected in the IR of samples encapsulated with an amount of Se used in a 1:5 (blue), 1:10 (red), and 1:20 (green) Yb:Se ratio. The spectra were obtained by excitation at 580 nm, 580 nm, and 586 nm respectively. The emission spectrum obtained from the sample where a 1:5 Yb:Se ratio is used looks very similar to the emission spectrum of the sample with a 1:1 Yb:Se ratio displayed in figure 4.4, displaying a low intensity peak at 975 nm, suggesting that the Yb^{3+} ions are not incorporated. When the amount of Se used is raised to a 1:10 Yb:Se ratio, the rise of a peak at 985 nm is observed. This peak may be attributed to emission of Yb^{3+} ions that are incorporated into the QD crystal lattice. The observed spectral shift of 10 nm with respect to the presumed to be surface-bound Yb^{3+} ions emitting at 975 nm is an indication of the change in chemical environment of the dopant ions. When the amount of Se used in the incorporation step is raised further to a 1:20 Yb:Se ratio, the emission peak at 985 nm becomes even more pronounced, an indication that even more surface-resident Yb^{3+} ions are incorporated into the CdSe QD crystal lattice by deposition of a higher amount of Se. Furthermore, a third peak is observed in the IR emission spectrum around 1030 nm. This peak may also be attributed to encapsulated Yb^{3+} ions emitting upon quantum dot excitation as the result of crystal field splitting due to the new crystal lattice environment of the dopant ions.

4.3.4 Encapsulation using a Se solution

As an alternative to a turbid dispersion of Se in ODE, a method optimized by the group of Bullen [65] is employed to dissolve Se in ODE at elevated temperatures. The homogeneous solution of Se is expected to provide better reproducibility of the encapsulating experiments, since the amount of Se transferred can be more accurately controlled then when using a sedimenting Se dispersion. Furthermore, Bullen et al. reported an increase of reactivity of the Se precursor when prepared in this manner over that of Se in dispersion [65].

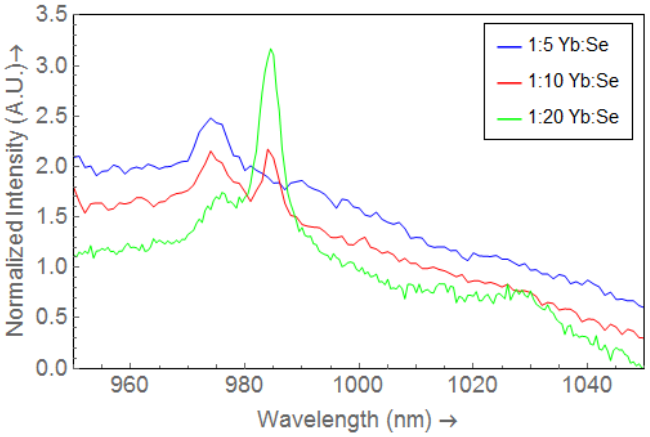

Figure 4.5: IR emission spectra of 3.85 nm sized QDs doped with a 30:1 Yb:QD ratio and a 1:5 (blue), 1:10 (red), and 1:20 (green) Yb:Se ratio using a Se precursor in dispersion. The spectra are obtained after QD excitation at 580 nm, 580 nm, and 586 nm, respectively. When higher amounts of Se are used, the rise of a Yb^{3+} emission peak at 985 nm is observed, attributed to Yb^{3+} ions that are incorporated into the CdSe nanocrystal lattice. Spectra are vertically offset for clarity.

The Se precursor dissolved in ODE is used in the encapsulation step of the growth doping experiments on CdSe, the amounts of Se used are varied, experiments were done with a 1:10, 1:20 and 1:30 Yb:Se ratio. The resulting particles were analyzed using emission spectroscopy.

In figure 4.6 emission spectra are displayed obtained in the IR region of samples encapsulated using a solution of Se in ODE in the Yb:Se ratios of 1:10 (blue), 1:20 (red), and 1:30 (green). Spectra were collected upon QD band edge excitation at 588 nm, 594 nm, and 597 nm, respectively. All the obtained emission spectra display both an emission peak at 975 nm and one at 985 nm, attributed to emission from Yb^{3+} ions bound to the QD surface and Yb^{3+} ions incorporated into the QD crystal lattice respectively. When the amount of Se added during the synthesis is increased, the peak at 985 nm increases in intensity as well and the rise of a peak at 1030 nm is observed as well, indicating that more surface-bound Yb^{3+} ions are encapsulated by the Se, in the same manner as observed in the experiments with the Se dispersion discussed in the previous section.

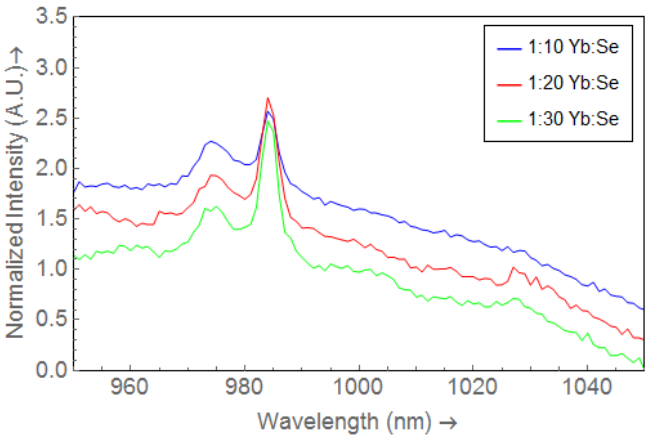

Figure 4.6: IR emission spectra of 3.85 nm sized QDs doped with a 30:1 Yb:QD ratio and a 1:10 (blue), 1:20 (red), and 1:30 (green) Yb:Se ratio using a Se precursor in solution. The spectra are obtained after QD excitation at 588 nm, 594 nm, and 597 nm, respectively. The intensity of the peak at Yb^{3+} emission peak at 985 nm increases with the amount of Se used, suggesting further incorporation of Yb ions into the CdSe nanocrystal lattice. Spectra are vertically offset for clarity.

4.3.5 Excitation spectroscopy

Doped dots that were encapsulated with higher amounts of Se displayed two peaks attributed to Yb^{3+} emission in the IR emission spectrum. To further investigate the origin of these peaks, excitation

spectra are recorded of the sample where a 1:30 Yb:Se ratio is used with a Se precursor dissolved in ODE. Emission intensities at 975 nm and 985 nm are measured upon excitation in the 500 to 650 nm range. The resulting spectra are displayed in figure 4.7. Here, the blue line is the excitation spectrum obtained upon measuring emission at 975 nm and the red line upon measuring emission at 985 nm. Both spectra display the excitonic feature of a quantum dot, indicating that energy transfer from the CdSe dots to the Yb^{3+} followed by radiative decay of the lanthanide ions is responsible for both emission peaks. The excitation spectrum obtained from the emission at 985 nm shows that the energy of the first quantum dot absorption peak is shifted slightly towards lower energies compared to the one displayed in the excitation spectrum obtained from emission at 975 nm. This may be the result of slightly larger quantum dots grown by deposition of a larger amount of Se, decreasing the exciton confinement. This observation agrees well with the postulation that Yb^{3+} ions emit at 985 nm after encapsulation with a Se shell.

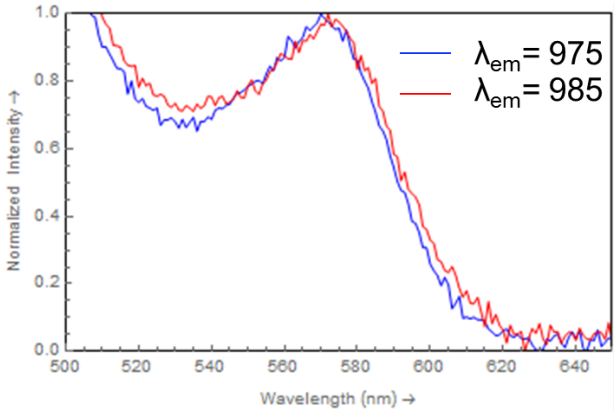

Figure 4.7: Excitation spectra obtained from the emission intensity at 975 nm (blue) and 985 nm (red). The quantum dot excitonic structure if found, suggesting energy transfer from CdSe quantum dots to Yb^{3+} dopant ions, resulting in Yb^{3+} emission.

4.3.6 Lifetime measurements

To further investigate the nature of the emission lines at 975 nm and 985 nm, lifetimes of the excited state are measured in the sample where the Se encapsulation step is performed using Se in solution in a 1:30 Yb:Se ratio. Decay curves are obtained by time-resolved emission measurement after excitation at 355 nm with a pulsed laser.

Figure 4.8 displays the decay curves collected measuring emission at 975 nm (blue dots) and at 985 nm (red dots). The curve obtained at emission at the 975 nm wavelength displays a rapid decay. This observation is attributed to the short-lived excited state of the Yb^{3+} dopant ions residing at the quantum dot surface. The decay is assisted by coupling to vibrations of ligand and solute molecules resulting in lower probability of radiative decay. The curve obtained measuring emission at 985 nm shows the presence of a distinctly longer lived component. This long-lifetime emission may be attributed to Yb^{3+} ions incorporated into the quantum dot crystal lattice. After incorporation, the ions are no longer in contact with ligand and solute molecules. This reduces the probability of non-radiative multi-phonon relaxation and the probability of radiative emission upon quantum dot energy transfer is strongly increased. The short component in the 985 nm decay curve can be attributed to trap state emission that is also measured at 985 nm upon quantum dot excitation. As displayed in figure 4.6, the emission lines attributed to Yb^{3+} emission overlap with a sloping baseline of what is assumed to be trap emission. The lifetime of quantum dot trap states is significantly lower than that of lanthanide emission, hence the distinction of the two lifetime components in the curve.

To quantify the measured lifetimes, exponential functions were fitted to the curves. The function fitted to the decay curve obtained from emission at 975 nm is plotted in figure 4.8 as a purple line and the function fitted to the decay curve obtained from emission at 985 is plotted as a black line. From the fit, the emission at 975 nm is calculated to correspond with a 2.8 μs excited state lifetime, a short emission lifetime attributed to multi-phonon relaxation. Since the decay curve obtained at 985

nm distinctly displays two components, a bi-exponential function is fitted. The calculated result is a 2.0 μs lifetime for the short lived excited state, which may be the lifetime of the trap state emission, and a second lifetime of 117 μs, which is attributed to Yb^{3+} emission from ions encapsulated by the Se shell.

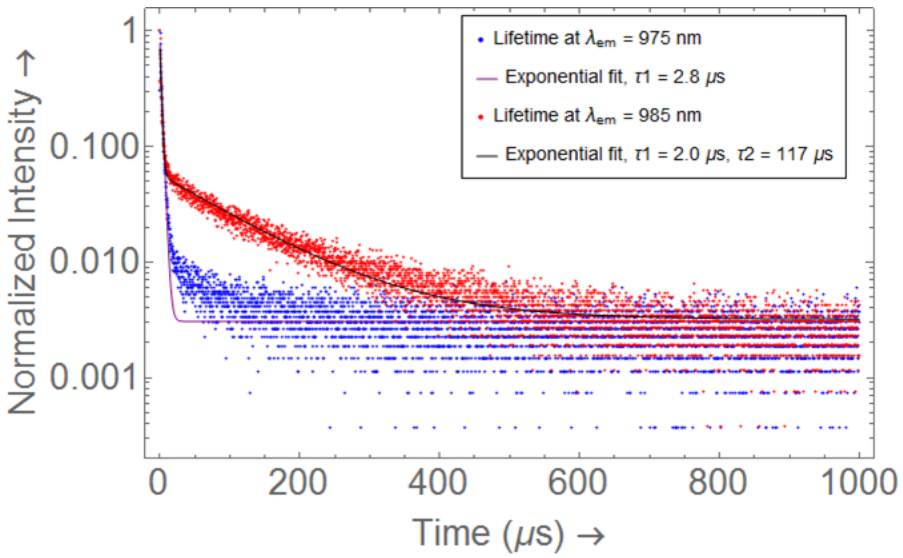

Figure 4.8: Decay curves obtained by time-resolved emission measurements at 975 nm (blue dots) and at 985 nm (red line), upon excitation at 355 nm. A mono-exponential function is fitted to the curve obtained at 975 nm (purple line) and a bi-exponential function to the curve obtained at 985 nm (black line). The 985 nm curve displays the rise of a long-lifetime component, attributed to Yb^{3+} ions encapsulated with Se.

4.3.7 Time resolved emission spectroscopy

The lifetime measurements showed that multiple components in the emission spectra decay at significantly different rates. To further visualize the emission at different time-scales, time resolved emission spectroscopy is performed.

Upon quantum dot band edge excitation at 597 nm of CdSe:Yb^{3+} quantum dots encapsulated with a Se precursor in solution in a 1:30 Yb:Se ratio, radiative decay curves are obtained by measuring time resolved emission from 950 nm to 1070 nm in steps of 4 nm, yielding a total of 31 decay curves. From these curves, emission spectra are constructed by integrating the photon counts at different time intervals.

Figure 4.9 displays two time resolved emission spectra between 950 nm and 1070 nm: a short lifetime spectrum constructed by integration of the 1 - 5 μs interval of the decay curves (left) and a long lifetime spectrum constructed by integration of the 5 - 1000 μs interval of the decay curves (right). The short lifetime spectrum displays a sloping band of emission between 950 nm and 1070 nm, which can be attributed to the short lived excited state decay of trap states generated by defects in the quantum dot. The peak at 975 nm displayed in the short lifetime spectrum is attributed to emission of surface-bound Yb^{3+} ions, having the emission of their lifetime reduced by multiphonon relaxation. The long lifetime spectrum on the right displays a high intensity peak at 985 nm. This peak is most likely caused by emission of Yb^{3+} incorporated into the quantum dot lattice, its long lifetime the result of shielding from solute and ligand vibrations. A second broader peak is observed in the long lifetime spectrum around 1030 nm. This peak can be a second emission peak of Yb^{3+} given rise to by crystal field splitting of the Yb^{3+} states. This provides further evidence of incorporation of the dopant ions into the CdSe crystal lattice.

4.3.8 Doping smaller particles

The growth doping procedure is applied to CdSe quantum dots with a smaller diameter to see whether the emission of the Yb^{3+} dopant ions would be influenced by the particle size. Quantum dots with a

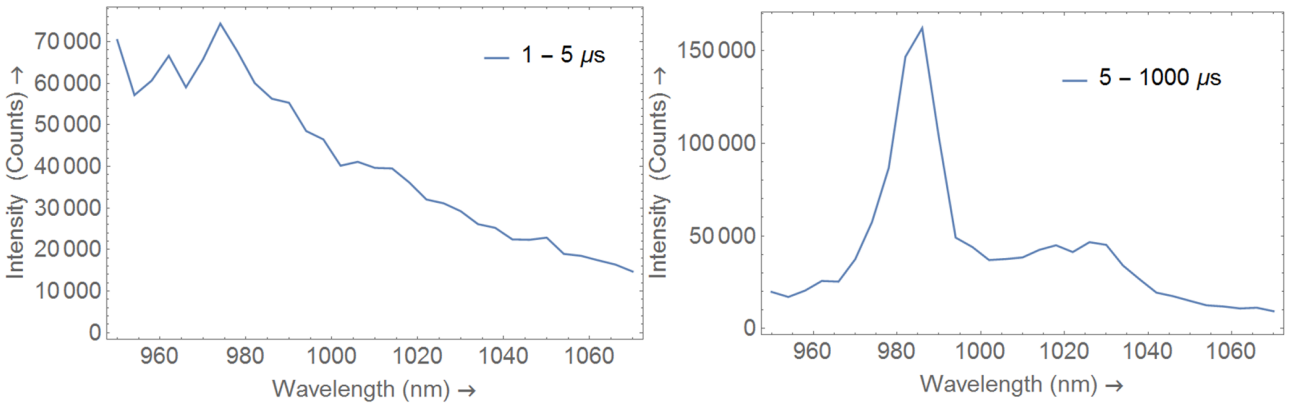

Figure 4.9: Time resolved emission spectra obtained from CdSe quantum dots doped with a 30:1 Yb:QD ratio and overgrown with Se in a 1:30 Yb:Se ratio. Decay curves are obtained after excitation at 597 nm measuring emission between 950 and 1070 nm between steps of 4 nm. Displayed are a short lifetime spectrum constructed by integration of the 1 - 5 μs interval of the decay curves (left) and a long lifetime spectrum constructed by integration of the 5 - 1000 μs interval of the decay curves (right). The short-lifetime emission spectrum displays a sloping band of trap state emission and the long-lifetime emission spectrum displays the crystal-field split Yb^{3+} emission of ions incorporated into the CdSe crystal lattice.

3.36 nm diameter (sample P9 in table 4.1) were doped with a 30:1 Yb:QD ratio and encapsulated with a dispersion of Se in a 1:10 Yb:Se ratio. After washing, the particles were analyzed using emission spectroscopy.

The emission of the smaller doped quantum dots upon QD band edge excitation of 578 nm is measured in the near IR region, see figure 4.10. As can be observed, the three characteristic peaks that were previously displayed in the emission spectra of larger doped particles are displayed here as well: one peak at 975 nm attributed to Yb^{3+} emission of ions resident at the quantum dot surface, and the peaks at 985 nm and 1030 nm attributed to Yb^{3+} emission of ions incorporated into the crystal lattice. While the excitonic properties of the CdSe QD core particles are changed, the emission peaks of the Yb^{3+} dopant after energy transfer from dot to dopant remain in the same place.

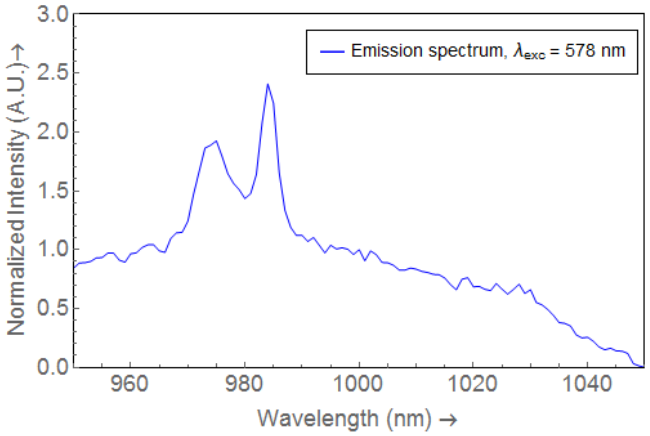

Figure 4.10: Emission spectrum obtained from 3.36 nm sized QDs doped with a 30:1 Yb:QD ratio and a 1:10 Yb:Se ratio. The spectrum is obtained after QD excitation at 578 nm.

4.3.9 SILAR

To further demonstrate the effect of differently sized host dopant ions on the observed Yb^{3+} dopant emission and to investigate whether energy transfer from the QDs to the dopant ions could be made more efficient by localizing the ions relatively closer to the QD core, multiple layers of CdSe are grown over doped particles via the SILAR method. Up to five mono-layers of CdSe are deposited on the

CdSe:Yb^{3+} quantum dots with a core size of 3.36 nm. The resulting samples were analyzed with absorption and emission spectroscopy.

In figure 4.11, absorption spectra are displayed obtained from bare CdSe cores (cyan), the cores doped with Yb^{3+} via the growth doping procedure (blue), doped dots overgrown with one (red), two (green), three (black), four (brown), and five (orange) mono-layers of CdSe. As can be seen, with each subsequent reaction step, the band edge absorption peak shifts further to the right. This indicates that during the growth doping step, larger particles are grown by deposition of Yb and Se onto the dots, decreasing the exciton confinement. After addition of the CdSe precursor equivalent of a single mono-layer, the first absorption peak shifts to the red, and this red-shift is increased with each following CdSe precursor addition step, suggesting that the particles are grown step by step by the addition of several mono-layers.

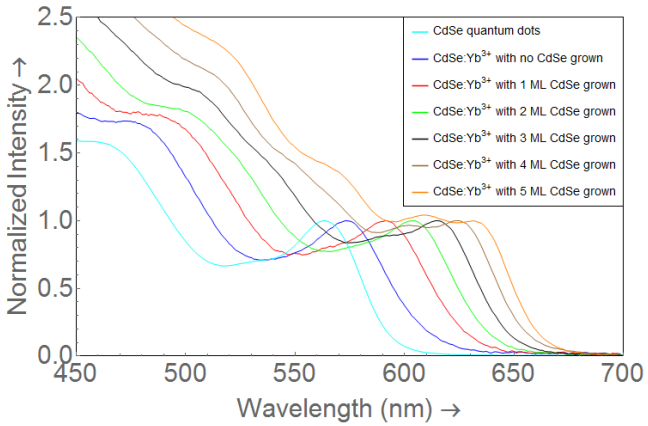

Figure 4.11: Absorption spectra obtained from bare CdSe quantum dots (cyan), CdSe quantum dots doped with Yb^{3+} via the growth doping procedure (blue), and the doped dots overgrown with one (red), two (green), three (black), four (brown), and five (orange) mono-layers of CdSe. With each mono-layer of CdSe deposited, the first absorption peak shifts towards lower energies.

Figure 4.12 shows emission spectra obtained in the visible region (left) and in the IR region (right). Emission spectra are obtained after excitation at 355 nm of samples of bare CdSe quantum dots (cyan), CdSe quantum dots doped with Yb^{3+} via the growth doping procedure (blue), and the doped dots overgrown with one (red), two (green), three (black), four (brown), and five (orange) mono-layers of CdSe. Here, each spectrum is normalized to its highest emission peak.

In the visible region, band edge emission of the quantum dots is observed. The average energy of the band edge emission peaks is shifted towards higher energies with each subsequent reaction step, similar to the energy shift observed in the absorption spectra. This is further proof that the quantum dots are grown to larger sizes during the doping procedure and after each addition of CdSe precursors to form a mono-layer. Another observation is the formation of small satellite peaks of energies higher than the primary band edge emission, becoming visible in the sample where three mono-layers are deposited (black) and becoming more pronounced with each subsequent mono-layer addition. This is most likely the result of secondary nucleation of CdSe quantum dots by reaction of the CdSe precursors to form nuclei instead of depositing on the doped quantum dot surface, resulting in smaller sized CdSe quantum dots in the sample. This may be caused by injecting the CdSe precursors too rapidly, resulting in a concentration that is sufficiently high for nucleation.

The emission of the samples is also measured in the IR region. All samples display a sloping band of trap state emission, and samples that were doped with Yb display the characteristic Yb^{3+} emission peaks at 975 nm and 985 nm. The trend observed in the IR spectra is that the emission peaks attributed to Yb^{3+} radiative decay become lower with respect to the trap state emission with each successive CdSe mono-layer deposition. An explanation for this observation is that the emission of trap states shifts towards lower energies with increasing quantum dot diameters. Furthermore, the deposition of CdSe may lead to an increase of crystal defects in the nanocrystal lattice by creating electron traps at the surface, increasing the number of trap states and the probability of radiative trap state decay. The Yb^{3+} emission peaks remain fixed at the 975 nm and 985 nm wavelengths, even

though the size of the host particles is increased via SILAR. This agrees well with the previous observation that the size of the quantum dots does not influence the emission properties of the lanthanide doped ions, and that their characteristic emission lines can be coupled to to the size-tunable broad absorption of CdSe quantum dots.

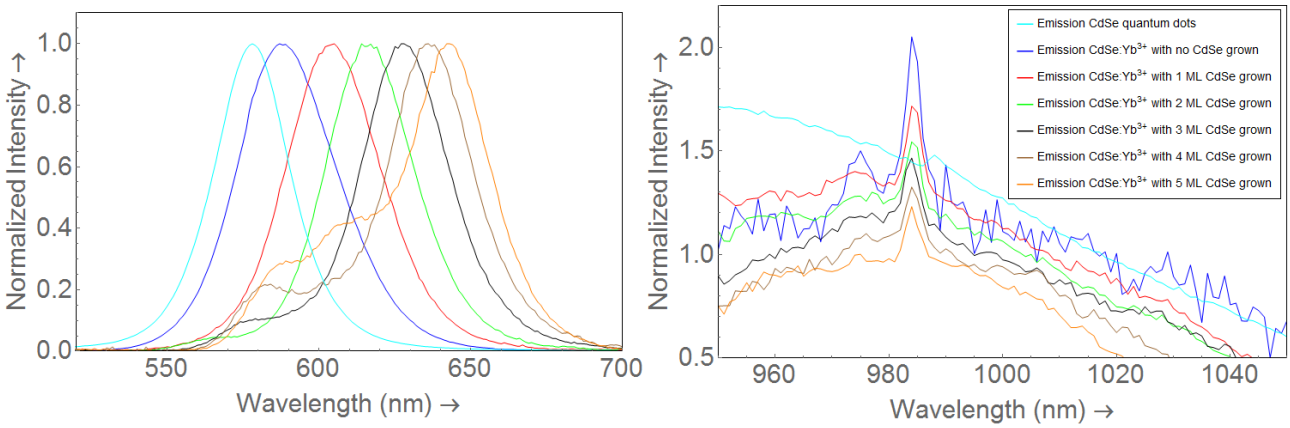

Figure 4.12: Emission spectra obtained in the visible region (left) and in the IR region (right), obtained after excitation at 355 nm of samples of bare CdSe quantum dots (cyan), CdSe quantum dots doped with Yb^{3+} via the growth doping procedure (blue), and the doped dots overgrown with one (red), two (green), three (black), four (brown), and five (orange) mono-layers of CdSe. Spectra are normalized to their highest emission peak. A shift towards lower energies is observed in the band edge emission of the quantum dots with each layer of CdSe deposited. In the IR, a relative decrease of Yb^{3+} emission intensity with respect to the trap state emission intensity is displayed with the addition of each subsequent mono-layer of CdSe. Spectra are vertically offset for clarity.

Of the Yb^{3+} emission in the SILAR sample series, the lifetimes are measured as well. Figure 4.13 displays the decay curves that were obtained measuring the emission at 985 nm upon excitation at 355 nm. All decay curves display the previously observed rapidly decaying component attributed to trap state emission, and a more slowly decaying component attributed to Yb^{3+} emission of ions that are incorporated into the quantum dot lattice. When CdSe is deposited onto the doped dots via SILAR, the relative intensity of the slowly decaying component decreases, corresponding with the observed decrease of the Yb^{3+} emission with respect to the trap state emission in the emission spectra. The lifetimes of the excited states are quantified by fitting bi-exponential functions to the curves. The calculated lifetimes are found to be around 1 μs for the fast decaying components and around 100 μs for the slow decaying components, with the exception of the curve obtained from the sample where one mono-layer of CdSe is grown (red), where the intensity of the slowly decaying component is too low for a successful fit. The highest lifetime is measured in the sample where 2 mono-layers of CdSe are deposited, displaying a lifetime of 136 μs of the slowly decaying Yb^{3+} excited state. The samples where 3 and 4 mono-layers of CdSe are deposited display longer lifetimes of the slowly decaying components with respect to the sample where no CdSe is deposited as well, 117 and 115 μs respectively. When the fifth layer of CdSe is deposited, the lifetime decreases further to 74 μs. Emission spectroscopy in the visible region suggested that particles of smaller sizes are present in the sample due to secondary nucleation, this may also affect the measured lifetimes.

Experimenting with the layer by layer deposition of CdSe onto CdSe:Yb^{3+} quantum dots revealed that the Yb^{3+} emission becomes less pronounced with respect to the trap state emission with each CdSe mono-layer deposited. The lifetime measurements show an increase in the Yb^{3+} excited state lifetime in samples where two, three, and four mono-layers of CdSe are deposited, suggesting more efficient energy transfer to the dopant, which may provide evidence to support the suggested model where the probability of energy transfer from dot to dopant is a function of the relative dopant distance to the host particle center. However, to further investigate this proposed model, particles with better optical properties need to be synthesized to eliminate the observed trap state emission.

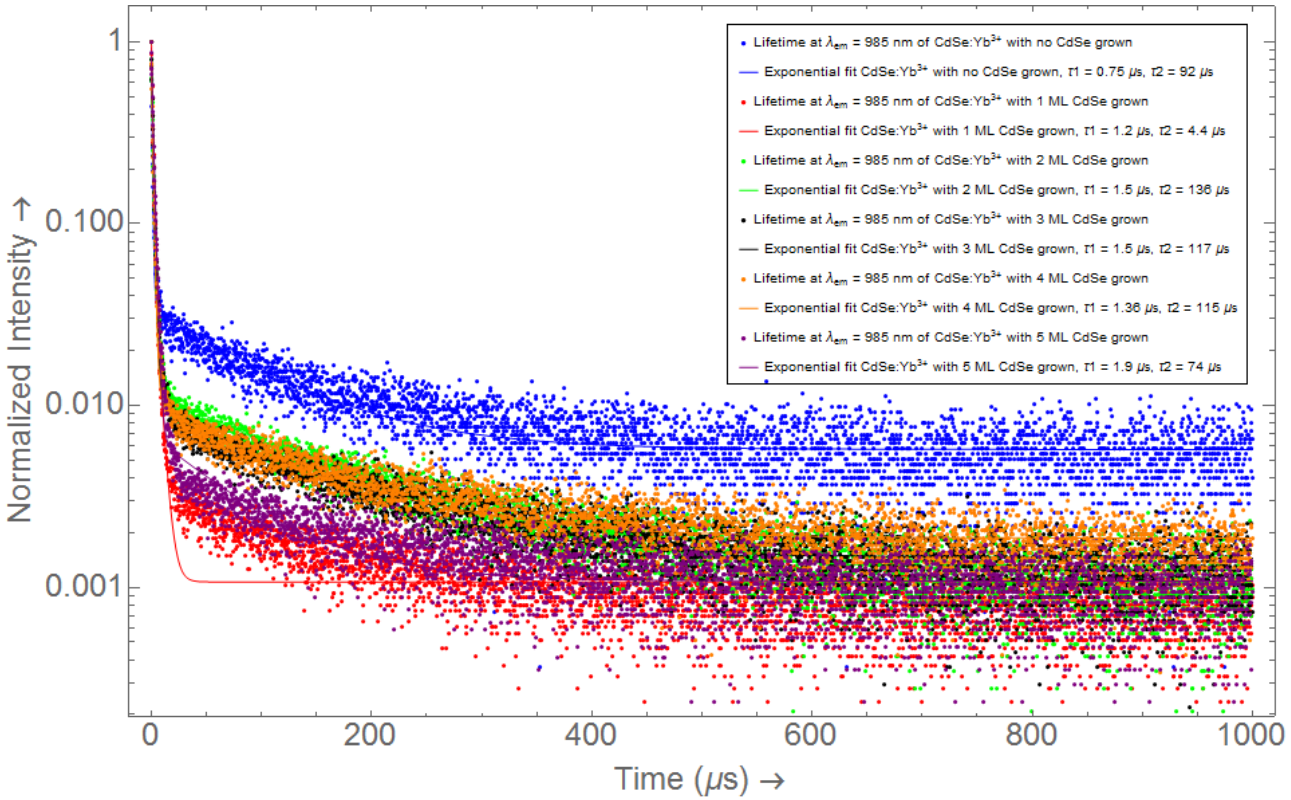

Figure 4.13: Decay curves obtained from Yb^{3+} doped CdSe quantum dots (blue dots), overgrown with 1 (red dots), 2 (green dots), 3 (black dots), 4 (orange dots), and 5 (purple dots) mono-layers of CdSe, measuring time-resolved emission intensity at 985 nm upon excitation at 355 nm. Bi-exponential functions are fitted to the curves displayed as lines with colors corresponding to the curves they are fitted to.

4.4 Conclusion

In this chapter, a growth doping strategy was used to couple Yb^{3+} ions to CdSe quantum dots. CdSe quantum dot cores of various sizes were synthesized via a hot-injection method. Extraction at later times after injection of the Cd precursor resulted in a red-shift of the first absorption peak, indicating an increase of CdSe quantum dot size.

Coupling to Yb^{3+} ions resulted in a single emission peak at 975 nm corresponding with the Yb^{3+} $^2F_{5/2} \rightarrow {}^2F_{7/2}$ transition upon quantum dot excitation when selenium was overgrown using a Yb:Se ratio of 1:1. Overgrowth with higher amounts of Se resulted in the rise of a second peak at 985 nm. Both peaks could be traced back to quantum dot excitation. The peak at 975 nm had a very short lifetime and is attributed to Yb^{3+} ions at the quantum dot surface, the peak at 985 nm had a significantly longer lifetime and is attributed to Yb^{3+} ions incorporated in the CdSe crystal lattice. Time-resolved emission spectra showed two peaks in the long lifetime spectrum in the IR: one at 985 nm and a second at 1030 nm. Both are attributed to the emission of Yb^{3+} incorporated into the CdSe quantum dots, the observation of two peaks is the result of crystal field splitting. From these results, is concluded that the incorporation of Yb^{3+} ions into CdSe quantum dots was successful.

The coupling of Yb^{3+} to smaller sized quantum dots shows the characteristic Yb^{3+} emission at the same wavelengths while the band edge absorption is varied. The independence of the lanthanide emission on the host particle size is further demonstrated when the SILAR method is employed to grow up to five mono-layers of CdSe onto the doped CdSe quantum dots. Experimenting with dots grown to different sizes via SILAR did not provide convincing evidence of more efficient energy transfer from the quantum dots to the dopant ions.

Chapter 5

Conclusions and outlook

5.1 Conclusions

This thesis described the successful coupling of Yb^{3+} to both InP and CdSe colloidal semiconductor nanocrystals via a growth doping procedure. Emission corresponding with the Yb^{3+} $^2F_{5/2} \rightarrow {}^2F_{7/2}$ transition is measured upon quantum dot excitation in both materials. After the doping of InP quantum dots with Yb^{3+} ions, lifetime measurements revealed that the Yb^{3+} ions reside merely at the quantum dot surface, having the lifetime of their excited state reduced by multi-phonon relaxation. Different shell materials were grown over Yb^{3+} doped InP quantum dots, but the dopant ions were not encapsulated. Overgrowth of Se on Yb^{3+} doped CdSe quantum dots revealed a second emission peak in the IR region with a significantly longer lifetime, attributed to Yb^{3+} emission of dopant ions that are incorporated into the CdSe crystal lattice. Yb^{3+} emission peaks were at the same wavelengths when differently sized doped dots were excited at varying wavelengths, demonstrating that the efficient absorption of the quantum dots can be varied by their size, resulting in the same characteristic emission of their lanthanide dopant ions. The deposition of CdSe mono-layers was performed to investigate a model describing the probability of energy transfer from dot to dopant as a function of the distance between the dopant ions and the host nanocrystal center. Results were inconclusive due to the large intensity of trap state emission in the same region as the Yb^{3+} emission.

5.2 Outlook

The results obtained during the research described in this thesis provide an outlook towards future experiments, both in the analysis and the synthesis regime. They will be described in this section.

Further quantitative analysis

The particles synthesized during this thesis were mainly analyzed using absorption and (time resolved) emission spectroscopy, providing a primarily qualitative description of the fabricated systems. Different analysis techniques need to be employed for a more quantitative description.

A spectroscopic analysis technique that can be performed is the quantitative measurement of the efficiency of radiative decay in Yb^{3+} doped quantum dots after excitation, both from the quantum dot band edge and from the Yb^{3+} excited state. Luminescent quantum yields can be calculated using an integrating sphere or a luminescent reference dye. The quantum yields of the doped nanocrystals can provide insight of the efficiency of the energy transfer from the excited state of the quantum dots to the Yb^{3+} dopant ions.

To quantify the amount of Yb^{3+} ions present in the doped quantum dots, both electron dispersive x-ray scattering (EDX) and inductively coupled plasma atomic emission spectroscopy (ICP-AES) can be employed. Using these techniques, elemental analysis can be performed to give a percentage of the present elements to show how much dopant ions are incorporated and how the ratio of the elements in the original quantum dot lattice is changed by the doping procedure. These results may provide insight in the doping mechanism of the growth doping procedure.

Changing the building blocks in the synthesis

The growth doping procedure to attach and incorporate lanthanide ions into quantum dots described in this thesis utilized three primary building blocks: the quantum dot core, the lanthanide dopant ions, and the material of the overgrown shell. Novel luminescent systems can be fabricated by changing any of these building blocks.

InP and CdSe were utilized as quantum dot core materials. The doping procedure may be applied to other materials as well. Zinc selenide (ZnSe) and copper indium sulfide (CIS) are materials with a low intrinsic toxicity compared to CdSe nanocrystals, while their quantum dots display efficient size-tunable absorption in the visible region as well. The cations in the ZnSe and CIS nanocrystal lattice are reported to experience a high lattice mobility, making them promising candidates for doping experiments.

Ytterbium was chosen as the dopant material in the experiments described in this thesis, due to the characteristic Yb^{3+} emission line being well separated from the quantum dot band edge emission. Different lanthanide ions may be incorporated as well, and a similar doping technique may be employed due to the chemical similarity of the ions in the lanthanide series. The possibility of energy transfer to different lanthanide ions then Yb^{3+} upon quantum dot excitation may then be demonstrated. Furthermore, using lanthanide ions with a sufficiently high gap between its ground state and its first excited state, multi-phonon relaxation may be prevented, resulting in more efficient lanthanide emission upon excitation of quantum dots where the lanthanide ions resides at the nanocrystal surface.

Different shell materials and growth methods to encapsulate Yb^{3+} dopant ions that are resident on the InP quantum dot surface may be employed. The seed-injection technique is a method that can be utilized for efficient shell growth: a mixture of previously doped quantum dots and one of the shell material precursors could be prepared, and injected into a heated up solution of the other shell material precursor, resulting in immediate shell deposition. The efficiency of the luminescence of Yb^{3+} ions incorporated into CdSe quantum dots may be increased by the overgrowth of a type-I (gradient) shell.

Investigation of the energy transfer probability model

In section 4.1, a model is proposed to describe the probability of energy transfer from dot to dopant as a function of the dopant distance to the host particle center. Initial experiments were performed in this thesis to investigate this model, but due to a high measured intensity of trap state emission, the efficiency of the energy transfer was difficult to quantify. The model may be more effectively investigated when an Yb^{3+} doped CdSe quantum dot sample that does not display trap state emission is grown to larger sizes via SILAR. An alternative method for the demonstration of the model would be the incorporation of Yb^{3+} ions into differently sized CdSe quantum dots subsequently grown to an equal size size by deposition of CdSe, resulting in similarly sized quantum dots with different dopant distances with respect to their host particle center. More efficient energy transfer could then be demonstrated when the dopant ions are closer to the quantum dot center.

Acknowledgements

The work described in this thesis was made possible with the help of a number of people whose effort i would like to acknowledge in this small chapter.

First of all, I would like to thank Elleke van Harten. You first introduced me to the project and were there as my daily supervisor ever since. Thank you for your enthusiasm, positivity, and helpfulness. You taught me a lot about quantum dot synthesis and were always there to advice me and answer my questions. I truly hope you will enjoy your final years at CMI!

During the final months of his PhD, Joren Eilers acted as my co-supervisor, bringing to the table his knowledge of doped quantum dot synthesis and spectroscopy. Thank you for the fruitful discussions and good luck working at Shell.

The void left in Joren's absence was almost immediately filled by Robin Geitenbeek, whose expertise with the incorporation of Yb^{3+} ions into CdSe quantum dots proved indispensable for the results obtained in this project. Thank you for your valuable input during our many discussions and good luck with your PhD project!

Supervising both my supervisors and myself there was Andries Meijerink. Thank you for giving me the opportunity to do my project with your group and for the tremendous amount of spectroscopic and scientific knowledge you shared.

Freddy Rabouw deserves special mention for helping me with my measurements and for teaching me the finer art of data analysis using Mathematica.

Finally, I would like to thank all the other students at CMI. You created a great atmosphere and it's been a pleasure working with all of you!

Bibliography

[1] Celso de Mello Donegá. *Nanoparticles: Workhorses of Nanoscience*. 2014.

[2] Dan Li, Marc B Müller, Scott Gilje, Richard B Kaner, and Gordon G Wallace. Processable aqueous dispersions of graphene nanosheets. *Nature nanotechnology*, 3(2):101–105, 2008.

[3] Cécile Bouet, Benoit Mahler, Brice Nadal, Benjamin Abecassis, Mickael D. Tessier, Sandrine Ithurria, Xiangzhen Xu, and Benoit Dubertret. Two-dimensional growth of CdSe nanocrystals, from nanoplatelets to nanosheets. *Chemistry of Materials*, 25(4):639–645, 2013.

[4] C. J. Murphy and N. R. Jana. Controlling the aspect ratio of inorganic nanorods and nanowires. *Advanced Materials*, 14(1):80–82, 2002.

[5] Lionel Vayssieres. Growth of arrayed nanorods and nanowires of ZnO from aqueous solutions. *Advanced Materials*, 15(5):464–466, 2003.

[6] A. P. Alivisatos. Semiconductor Clusters, Nanocrystals and Quantum dots. *Science*, 271(5251):933–937, 1996.

[7] Clemens Burda, Xiaobo Chen, Radha Narayanan, and Mostafa a. El-Sayed. *Chemistry and properties of nanocrystals of different shapes*, volume 105. 2005.

[8] Mostafa a. El-Sayed. Small Is Different: Shape-,Size-, and Composition-Dependent Properties of Some Colloidal Semiconductor Nanocrystals. *Acc. Chem. Res*, 37(5):326, 2004.

[9] Emil Roduner. Size matters: why nanomaterials are different. *Chemical Society reviews*, 35(7):583–592, 2006.

[10] L.E. Brus. On the development of bulk optical properties in small semiconductor crystallites. *Journal of Luminescence*, 31-32(0):381–384, 1984.

[11] L E Brus. Electron-electron and electron-hole interactions in small semiconductor crystallites: The size dependence of the lowest excited electronic state. *The Journal of Chemical Physics*, 80(1984):4403, 1984.

[12] J. M. Caruge, J. E. Halpert, V. Wood, V. Bulović, and M. G. Bawendi. Colloidal quantum-dot light-emitting diodes with metal-oxide charge transport layers. *Nature Photonics*, 2(4):247–250, 2008.

[13] Moungi Bawendi & Vladimir Bulovic Seth Coe, Wing-Keung Woo. Electroluminescence from single monolayers of nanocrystals in molecular organic devices. *Nature*, 420(December):3–6, 2002.

[14] Qingjiang Sun, Y. Andrew Wang, Lin Song Li, Daoyuan Wang, Ting Zhu, Jian Xu, Chunhe Yang, and Yongfang Li. Bright, multicoloured light-emitting diodes based on quantum dots. *Nature Photonics*, 1(12):717–722, 2007.

[15] S Nizamoglu, T Ozel, E Sari, and H V Demir. White light generation using cdse/zns coreshell nanocrystals hybridized with ingan/gan light emitting diodes. *Nanotechnology*, 18(6):065709, 2007.

[16] Wendy U Huynh, Wendy U Huynh, Janke J Dittmer, and A Paul Alivisatos. Hybrid Nanorod-Polymer Solar Cells. *Science*, 295:2425–2428, 2002.

[17] A.J. Nozik. Quantum dot solar cells. *Physica E: Low-dimensional Systems and Nanostructures*, 14(1-2):115–120, 2002.

[18] Steven A. McDonald, Gerasimos Konstantatos, Shiguo Zhang, Paul W. Cyr, Ethan J. D. Klem, Larissa Levina, and Edward H. Sargent. Solution-processed PbS quantum dot infrared photodetectors and photovoltaics. *Nature Materials*, 4(2):138–142, 2005.

[19] P V Kamat. Quantum Dot Solar Cells. Semiconductor Nanocrystals as Light Harvesters. *Journal of Physical Chemistry C*, 112(48):18737–18753, 2008.

[20] Edward H Sargent. Colloidal Quantum Dot Solar Cells. *Nature Photonics*, 6(3):133–135, 2012.

[21] Paul Alivisatos. The use of nanocrystals in biological detection. *Nature Biotechnology*, 22(1):47–52, 2004.

[22] Igor L Medintz, H Tetsuo Uyeda, Ellen R Goldman, and Hedi Mattoussi. Quantum dot bioconjugates for imaging, labelling and sensing. *Nature materials*, 4:435–446, 2005.

[23] M Dahan, T Laurence, F Pinaud, D S Chemla, a P Alivisatos, M Sauer, and S Weiss. Time-gated biological imaging by use of colloidal quantum dots. *Optics letters*, 26(11):825–827, 2001.

[24] Pinaud F. F. Michalet, X., L. A. Bentolila, J. M. Tsay, S. Doose, J. J. Li, G. Sundaresan, A. M. Wu, S. S. Gambhir, and S. Weiss. Quantum Dots for Live Cells, in Vivo Imaging, and Diagnostics. *Science*, 307:538–545, 2005.

[25] Peng Wu and Xiu-Ping Yan. Doped quantum dots for chemo/biosensing and bioimaging. *Chemical Society reviews*, 42(12):5489–521, jun 2013.

[26] R. N. Bhargava, D. Gallagher, X. Hong, and A. Nurmikko. Optical Properties of Manganese-Doped of ZnS. *Physical Review Letters*, 72(3):1–4, 1994.

[27] Steven C Erwin, Lijun Zu, Michael I Haftel, Alexander L Efros, Thomas a Kennedy, and David J Norris. Doping semiconductor nanocrystals. *Nature*, 436(7047):91–94, 2005.

[28] Narayan Pradhan and Xiaogang Peng. Efficient and color-tunable Mn-doped ZnSe nanocrystal emitters: control of optical performance via greener synthetic chemistry. *Journal of the American Chemical Society*, 129(11):3339–3347, 2007.

[29] Renguo Xie and Xiaogang Peng. Synthesis of Cu-doped InP nanocrystals (d-dots) with ZnSe diffusion barrier as efficient and color-tunable NIR emitters. *Journal of the American Chemical Society*, 131(30):10645–51, aug 2009.

[30] B. Srivastava, Santanu Jana, and P Narayan. Doping Cu in Semiconductor Nanocrystals: Some Old and Some New Physical Insights. *Journal of the American Chemical Society*, (133):1007–1015, 2010.

[31] S. J. Xu, S. J. Chua, B. Liu, L. M. Gan, C. H. Chew, and G. Q. Xu. Luminescence characteristics of impurities-activated ZnS nanocrystals prepared in microemulsion with hydrothermal treatment. *Applied Physics Letters*, 73(4):478–480, 1998.

[32] Hua Yang, Lianxiang Yu, Lianchun Shen, and Li Wang. Preparation and luminescent properties of Eu^{3+}-doped zinc sulfide nanocrystals. *Materials Letters*, 58:1172–1175, 2004.

[33] Rosa Martín-Rodríguez, Robin Geitenbeek, and Andries Meijerink. Incorporation and luminescence of Yb3+ in CdSe nanocrystals. *Journal of the American Chemical Society*, 135(37):13668–71, sep 2013.

[34] Ung Thi Dieu Thuy, Axel Maurice, Nguyen Quang Liem, and Peter Reiss. Europium doped In(Zn)P/ZnS colloidal quantum dots. *Dalton transactions*, 42(35):12606–10, sep 2013.

[35] Paul Mushonga, Martin O. Onani, Abram M. Madiehe, and Mervin Meyer. Indium Phosphide-Based Semiconductor Nanocrystals and Their Applications. *Journal of Nanomaterials*, 2012:1–11, 2012.

[36] Woo-Seuk Song, Hye-Seung Lee, Ju Chul Lee, Dong Seon Jang, Yoonyoung Choi, Moongoo Choi, and Heesun Yang. Amine-derived synthetic approach to color-tunable InP/ZnS quantum dots with high fluorescent qualities. *Journal of Nanoparticle Research*, 15(6):1750, jun 2013.

[37] Liang Li and Peter Reiss. One-pot Synthesis of Highly Luminescent InP / ZnS Nanocrystals without Precursor Injection. *Journal of the American Chemical Society*, 130:11588–11589, 2008.

[38] Ung Thi Dieu Thuy, Peter Reiss, and Nguyen Quang Liem. Luminescence properties of In(Zn)P alloy core/ZnS shell quantum dots. *Applied Physics Letters*, 97(19):193104, 2010.

[39] Eun-Pyo Jang and Heesun Yang. Utilization of Solvothermally Grown InP/ZnS Quantum Dots as Wavelength Converters for Fabrication of White Light-Emitting Diodes. *Journal of Nanoscience and Nanotechnology*, 13(9):6011–6015, sep 2013.

[40] Celso de Mello Donegá. Synthesis and properties of colloidal heteronanocrystals. *Chem. Soc. Rev.*, 40(3):1512–1546, 2011.

[41] S.V. Gaponenko. *Introduction to Nanophotonics*. 2010.

[42] A A Guzelian, J E B Katari, A V Kadavanich, U Banin, K Hamad, E Juban, A P Alivisatos, R H Wolters, C C Arnold, and J R Heath. Synthesis of Size-Selected, Surface-Passivated InP Nanocrystals. *Journal of Physical Chemistry*, 100(17):7212–7219, 1996.

[43] R W Meulenberg, J R I Lee, a Wolcott, J Z Zhang, L J Terminello, and T van Buuren. Determination of the Excition Binding Energy in CdSe Quantum Dots. *Acs Nano*, 3(2):325–330, 2009.

[44] Moungi G. Bawendi, Michael L. Steigerwald, and Louis E. Brus. The Quantum Mechanics Of Larger Semiconductor Clus ters (. *Annual Review of Physical Chemistry*, 41(4):477–496, 1990.

[45] Donald A. McQuarrie and John D. Simon. *Physical Chemistry: A Molecular Approach*. University Science Books, 1997.

[46] E. Groeneveld. Synthesis and optical spectroscopy of (hetero)-nanocrystals. ph.d. thesis, 2012.

[47] Peter Reiss, Myriam Protière, and Liang Li. Core/Shell semiconductor nanocrystals. *Small (Weinheim an der Bergstrasse, Germany)*, 5(2):154–68, feb 2009.

[48] Mark A. Reed. Quantum Dots. *Scientific American*, 268(1):118–123, 1993.

[49] Celso deMelloDonegá, Peter Liljeroth, and Daniel Vanmaekelbergh. Physicochemical Evaluation of the Hot-Injection Method, a Synthesis Route for Monodisperse Nanocrystals. *Small*, 1(12):1152–1162, 2005.

[50] Jongnam Park, Jin Joo, Gu Kwon Soon, Youngjin Jang, and Taeghwan Hyeon. Synthesis of monodisperse spherical nanocrystals. *Angewandte Chemie - International Edition*, 46(25):4630–4660, 2007.

[51] Celso de Mello Donegá. *Nanoparticles: Workhorses of Nanoscience*. 2014.

[52] David J Norris, Alexander L Efros, and Steven C Erwin. Doped nanocrystals. *Science (New York, N.Y.)*, 319(5871):1776–9, mar 2008.

[53] Raffaella Buonsanti and Delia J. Milliron. Chemistry of Doped Colloidal Nanocrystals. *Chemistry of Materials*, 25(8):1305–1317, apr 2013.

[54] Jessy B Rivest and Prashant K Jain. Cation exchange on the nanoscale: an emerging technique for new material synthesis, device fabrication, and chemical sensing. *Chemical Society reviews*, 42(1):89–96, jan 2013.

[55] N G Damhus. *Nomenclature of Inorganic Chemistry: IUPAC Recomendations 2005*. 2005.

[56] Catherine E Housecroft and Alan G Sharpe. *Inorganic Chemistry*. 2005.

[57] Gerhard H. Dieke. Spectra and Energy Levels of Rare Earth Ions in Crystals. *American Journal of Physics*, 38(3):399, 1963.

[58] C. Trallero-Giner, a. Debernardi, M. Cardona, E. Menéndez-Proupín, and a. Ekimov. Optical vibrons in CdSe dots and dispersion relation of the bulk material. *Physical Review B*, 57(8):4664–4669, 1998.

[59] Michael S Shur. *Handbook series on semiconductor parameters*, volume 1. World Scientific, 1996.

[60] J.J. Eilers. Doping the dots: doped quantum dots for luminescent solar concentrators, 2015.

[61] Urte Hotje, Christoph Rose, and Michael Binnewies. Lattice constants and molar volume in the system ZnS, ZnSe, CdS, CdSe. *Solid State Sciences*, 5(9):1259–1262, 2003.

[62] Zheng Li Renguo Xie and Xiaogang Peng, Renguo Xie, Zheng Li, and Xiaogang Peng. Nucleation Kinetics vs Chemical Kinetics in the Initial\nFormation of Semiconductor Nanocrystals. *J. Am. Chem. Soc.*, 131(42):15457–15466, 2009.

[63] D. E; Aspnes and A. A. Studna. Dielectric functions and optical parameters of Si, Ge, GaP, GaAs, GaSb, InP, InAs, and InSb from 1.5 to 6.0 eV. *Physical Review B*, 27(2):985–1009, 1983.

[64] Lianhua Qu, Za Peng, and Xiaogang Peng. Alternative routes toward high quality CdSe nanocrystals. *Nano Letters*, 1(6):333–337, 2001.

[65] Craig Bullen, Joel Van Embden, Jacek Jasieniak, Joanna E. Cosgriff, Roger J. Mulder, Ezio Rizzardo, Min Gu, and Colin L. Raston. High activity phosphine-free selenium precursor solution for semiconductor nanocrystal growth. *Chemistry of Materials*, 22(14):4135–4143, 2010.

[66] W William Yu, Lianhua Qu, Wenzhuo Guo, and Xiaogang Peng. Experimental Determination of the Extinction Coefficient of CdTe , CdSe , and CdS Nanocrystals Experimental Determination of the Extinction Coefficient of CdTe , CdSe , and CdS Nanocrystals. *Chemistry of Materials*, 125(17):2854–2860, 2003.

Appendices

Appendix A

InP and In(Zn)P quantum dot cores

Table A.1: Experimental parameters of the InP and In(Zn)P hot injection syntheses.

Code	In precursor	Zn precursor	P precursor	Injection T (°C)	Reaction T (°C)	Growth t	Washed with
S1	206 mg $InCl_3$	122 mg $ZnCl_2$	0.25 mL $P(DMA)_3$ in 1 mL OLAM	220	190	5 m	BuOH/MeOH
S2	0.20 g $InCl_3$	0.12 g $ZnCl_2$	0.25 mL $P(DMA)_3$ in 1 mL ODE	220	185	5 m	no
S3	0.20g $InCl_3$	0.12 g $ZnCl_2$	0.25 mL $P(DMA)_3$ in 1 mL ODE	220	185	5 m	no
S4	0.20 g $InCl_3$	none	0.25 mL $P(DMA)_3$ in 1 mL ODE	220	185	5 m	BuOH/MeOH
S5	0.20 g $InCl_3$	0.25 g YbCl3	0.25 mL $P(DMA)_3$ in 1 mL ODE	220	190	5 m	BuOH/MeOH
S6	0.20 g $InCl_3$	0.02 g YbCl3	0.25 mL $P(DMA)_3$ in 1 mL OLAM	220	192	5 m	MeOH
S7	0.597 g $InCl_3$	none	0.75 mL $P(DMA)_3$ in 3 mL OLAM	220	191.5	5 m	MeOH
S8	0.596 g $InCl_3$	none	0.75 mL $P(DMA)_3$ in 3 mL OLAM	220	190	5 m	MeOH
S9	0.199 g $InCl_3$	none	0.25 mL $P(DMA)_3$ in 1 mL OLAM	220	190	5 m	MeOH
S10	0.199 g $InCl_3$	0.123 g $ZnCl_2$	0.25 mL $P(DMA)_3$ in 1 mL OLAM	220	190	5 m	MeOH
S11	0.199 g $InCl_3$	0.245 g $ZnCl_2$	0.25 mL $P(DMA)_3$ in 1 mL OLAM	220	190	5 m	MeOH

Appendix B

InP quantum dot doping experiments

Table B.1: Experimental parameters of the doping experiments performed on InP and In(Zn)P quantum dots

Code	Core QD used	Doping temperature (°C)	Ratio Yb-precursor:QD	Doping time (m)	Encapsulant precursor
S1D0	S1	265	0	30	
S1D1	S1	265	30	30	
S1D2	S1	265	60	30	
S1D3	S1	265	90	30	
S1D4	S1	90	0	30	
S1D5	S1	90	30	30	
S1D6	S1	90	60	30	
S1D7	S1	90	90	30	
S7D1	S7	265	0	30	0.340 mL DDT added
S7D2	S7	265	120	30	0.340 mL DDT added
S7D3	S7	265	240	30	0.340 mL DDT added
S7D4	S7	265	480	30	0.340 mL DDT added
S7D5	S7	275	0	30	0.340 mL DDT added
S7D6	S7	275	120	30	0.340 mL DDT added
S7D7	S7	275	240	30	0.340 mL DDT added
S7D8	S7	275	480	30	0.340 mL DDT added
S7D9	S7	265	0	30	0.340 mL DDT added
S7D10	S7	265	120	30	0.340 mL DDT added
S7D11	S7	265	240	30	0.340 mL DDT added
S7D12	S7	265	480	30	0.340 mL DDT added
S7D13	S7	265	240	30	0.340 mL DDT added
S7D14	S7	265	480	30	0.340 mL DDT added
S7D15	S7	265	720	30	0.340 mL DDT added
S7D16	S7	265	960	30	0.340 mL DDT added
S7D17	S7	265	360	30	0.340 mL DDT added
S7D18	S7	265	480	30	0.340 mL DDT added
S7D19	S7	265	720	30	0.340 mL DDT added
S7D20	S7	265	960	30	0.340 mL DDT added
S8D1	S8	265	360	30	0.330 mL DDT added
S8D2	S8	265	360	30	0.990 mL 0.1 M S in ODE added
S8D3	S8	265	360	30	
S8D4	S8	265	360	30	0.150 mL 0.1 M $P(TMS)_3$ in ODE
S8D5	S8	265	360	30	0.150 mL 0.1 M P(DMA)3 in ODE
S8D6	S8	265	360	30	0.150 mL 0.1 M $P(DMA)_3$ in ODE
S8D7	S8	275	360	30	0.150 mL 0.1 M $P(DMA)_3$ in ODE
S8D8	S8	285	360	30	0.150 mL 0.1 M $P(DMA)_3$ in ODE
S8D9	S8	310	360	30	0.150 mL 0.1 M $P(DMA)_3$ in ODE
S8D10	S8	265	360	30	
S8D11	S8	265	360	30	
S8D12	S8	265	360	30	
S9D1	S9	265	360	30	
S10D1	S10	265	360	30	
S10D2	S10	265	360	30	
S11D1	S11	265	360	30	

Appendix C

InP quantum dot shelling experiments

Table C.1: Experimental parameters of the shelling experiments on (doped) InP and In(Zn)P quantum dots.

Code	Cores used	Shell precursor(s)	Reaction T (°C)	Reaction t
S2S1	2 mL S2	0.09 mmol Zn DTDC	135	2h
S2S2	2 mLS2	0.18 mmol Zn DTDC	135	2h
S3S1	2 mL S3	0.09 mmol Zn DTDC	135	2h
S3S2	2 mL S3	0.18 mmol Zn DTDC	135	2h
S2S3	1 mLS2	0.625 mmol DDT	200	8h
S2S4	1 mL S2	1.25 mmol DDT	200	8h
S3S3	1 mL S3	0.625 mmol DDT	200	8h
S3S4	1 mL S3	1.25 mmol DDT	200	8h
S4S1	0.4 mL S4	0.09 mmol Zn DTDC	135	2h
S6S1	0.4 mL S6	0.18 mmol $ZnCl_2$, 1.25 mmol DDT	205	5h
S6S2	0.4 mL S6	0.09 mmol Zn DTDC	135	2h 10m
S7D5S	2 mL S7D5	0.099 mmol $ZnCl_2$, 0.6875 mmol DDT	205	4h
S7D6S	2 mL S7D6	0.099 mmol $ZnCl_2$, 0.6875 mmol DDT	205	4h
S7D7S	2 mL S7D7	0.099 mmol $ZnCl_2$, 0.6875 mmol DDT	205	4h
S7D8S	2 mL S7D8	0.099 mmol $ZnCl_2$, 0.6875 mmol DDT	205	4h
S7D9S	2 mL S7D9	0.099 mmol $ZnCl_2$, 0.6875 mmol DDT	205	4h
S7D10S	2 mL S7D10	0.099 mmol $ZnCl_2$, 0.6875 mmol DDT	205	4h
S7D11S	2 mL S7D11	0.099 mmol $ZnCl_2$, 0.6875 mmol DDT	205	4h
S7D12S	2 mL S7D12	0.099 mmol $ZnCl_2$, 0.6875 mmol DDT	205	4h
S8S1	1 mL S8	0.044 mL 0.1 M $S(TMS)_2$	24	20m
S8S2	1 mL S8	0.044 mL 0.1 M $S(TMS)_2$	120	20m
S8S3	1 mL S8	0.174 mL 0.1 M $S(TMS)_2$, 0.174 mL 0.1 M $Zn(OA)_2$	120	20m
S8D10S1	3 mL S8D10	0.130 mL 0.1 M $S(TMS)_2$, 0.130 mL 0.1 M $Zn(OA)_2$	120	20m
S8D10S2	3mL S8D10	0.290 mL 0.1 M $S(TMS)_2$, 0.290 mL 0.1 M $Zn(OA)_2$	120	20m
S8D10S3	3mL S8D10	0.510 mL 0.1 M $S(TMS)_2$, 0.510 mL 0.1 M $Zn(OA)_2$	120	20m
S8D11S1	3mL S8D11	0.889 mL 0.1 M $S(TMS)_2$, 0.889 mL 0.1 M $Zn(OA)_2$	120	20m
S8D11S2	3mL S8D11	1.297 mL 0.1 M $S(TMS)_2$, 1.297 mL 0.1 M $Zn(OA)_2$	120	20m
S8D11S3	3mL S8D11	1.798 mL 0.1 M $S(TMS)_2$, 1.798 mL 0.1 M $Zn(OA)_2$	120	20m
S8D12S1	0.75 mL S8D12	0.005 g $Zn(SCNEt_2)_2$	110	1h 30m
S8D12S2	0.75 mL S8D12	0.011 g $Zn(SCNEt_2)_2$	110	1h 30m
S8D12S3	0.75 mL S8D12	0.022 g $Zn(SCNEt_2)_2$	110	1h 30m
S8D12S4	0.75 mL S8D12	0.033 g $Zn(SCNEt_2)_2$	110	1h 30m
S8D12S5	0.75 mL S8D12	0.044 mL 0.1 M $S(TMS)_2$	24	30m
S8D12S6	0.75 mL S8D12	0.108 mL 0.1 M $S(TMS)_2$	24	30m
S8D12S7	0.75 mL S8D12	0.191 mL 0.1 M $S(TMS)_2$	24	30m
S9S1	110 L S9	0.065 mL 0.1 M Se, 0.065 mL 0.1 M $Zn(OA)_2$	240	30m
S9S2	110 L S9	0.065 mL 0.1 M Se, 0.065 mL 0.1 M $Cd(OA)_2$	240	30m
S9D1S1	0.75 mL S9D1	0.072 mL 0.1 M Se, 0.072 mL 0.1 M $Zn(OA)_2$	240	30m
S9D1S2	0.75 mL S9D1	0.195 mL 0.1 M Se, 0.195 mL 0.1 M $Zn(OA)_2$	240	30m
S9D1S3	0.75 mL S9D1	0.072 mL 0.1 M Se, 0.072 mL 0.1 M $Cd(OA)_2$	240	30m
S9D1S4	0.75 mL S9D1	0.195 mL 0.1 M Se, 0.195 mL 0.1 M $Zn(OA)_2$	240	30m
S10D1S1	3 mL S10D1S1	0.300 mL 0.1 M $S(TMS)_2$, 0.300 mL 0.1 M $Zn(OA)_2$	200	20m
S11D1S1	3 mL S11D1S1	0.300 mL 0.1 M $S(TMS)_2$, 0.300 mL 0.1 M $Zn(OA)_2$	200	20m
S10D2S1	3 mL S10D1S2	0.120 mL 0.1 M $S(TMS)_2$, 0.120 mL 0.1 M $Zn(OA)_2$	210	20m
S10D2S2	3 mL S10D1S2	0.300 mL 0.1 M $S(TMS)_2$, 0.300 mL 0.1 M $Zn(OA)_2$	210	20m
S10D2S3	3 mL S10D1S2	0.550 mL 0.1 M $S(TMS)_2$, 0.550 mL 0.1 M $Zn(OA)_2$	210	20m
S10D2S4	3 mL S10D1S2	0.120 mL 0.1 M $S(TMS)_2$, 0.120 mL 0.1 M $Zn(OA)_2$	280	20m
S10D2S5	3 mL S10D1S2	0.300 mL 0.1 M $S(TMS)_2$, 0.300 mL 0.1 M $Zn(OA)_2$	280	20m
S10D2S6	3 mL S10D1S2	0.550 mL 0.1 M $S(TMS)_2$, 0.550 mL 0.1 M $Zn(OA)_2$	280	20m
S10D2S7	3 mL S10D1S2	0.120 mL 0.1 M $S(TMS)_2$, 0.120 mL 0.1 M $Zn(OA)_2$	120	20m
S10D2S8	3 mL S10D1S2	0.300 mL 0.1 M $S(TMS)_2$, 0.300 mL 0.1 M $Zn(OA)_2$	120	20m
S10D2S9	3 mL S10D1S2	0.550 mL 0.1 M $S(TMS)_2$, 0.550 mL 0.1 M $Zn(OA)_2$	120	20m

Appendix D

CdSe quantum dot doping experiments

Table D.1: Experimental conditions of doping experiments conducted with CdSe quantum dot cores.

Sample	Cores	QD's (nmol)	Ratio QD:Yb	Se precursor	Ratio Yb:Se	Reaction T (°C)
P13D1	P13	140	1:30	Se in ODE	1:01	270
P13D2	P13	140	1:30	Se in ODE	1:05	285
P13D3	P13	140	1:30	Se in ODE	1:10	285
P13D4	P13	140	1:30	Se in ODE	1:20	285
P13D5	P13	140	1:30	Se in ODE	1:05	270
P13D6	P13	140	1:30	Se in ODE	1:10	270
P13D7	P13	140	1:30	Se in ODE	1:20	270
P13D8	P13	140	1:30	Bullen-Se	1:10	270
P13D9	P13	140	1:30	Bullen-Se	1:20	270
P13D10	P13	140	1:30	Bullen-Se	1:30	270
P9D1	P9	140	1:30	Se in ODE	1:10	270
P10D1	P10	140	1:30	Se in ODE	1:10	255